

APERTURELESS SNOM: REALISTIC MODELING OF THE IMAGING PROCESS AND MEASUREMENTS OF RESONANT PLASMONIC NANOSTRUCTURES

THÈSE N° 3804 (2007)

PRÉSENTÉE LE 27 JUILLET 2007

À LA FACULTÉ DES SCIENCES DE BASE

Institut de physique des nanostructures

PROGRAMME DOCTORAL EN PHYSIQUE

ÉCOLE POLYTECHNIQUE FÉDÉRALE DE LAUSANNE

POUR L'OBTENTION DU GRADE DE DOCTEUR ÈS SCIENCES

PAR

Rubén ESTEBAN LLORENTE

Ingeniero de telecomunicacion, Universidad Politécnica de Madrid, Espagne
et de nationalité espagnole

acceptée sur proposition du jury:

Prof. R. Schaller, président du jury

Prof. K. Kern, directeur de thèse

Dr J. Aizpurua, rapporteur

Prof. G. Dietler, rapporteur

Prof. C. Hafner, rapporteur



ÉCOLE POLYTECHNIQUE
FÉDÉRALE DE LAUSANNE

Suisse
2007

Abstract

This thesis studies apertureless Scanning Near Field Optical Microscopy, a technique that uses the apex of a very sharp tip to obtain local optical information with lateral resolution much beyond the diffraction limit. Both theoretical and experimental results are discussed.

The theoretical work is a significant advance towards the quantitative convergence of experiments and theoretical predictions, and should be useful in aiding the interpretation of measured images. Extended tips and substrates are used, and the detector is also carefully modeled. A static tip in vacuum serves to study the influence of the tip and illumination geometry on the far fields and on the near fields in the proximity of the tip apex, the volume used to probe the sample. Including a gold substrate and the commonly used demodulation scheme allows to study the discrimination of the components carrying the local information. A very good discrimination is verified for silicon tips and small oscillation amplitudes, as far as the tip interacts closely with the substrate and the oscillation remains highly sinusoidal. The imaging process is studied by including patterned substrates. The obtained signal is mostly sensitive to a few nanometers of depth into the sample, and the influence of the scanning conditions on the level of signal, background suppression and lateral resolution is characterized. Further, a closer look into the behavior of the extended physical detector reveals the influence of the spatial inhomogeneities of the scattered fields and, for interferometric measurements, the large significance of the optical phase.

Experimentally, different techniques are first described that can facilitate images with clear local information. A cross polarization scheme is introduced which is very useful for non-perturbative measurements. It is applied to the mapping of the the field distribution surrounding plasmonic structures, for both the phase and the amplitude. Beyond dipolar resonances, I also study coupled dipoles and quadrupole field distributions. When imaging artifacts are avoided, the obtained images closely resemble theoretical expectations.

Keywords: Apertureless; SNOM; Realistic simulations; modeling; MMP; Imaging; Plasmonics; Nano-Optics; Non-perturbative; Demodulation; Quantitative; Nearfield; Farfield; Experiments; Higher harmonics; Optical Phase; Extended detector; Extended

tips; Strong interaction; Scanning Probe Microscopy.

Résumé

Cette thèse étudie le Microscope Optique en Champ Proche à sonde sans ouverture, une technique qui a recours à l'apex d'une pointe très fine afin d'obtenir une information optique locale avec une résolution latérale largement meilleure que la limite de diffraction. J'examinerai tant les résultats théoriques qu'expérimentaux.

L'étude théorique est une avancée importante vers la convergence quantitative des expériences et des prédictions théoriques et devrait faciliter l'interprétation des images mesurées. J'utilise des substrats et pointes étendues spatialement et le détecteur est également modélisé soigneusement. Une pointe statique sous vide sert à étudier l'influence de la géométrie de la pointe et de l'illumination sur les champs lointains et sur les champs proches à proximité de l'apex de la pointe, ce qui constitue le volume utilisé pour sonder l'échantillon. L'inclusion d'un substrat d'or et le schéma de démodulation utilisé habituellement permettent d'étudier la séparation des composants qui contiennent l'information locale. Une très bonne séparation est vérifiée pour les pointes de silicium et les petites amplitudes d'oscillation, pour autant que la pointe interagisse étroitement avec le substrat et que l'oscillation demeure hautement sinusoïdale. Le processus de formation de l'image est étudié en incluant des substrats pré-structurés. Le signal obtenu est sensible principalement à quelques nanomètres de profondeur à l'intérieur de l'échantillon et j'étudie l'influence des conditions de balayage sur le niveau du signal, sur la suppression du signal de fond et sur la résolution latérale. Un examen plus approfondi du comportement du détecteur physique étendu spatialement révèle l'influence des inhomogénéités spatiales des champs diffusés et, concernant les mesures interférométriques, la grande importance de la phase optique.

Sur le plan expérimental, je décris premièrement différentes techniques qui peuvent aider à obtenir des images avec une information locale claire. Un schéma faisant appel à deux polarisations perpendiculaires est inclus, ce qui s'avère très utile dans le cas de mesures non perturbatrices. Il s'applique à la mesure de la distribution du champ qui entoure les structures plasmoniques, tant pour la phase que pour l'amplitude. Au-delà des résonances dipolaires, j'analyse les champs de distribution dipolaires couplés et quadripolaires. Lorsque je parviens à éviter les artefacts d'imagerie, les images obtenues se rapprochent nettement des attentes théoriques.

Mots-clés Sonde sans ouverture; SNOM; Simulation réaliste; Modélisation; MMP;

Images; Plasmonique; Nano-optique; Non perturbatrices; Démodulation; Quantitative; Champ proche; Champs lointains; Expériences; Harmoniques supérieurs; Phase optique; Détecteur étendu spatialement; Pointe étendue spatialement; Interaction forte; Microscopie à Sonde à Balayage.

Contents

Abstract	i
Résumé	iii
Contents	v
1 Introduction	1
1.1 <i>a</i> SNOM working principles	2
1.1.1 Passive and active measurements	2
1.1.2 Near Field discrimination	3
1.1.3 Silicon as tip material	4
1.2 Theoretical work	5
1.2.1 The geometry of interest	6
1.2.2 The mathematical tool	8
1.3 Experimental work	9
2 Simulations of isolated tips	11
2.1 Results	13
2.1.1 Tip shape	13
2.1.2 Illumination parameters	16
2.1.3 Field distribution near the tip apex	18
2.2 Discussion	24
2.3 Conclusion	28

3	Simulations of tips over homogenous substrates	31
3.1	Transition from the dipole model...	33
3.2	Near field optical contrast	36
3.3	Experimental Results	39
3.4	Discussion and conclusion	41
4	Simulations of the imaging process	43
4.1	Modeling	43
4.2	Results	45
4.2.1	Numerical Convergence	45
4.2.2	General characteristics of the obtained signal	47
4.2.3	Tip length and inclusion depth	48
4.2.4	Scanning parameters	50
4.3	Discussion and conclusions	52
5	Studying the detector response:...	57
5.1	The model	57
5.1.1	The considered geometry	57
5.1.2	Modeling the detector response for each tip position	58
5.1.3	Modeling the detector response for an oscillating tip	60
5.2	Results	62
5.2.1	Interferometric and noninterferometric detection	63
5.2.2	Phase modulation for an oscillating tip	64
5.2.3	Phase distribution over the detector	68
5.2.4	Location of the detector area element	72
5.3	Discussion and conclusion	77
6	Experimental Set-up and procedures	81
6.1	General description of the set-up	81
6.2	Optical alignment	84

6.2.1	Characterizing the focus volume	85
6.2.2	Interferometry	87
6.3	Amplitude calibration	88
6.4	Controlling the polarization	89
6.5	Tip choice	93
6.6	Discussion and conclusions	94
7	Near field measurements beyond dipolar resonances	97
7.1	The samples: description of previous work	98
7.1.1	Far field characterization	99
7.1.2	Near field calculations	99
7.2	Near field characterization	102
7.2.1	Dipole resonances	102
7.2.2	Quadrupole resonances	105
7.2.3	Coupled dipoles resonances	105
7.3	Discussion and conclusions	108
8	Summary and Outlook	113
	Bibliography	117
	Curriculum vitae	129
	List of publications	131
	Acknowledgements	133

Chapter 1

Introduction

Conventional optical microscopy has been extensively used to gain ample information about material properties. However, it cannot resolve features much smaller than the wavelength used, and the search for new techniques to circumvent this limitation continues today [1–7].

An important family of solutions utilizes the higher confinement of electromagnetic density possible in the near field. First proposed in the twenties [8], half a century was necessary for the required technological advances [9]. In particular, the first solution valid at optical frequencies, Scanning Near Field Optical Microscopy (SNOM), uses tapered optical fibers [10–12] and allows to obtain a lateral resolution on the order of $\lambda/10$, but additional improvements have proved challenging.

This thesis focuses both experimentally and theoretically on a technique developed to go beyond this limit, apertureless SNOM (aSNOM) [13–21]. It utilizes a dielectric or metallic tip to concentrate the light near the apex. Lateral, evanescent and strongly focused illumination perpendicular to the sample have all been used. It allows to obtain resolution around 10 nm, largely independent of wavelength. It is a very general technique, for wavelengths ranging from the visible to the microwave [22–31]. Beyond elastic scattering, extinction [32], Raman scattering [33, 34], two photon processes [35, 36] and fluorescence can all be measured [37–41]. Ferroelectric [42–44] and magnetic information [45, 46] can also be gained. A particle is sometimes attached to the apex for a

better control of the apex shape [47]. Designs that combine aperture and apertureless characteristics also exist [48, 49]. I will consider in this thesis *aSNOM* for visible or near infrared illumination, lateral illumination and detection of the elastically scattered fields.

1.1 *aSNOM* working principles

Broadly speaking, *aSNOM* utilizes a tip to locally probe a sample which is illuminated by an external laser. The resolution is essentially determined by the size of the tip apex, which can be very small for sharp Atomic Force Microscope (AFM) tips. It is a scanning technique, meaning that the information about a sample is obtained pixel by pixel. A more detailed description is given below.

1.1.1 Passive and active measurements

To understand the origin of the signal obtained with *aSNOM*, I distinguish between two limiting modes, both treated in this thesis. In passive mode, near fields which are already present in the substrate [50–52] are to be measured. The tip should not perturb them, serving only as a scattering center to convert the near fields into propagating radiation that can be read at the far field. If the volume effectively probed by the tip apex is small, the lateral resolution achievable is high.

For an active mode measurement, tip and substrate strongly interact via the near fields forming a coupled system. The result is not only strong electromagnetic density in the gap [53], but also scattered radiation that can be collected by external optics [54, 55]. The interaction typically increases considerably for reduced distances between the tip apex and the structure to be measured, and high spatial resolution is possible.

1.1.2 Near Field discrimination

As mentioned, *aSNOM* was developed to resolve sample features much smaller than the wavelength, but to discriminate this information is often challenging. To facilitate the discussion, terms such as “near field signal” or “near field information” will be used in this thesis to refer to the fraction of the detected signal which is strongly affected by the volume of the studied system in the immediate proximity of the tip apex, making high lateral resolution possible. “Background fields” will refer to all other contributions, which often dominate the scattered signal.

By the given definition, the near field signal will be strongly affected by the tip position, which can be exploited to discriminate it even in the presence of strong background fields. One possible scheme, which also helps to avoid topographical artifacts [20, 56–59], uses an oscillating tip and higher harmonic demodulation [58, 60–63]. In a simplified picture valid for small oscillation amplitude and more critically examined in Ch. 5, demodulating the signal at the $n - th$ harmonic of the tip oscillation frequency is proportional to the $n - th$ derivative of the detected signal with respect to the direction of the tip vibration. If the amplitude is small enough to describe the background fields as linear over the trajectory of the tip, they are perfectly suppressed at the higher harmonics. As the near field signal is strongly dependent on position, their higher derivative contributions can be significant, and the desired information is correctly discriminated. Unfortunately, the level of signal obtained is also strongly dependent on the oscillation amplitude, and too small values result in a signal too low to be detected in practice. For large values, the influence of the demodulation is more complicated and, in particular, the evolution of the background cannot be described as linear and is not as efficiently suppressed [41, 62, 64]. The amplitude should thus be chosen with care, as illustrated in Chs. 3,4.

During this thesis, an interferometric detection scheme is typically considered. It combines the signal scattered by the tip-substrate system with an external laser to obtain phase information and to enhance the signal read at the lock-in amplifier. The

contribution from the interferometric term of the combined signal, for the n -th harmonic, is equivalent to calculating

$$H_n \propto \frac{1}{T} \int_0^T \mathcal{I}^*(d^{(ts)}(t)) e^{inwt} dt \quad (1.1)$$

which is in general complex-valued because it contains information about the amplitude and the phase of the signal detected. I will refer in this thesis to the amplitude of H_n unless otherwise mentioned. w refers to the angular frequency of oscillation of the tip and T to the period associated with it, or a value tending to infinity. $d^{(ts)}$ parameterizes the position of the tip, and for a sinusoidal oscillation perpendicular to the sample takes the form $d^{(ts)} = d_{min} + \mathcal{A}[1 + \cos(ut)]$, where \mathcal{A} is the oscillation amplitude and d_{min} is the position of the tip when closer to the substrate. \mathcal{I}^* corresponds to the signal generated by the detector at a certain position of the tip, described by $d^{(ts)}$, and can be written as $\mathcal{I}^* = \int_{A_{det}} |E(r)| \exp(-i \arg[E(r)]) dr$. It represents an integral of the field distribution, written as a function of the position r , over the area of the detector. In principle, the vectorial character of the fields should be considered, but due to the symmetry to be described in Sec. 1.2, only the component contained in the plane of incidence of the detector does not integrate to zero and I can consider the fields to be described as scalar. A more detailed discussion of the detection scheme, including the conditions under which the expression given for \mathcal{I}^* applies and the consequences of demodulating at the n -th harmonic for interferometric detection, is given in Ch. 5.

1.1.3 Silicon as tip material

Several tip materials are possible for *aSNOM*. In this thesis, silicon tips are used both for passive and active measurements. In the former case, the silicon tips are used without removing the oxide layer, and are a promising alternative to the carbon nanotube tips used in [50], as demonstrated in Ch. 6.

For the active configuration, metallic tips are discussed in most of the recent literature, due fundamentally to the large signal attainable when their plasmonic resonances

are excited [13, 65]. However, together with this significant advantage, there are also some drawbacks. Beyond the difficulty of optimizing the resonance [66] for tips shapes which are often not well controlled, plasmonic resonances are sensitive to small changes (for example in the substrate during the scanning). If the whole spectrum is not measured [47], the interpretation of images can be difficult [67]. Further, the coating steps involved in the fabrication of typical metallic AFM tips make obtaining a sharp apex, and thus ultimate resolution, challenging. Other approaches, such as electrochemical etching, are also demanding [68].

To excite plasmonic resonances, however, is not essential, and phenomena such as the lightning rod effect or material contrast can also be exploited to facilitate near field discrimination. These effects are expected to be less sensitive to the exact experimental conditions, and are also present for other materials. In particular, silicon tips [32, 37, 69–71] make use of a very mature technology offering commercial products with apex radii $< 10\text{nm}$, and are thus promising for ultimate lateral resolution [72]. Silicon tips could also diminish the quenching influence in fluorescence imaging [73]. I demonstrate both experimentally and theoretically how clear images can be obtained with silicon tips. In the active configuration, I first remove the native oxide to reveal the bare silicon.

1.2 Theoretical work

Copious theoretical work has allowed to better understand *aSNOM*. The phenomena of interest include the influence of the shape of the tips [74, 75], the interaction between tip and substrate [76, 77], the influence of higher harmonic demodulation [64] and the contrast and resolution expected over patterned samples [55, 78, 79]. The focus is often set in one or a few of them, and the others are simplified or not considered. To include all of them simultaneously, without recurring to 2-dimensional models or simplified forms of the Maxwell equations, is computationally demanding

My objective in the theoretical part of this thesis is to arrive at a model approaching typical aSNOM experimental conditions and solved by the full 3 dimensional Maxwell

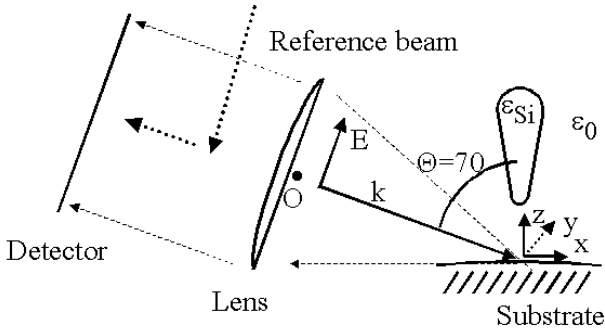


Figure 1.1: Illustration of the geometry used. The scattered radiation is collected by a lens and detected at the photodetector. The reference beam is used when interferometric detection is simulated.

equations. An incremental approach is taken, to gradually study the influence of different phenomena. I start in Ch. 2 by considering realistic tips and illuminations, and include in Ch. 3 a gold substrate to study the (strong) interaction between the tip and the substrate and the effect of demodulation at higher harmonics. In Ch. 4, a patterned substrate is introduced and the imaging process is analyzed. Care is taken in the model of the detector, and Ch. 5 takes a closer look at its behavior to reveal interesting *aSNOM* phenomena. Thus, the final model allows to study imaging at higher harmonic in the presence of strong tip-substrate interaction, for tips, samples and detectors that approach reality.

1.2.1 The geometry of interest

I describe here briefly the characteristics of the tip, illumination and substrate that will be regularly used later on the thesis. An example of the geometry used is shown in Fig. 1.1. For the interferometric detection, a reference beam described as a planar wave will be mixed with the field scattered by the tip and substrate. The values cited here are typical, and changes will be mentioned in the adequate places throughout the thesis.

Silicon tips ($\epsilon_{Si} = 17.76 + 0.508i$ [80]) embedded in vacuum are considered, shaped as C^1 -continuous cones capped by two hemispheres. The radius of the smaller is 10nm and the half angle of the cone is 10° . Tip lengths of 500, 1400 and 3000nm will be predominantly encountered. When a substrate is present, it is homogenous gold ($\epsilon_{Au} = -3.95 + 2.58i$ [81]) or a gold sphere of 10nm radius included in a glass substrate ($\epsilon_{glass} = 2.1$). The precise details will be given in Chs. 3,4.

As illumination, I consider planar waves or fifth order corrected [82–84] gaussian beams with 500nm waist radius, the latter focused at the tip apex or, when a substrate is present, at the surface of the substrate just below the apex ($x = y = z = 0$). $\lambda \sim 514.5\text{nm}$, linear polarization on the plane of incidence (plane xz) and $\Theta = 70^\circ$ angle between the propagation vector and the tip axis are used. The intensity of the excitation is such that the maximum value of its complex-valued electric field module is unity.

The far field signal of interest is either the intensity or the signal generated interferometrically by the detector. The signal is typically collected by a lens situated in the far field and of $NA \sim 0.342$, representative of experimental conditions, and is assumed to remain unchanged by the propagation to the detector, which is flat and oriented perpendicularly to the propagation direction. The lens is spherically symmetric with respect to the point labeled O in Fig. 1.1, and assumed to be perfect, i.e. a spherical wave with origin at $x = y = z = 0$ results in a beam of constant phase over the area of the detector, without any loss of intensity. Notice that this implies compensating the phase, which avoids its very fast dependence on position if the lens is not considered. The perfect symmetry of the model with respect to $y = 0$ justifies ignoring the out of plane electric field component (parallel to the y axis) for the interferometrically detected signal, as for this component the given expression (Sec. 1.1.2) integrates to zero¹. Beyond the scattered fields, the near field enhancement is also of interest, defined as the maximum of the module of the complex-valued electric field in the proximity of the

¹This is not the case for the Poynting vector, and both in plane and out of plane components are considered in this case

apex. Excepting the beginning of Ch. 3, I ignore for both near and far field the constant contribution obtained if the large sphere used as substrate is considered in isolation, as it depends on the exact characteristics of the sample. I do include the contribution from the gold inclusion as part of the detected signal.

1.2.2 The mathematical tool

Solving the Maxwell equations for the complicated geometries typical of *aSNOM* studies can be computationally demanding. Numerous techniques have been utilized [85], including perturbative techniques [86, 87], Green functions [79, 87, 88] Finite Differences Time Domain [89, 90], Finite Elements [91, 92], the reciprocity theorem [64] and multiple multipoles [70, 93].

I have used in my thesis a multiple multipole technique (MMP), in particular as implemented by the numerical platform MAX-1 [94, 95]. Near and far field can be simultaneously obtained and it is well adapted to geometries with features both much smaller (tip apex radius, tip-substrate distance) and much larger (tip and substrate size) than the wavelength. It utilizes a set of bulk solutions (expansions) of the three dimensional monochromatic Maxwell equations to describe the fields in each domain of homogenous dielectric constant. Each expansion is parameterized by a certain number of free coefficients, determined by which orders and degrees are included. The values of these coefficients are optimized to minimize the error on the boundary conditions at the discretized interfaces. Neither the position nor the degree/order of the expansions is automatically selected by the numerical platform, and care must be taken to avoid numerical interdependencies and minimize the computational requirements.

To gain confidence on the obtained results, I only accept those simulations that simultaneously verify two criteria. First, the average relative error in the matching points used for the minimization must be below 0.5 %, and comparable at other positions. Second, when the number of free coefficients describing the expansions is increased (typically a 50% or a 25%) only minor corrections are observed on the obtained results.

In particular, the intensity of the collected far field integrated over the detector area varies less than 1%. An example of the convergence achieved for a complex geometry is shown in Ch. 4, where the challenges involved in converging the results after high harmonic demodulation are also discussed.

1.3 Experimental work

The experimental set-up used for my measurements is described in Ch. 6. I also discuss in some detail different alignment techniques developed to facilitate obtaining an adequate near field signature. As the results are very sensitive to the exact alignment conditions, I typically do not compare the absolute values between different images but how the patterns vary; the color scales are chosen to improve the appearance of each individual image.

The obtained results can be divided into two categories. The first directly relate the measurements with the theory presented in this thesis, and appear mostly in Ch. 5, with some in Chs. 6,3. Indeed, theoretical and experimental work was frequently intertwined: experimental observations can often be better understood with simulations or simple analytical modeling, which can guide following experiments.

The second set of results are shown in Ch. 7. Here, the measurements do not pursue a better understanding of *aSNOM* by itself but information about a specific sample system of interest. In particular, I analyze the near field distribution near plasmonic structures that are interesting for the design of metamaterials and nanosensors for biological applications.

Chapter 2

Simulations of isolated tips

In this chapter I discuss the behavior of a tip situated in vacuum, i.e., without any substrate. A large number of experimental parameters are varied systematically to learn about their influence on both near field enhancements and scattered far field.

The tip shape has already been shown to be of considerable influence [74, 75, 96, 97]. Many studies have focused on maximizing the achievable near field enhancement by utilizing plasmonic resonances in a metal. For the reasons already discussed in the introduction, I focus on silicon tips.

Of special interest in this thesis are tips long enough to resemble those used in experiments. I study the evolution from small spherical tips to elongated tips several wavelengths long, enough to closely approach experimental conditions. For long tips, I change afterwards other parameters of relevance. The influence of the tip apex radius is studied, from a relatively blunt tip to a very sharp apex of 2 nm radius. Further, the characteristics of the illumination beam are systematically changed, which adds possibilities to increase the near field enhancement and gives interesting insight into the relation of the local fields and scattered far field. Also, not only the maximum value of the fields, but also their spatial distribution are discussed and described with a simple equation. I find that the field distribution scales with apex radius and is very robust with respect to changes in experimental conditions, which should help to obtain stable measurements.

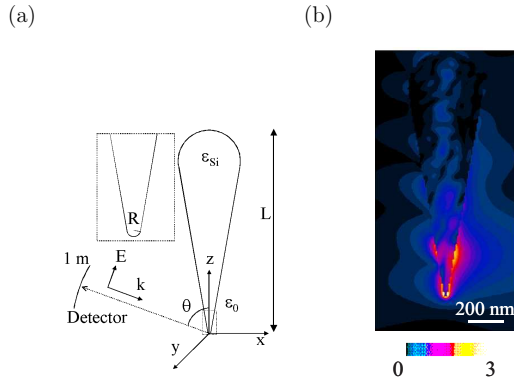


Figure 2.1: Geometry of the model tips considered and example of field patterns obtained. (a) Conical Si tips of length L and apex radius R are illuminated in vacuum by a Gaussian beam at an angle θ with respect to the tip axis. The scattered far field is recorded in backscattering direction. (b) Module of the average electric field for a typical simulation tip, exhibited in linear scale. A standing wave pattern inside can be distinguished, but the fields are weak for the upper part of the tip.

The geometry used for this chapter is shown in Fig. 2.1(a). I introduce a coordinate system useful for the discussion. Unless stated differently in the text, 1400nm long tips as described in Sec. 1.2 are used. The scattered fields are assumed to be collected in the backscattered direction at a distance of 1 m , clearly at the far field. At this stage, the collected radiation is reduced to the integral of the Poynting vector over a circular lens of $\text{NA} \sim 0.342$. Fig. 2.1(b) illustrate the field distribution for a given tip. Due to propagation, the fields are nonnegligible even in the very weakly illuminated top cap [98].

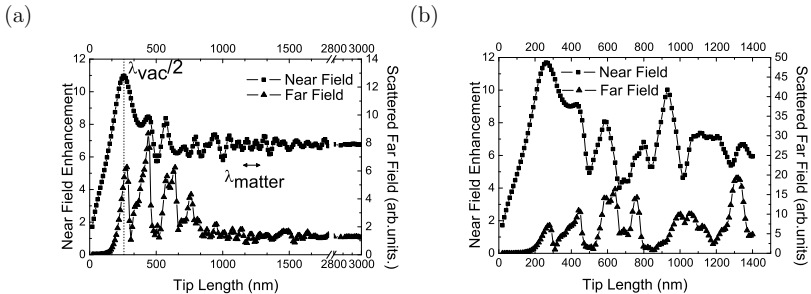


Figure 2.2: Near field enhancement and scattered far field when the length of the tip is modified, for Gaussian beam (a), and planar wave (b) illumination.

2.1 Results

2.1.1 Tip shape

Fig. 2.2 illustrates how the tip length L influences the near field enhancement and scattered far field. Considering (a) gaussian and (b) planar wave illumination is almost equivalent for tips much shorter than the wavelength. For micrometer long tips, the dependence with tip length is much stronger for plane wave illumination. This is specially relevant for the scattered fields, attributed to the influence of a strongly illuminated top cap. To avoid this undesired effect, gaussian beams of 500nm waist radius focused at the apex (Sec. 1.2) are used in the rest of this chapter when not mentioned otherwise.

As the tip is increased up to $L \approx 200\text{nm}$ constructive contributions to the near field enhancement result in an almost linear increase of the near field enhancement. The scattered far field intensity scales approximately with the volume V in a power law with exponent 2.55. I trace the difference with the V^2 expectation from Rayleigh scattering theory to the the transition from a spherical tip ($L = 20\text{nm}$) to an elongated conical shape ($L = 200\text{nm}$). If the tip is scaled uniformly the familiar V^2 law is regained.

For $L \gtrsim 200\text{nm}$ resonances appear. The position of the first maximum, at a length slightly bigger than $\lambda_{vac}/2$, reminds of classical antenna theories [99], a behavior already observed for the 2-dimensional case [100]. Resonances are observed not only on

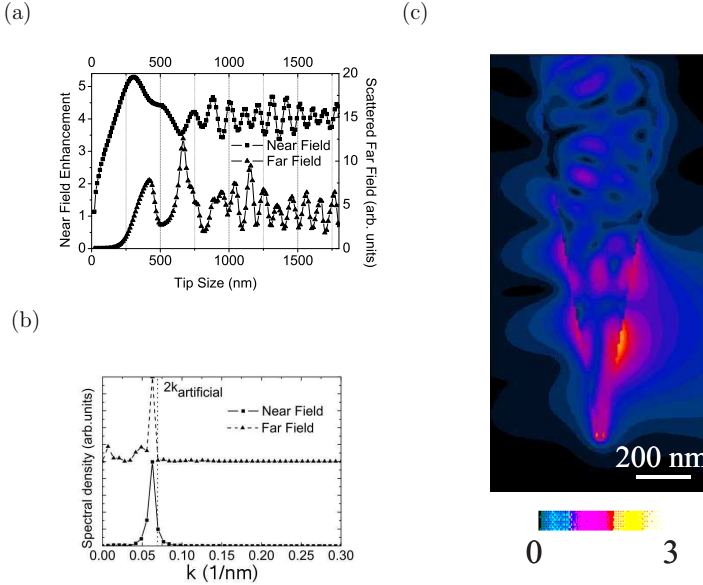


Figure 2.3: (a) Evolution of the near field enhancement and scattered far field with tip length for tip dielectric constant equal to 8 and gaussian beam illumination. (b) Fourier transform as a function of the wvector k of the traces in (a) for tips between $1\mu\text{m}$ and $1.8\mu\text{m}$ after subtracting the average value in this range. For clarity, the scattered far field trace is shifted vertically. (c) is a typical plot of the fields in linear scale for one of the considered tips.

the length scale of $\lambda_{vac}/2$ but also of $\lambda_{matter}/2$, the wavelength inside the tip material (silicon), attributed to the presence of standing waves (Fig. 2.1(b)). As the tip gets larger, the resonances loose in significance and the $\lambda_{matter}/2$ seem to become more important: the Fourier transform of the near field enhancement and scattered far fields for

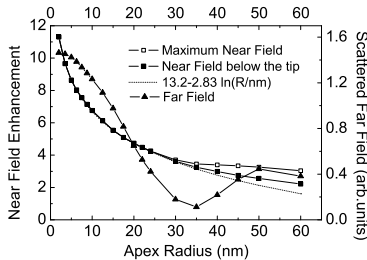


Figure 2.4: Evolution of the near and far field for apex radius varying between 2 and 60nm.

tips between $1\mu\text{m}$ and $1.8\mu\text{m}$ shows a high spectral density close to $2\pi/(\lambda_{\text{matter}}/2)$. It is in particular clear for briefly considered absorption-free tips, with dielectric constant equal to 8 (Fig. 2.3). Without energy loss in the material, standing waves gain in importance, and a strong oscillation in the length scale of $\lambda_{\text{matter}}/2$ is observed even for long tips.

Referring again to the usual silicon tips, for tip lengths larger than approximately three times the wavelength and the illumination beam waist radius ($\sim 1500\text{nm}$), waves are efficiently damped and the semispherical top cap is not efficiently illuminated. The variation from the average value becomes quite small. Between $2.8\mu\text{m}$ and $3\mu\text{m}$, it is less than ± 4 percent.

The influence of the apex radius R is studied next. Fig. 2.4 shows the evolution of the near field enhancement and the scattered far field intensity for R between 2 and 60nm , i.e., from extremely sharp to relatively blunt tips. $L \sim 3\mu\text{m}$ is used to minimize the influence of length-related resonances. Two values of near field enhancement are given here, the maximum of the complex-valued field module near the apex and the value just below the tip. They are almost identical for sharp tips, but differ for the larger radii because the position of the maximum shifts. The diverging expression $13.2 - 2.83 \ln(R/\text{nm})$ corresponds to an empirical fit and describes almost perfectly the near field enhancement for radii R between 2 and 30 nm. Although the scattered far field also increases for smaller radii, it saturates.

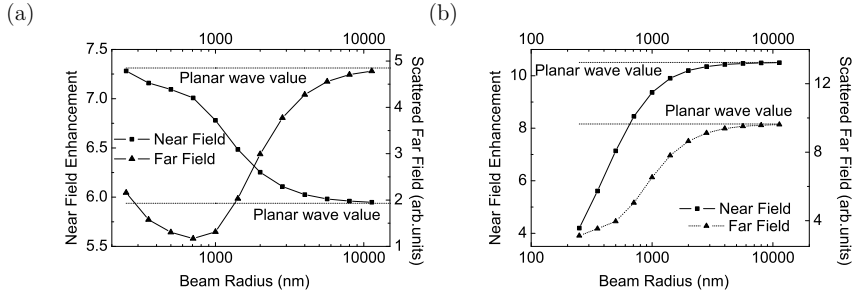


Figure 2.5: Near field enhancement and scattered far field intensity for different radii of the Gaussian excitation beam, asymptotically approaching those of a planar wave excitation for increasing beam waist radius. (a) for the usual value of $\theta = 70^\circ$ and (b) for $\theta = 20^\circ$

2.1.2 Illumination parameters

For gaussian beams, waist radius, angle of incidence and the relative location of tip apex and focus center will all influence the tip response to the illumination, an influence that is studied here. Broadly speaking, due to collective retardation effects, these parameters affect not only how strongly each part of the whole tip is excited, but also if the different partial volumes contribute constructively or destructively to the signal.

Fig. 2.5 shows the effect of variable beam waist radius for constant field amplitude at the focus –and thus varying beam intensity. $\theta = 70^\circ$ (a) and $\theta = 20^\circ$ (b) are considered. The evolution of the near field enhancement and the scattered far fields is even qualitatively different. A monotonous increase with waist radius is observed in the second case, due to predominantly constructive contributions. For $\theta = 70^\circ$, destructive interference [101] results in a local maxima for tight illumination. Contributions from the hemispherical region at the top of the tip gain importance for less confined focus, and probably explains why at $\sim 700\text{nm}$ the scattered far field intensity stop decreasing and start increasing with waist radius (Fig. 2.5(a)). In the limit of infinite beam waist radius the traces converge to the planar wave illumination case.

The influence of θ on the results is systematically shown in Fig. 2.6, for a $3\mu\text{m}$ long tip. As expected, the near field enhancement is minimal for the electrical field

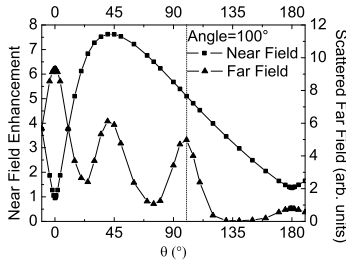


Figure 2.6: Near field enhancement and scattered far fields as a function of the angle θ between the beam propagation direction and the axis of a $3\mu\text{m}$ tip. An optimal near field enhancement around $\theta \sim 40^\circ$ is found.

perpendicular to the axis of the tip [90, 93, 102, 103] ($\theta = 0^\circ$ and 180°). The maximum is, however, not observed for the electrical field vector parallel to the axis of the tip ($\theta = 90^\circ$) but at a different angle [104], here $\theta \sim 40^\circ$. The scattered far field intensity presents four maxima. Two of the maxima, at $\theta = 0^\circ$ and 180° , can be explained by the strong scattering from the top semispherical cap. The third maximum, at $\sim 100^\circ$ degrees, corresponds to illumination perpendicular to the side surface of the cone. The fourth maximum is at the approximate position of the near field enhancement maximum, $\sim 40^\circ$, and is likely the most relevant for *aSNOM*.

Last, I consider illumination focused not exactly at the tip apex. The near field enhancement and far-field intensity for a displacement of the focus along the z direction is presented in Fig. 2.7(a). As long as the top cap is not strongly illuminated both values scale quite closely with the local field modulus of the excitation at the apex of the tip – with the square in the case of the scattered far field intensity. Similar conclusions are obtained when the illumination beam is displaced along the x and y direction, as seen in Fig. 2.7(b,c). This suggests a method to characterize beams [105–107], which I found useful in experiments and will be discussed in Ch. 6.

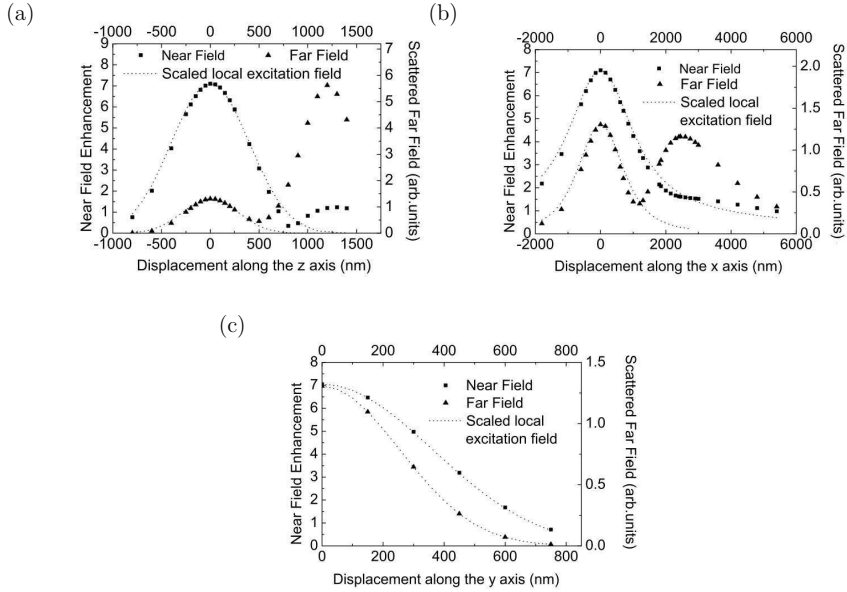


Figure 2.7: (a) Near field enhancement and scattered far field intensity for displacements of the focus along the z axis. Zero displacement corresponds to the location of the apex of the tip. Displacements towards positive values correspond to illumination of the upper part of the tip. The additional maxima at $\sim 1.25\mu\text{m}$ are attributed to the direct illumination of the top cap. For comparison, I plot in a dotted line the appropriately scaled modulus of the excitation field at the apex of the tip (for the near field enhancement) and its square (for the scattered far field intensity) for the corresponding displacement of the focus. (b) and (c) are equivalent to (a) but for displacements along x and y axis

2.1.3 Field distribution near the tip apex

Beyond the scattered far field intensity and the maximum of the near field modulus, the local distribution of the near field is also of interest [101, 108–110]. Fig. 2.8(a) presents the strength of $|E|$ for different radii, along the x axis, for $z = -R/2$. It shows that the normalized fields scale spatially quite accurately with the radius. Just below the apex the fields are predominantly vertically oriented –along the z axis–, as can be appreciated in Fig. 2.8(b).

In this subsection, I will study further how the module of the complex-valued field $|E|$ evolves near the apex of the tip. I find that its evolution changes only slightly for a

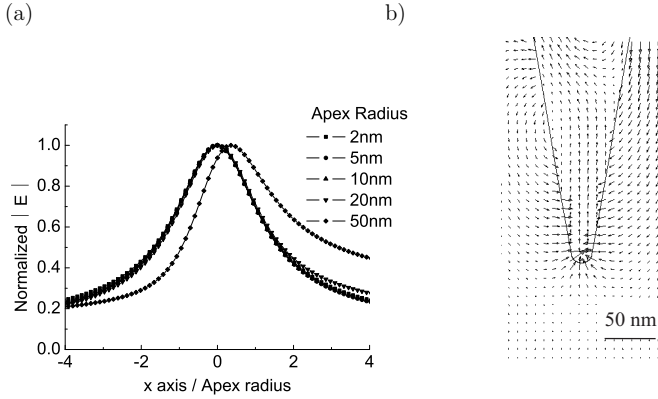


Figure 2.8: (a) Near field modulus (normalized to the maximum) along a horizontal cut at $R/2$ below the apex for different radii. (b) Instantaneous distribution of \vec{E} for $R = 10 \text{ nm}$ and $y = 0$

wide range of simulated conditions, and the entire range can be described with a single equation. I have already described in [111] the case of a cut along x . A good fit was obtained using a Lorentzian equation

$$|E| \propto E_0 + \frac{1}{Z_0^2 + x^2} \quad (2.1)$$

where E_0 and Z_0 are fitting parameters. The coordinates, here and in the following, refer to Fig. 2.1(a). In this section, a more general equation will be used, valid for the volume just below the tip apex. This equation takes the form

$$|E| = K \left[a + \frac{1}{\left(\frac{\rho^2 + (|z| - \alpha R)^2}{R^2} \right)^{\beta/2}} \right] \quad (2.2)$$

where $\rho = \sqrt{x^2 + y^2}$ and a , β , K and α are the fitting parameters. K represents a proportionality constant and Ka a uniform offset. R correspond to the tip apex, as before. For $\beta = 2$ and fixed y and z , Eq. (2.1) is recovered. Two things can be

immediately seen from Eq. (2.2): there is usually a very good rotational symmetry, and the fields scale approximately with R (Fig. 2.8(a)).

A main result in this subsection is that the spatial evolution of the near fields near the apex is little sensitive to the exact experimental conditions. To stress this conclusion, I set $\alpha = 0.9$ and $\beta = 2.07$ and fit only the offset parameter a and the proportionality factor. I will show that a very good fit with the simulated near field distribution is obtained for a large range of tip and illumination geometries. Allowing β and α to vary does not seem to significantly increase the applicability range of Eq. (2.2).

The simulated field distribution will be thus compared with

$$|E| = K \left[a + \frac{1}{\left(\frac{\rho^2 + (|z| - 0.9R)^2}{R^2} \right)^{1.035}} \right] \quad (2.3)$$

For aSNOM measurements, it is very important that the fields are strongly confined around the tip apex, as this confinement is important to explain the good lateral resolution achievable [70, 112]. It can already be appreciated from Eq. (2.3), but for a more quantitative discussion I use the full width half maximum value ($FWHM$) of the simulated values, calculated after subtracting the offset Ka for a line crossing $x = y = 0$ and situated in a plane perpendicular to the z axis. In principle, the $FWHM$ depends on which direction inside this plane is considered, but this effect is minor for the values that will be given here, due to good rotational symmetry. For a near field spatial distribution following exactly Eq. (2.3) and $z = 0$, $FWHM = 1.758R$, much smaller than the wavelength, which illustrates why a sharp tip can be used as “nanolamp” in *aSNOM*.

The distribution of the fields around the apex of a typical tip is shown in Fig. 2.9. Fig. 2.9(a,b) shows the simulated $|E|$ and the fit of the values given by Eq. (2.3). The fit is indeed very good. The $FWHM$ increases for bigger values of $|z|$, and for example for $z = -4\text{nm}$, $FWHM \sim 2.5R$ is obtained (to compare with $FWHM \sim 1.7R$ for $z = 0$), suggesting small tip-substrate distance being favorable for improved resolution.

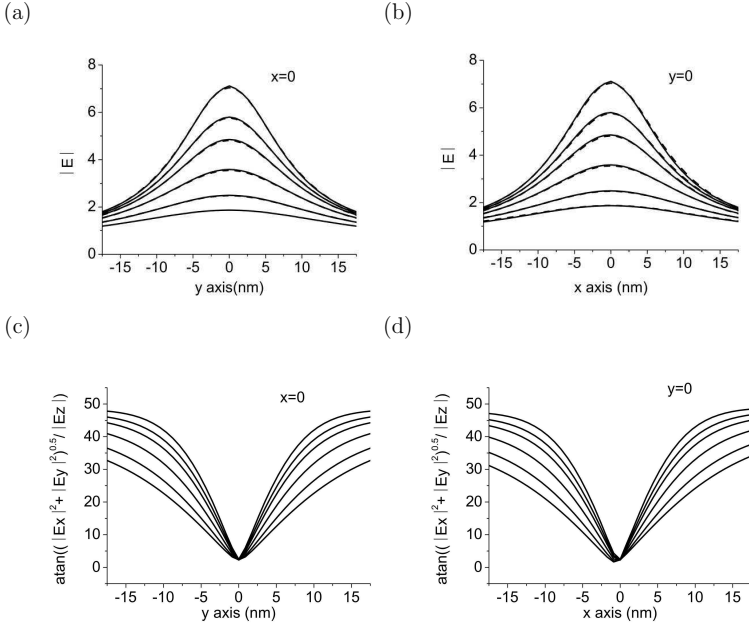


Figure 2.9: Evolution of the fields around the apex of a tip, for the typical tip geometry ($R = 10\text{nm}$). The different traces given are for $z = 0, -1, -2, -4, -7, -10\text{nm}$, the upper curves in each graph corresponding to the smaller values of z (a) $|E|$ for $x = 0$, (b) $|E|$ for $y = 0$, (c) $\arctan(\sqrt{(|Ex|^2 + |Ey|^2)}/|Ez|)$ for $x = 0$ and (d) for $y = 0$. Discontinued lines in (a) and (b) correspond to fitted values

Fig. 2.9(c,d) show $\arctan(\sqrt{(|Ex|^2 + |Ey|^2)}/|Ez|)$ for different values of z and for the planes $x = 0$ and $y = 0$, respectively. It is seen that the field is oriented predominantly along the the z axis in the proximity of the apex [24, 113]. In the following I will concentrate on $|E|$.

Fig. 2.10 illustrates the obtained field distribution for different geometries. The fit is usually worse when the rotational symmetry is lost, which in one-dimensional cuts is appreciated in a lack of symmetry with respect to the z axis for $y = 0$, but not for $x = 0$. I focus on geometries in which the fit with Eq. (2.3) has slightly deteriorated but is still good. As the only parameters fitted are the offset and a proportionality constant, all curves presenting a good fit are similar between themselves and scale well with the apex radius. I discuss next the large range of tip and illumination geometries following

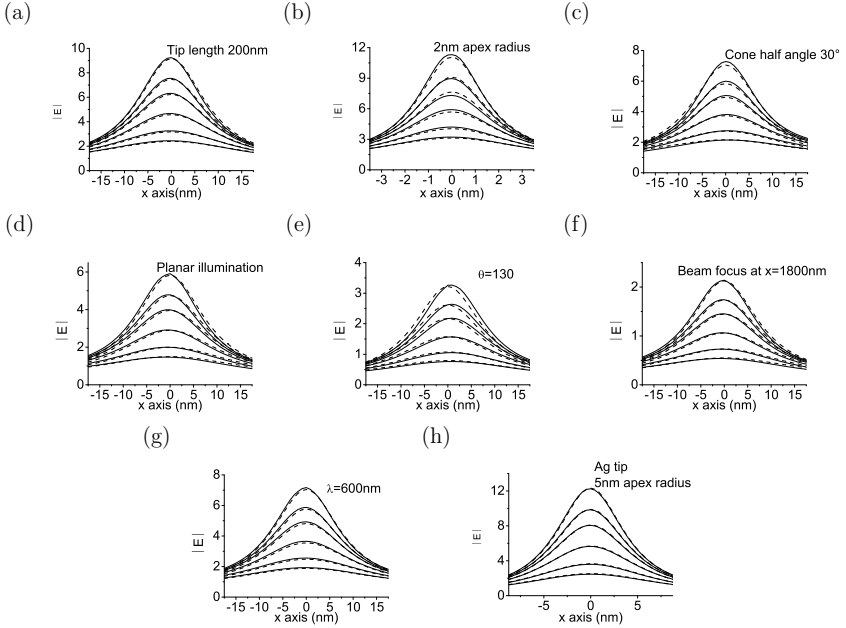


Figure 2.10: Shape of the fields around the apex for different characteristics of the tip and illumination beam. Parameters not mentioned below correspond to the description in Sec. 1.2 (tip length 1400nm, $R = 10$ nm, $\theta = 70$, Silicon tip, $\lambda = 514$ nm, 10 degrees cone half angle, gaussian beam of 500nm waist radius focused at the apex). Continued lines correspond to the simulated near fields, and dashed lines to the obtained fit. The different curves given are $z = 0, -1, -2, -4, -7, -10 * R/10$ nm, the bigger values of $|E|$ corresponding to the smaller values of $|z|$. (a) 200nm long tip, (b) tip with 2nm apex radius, (c) cone with 30 degrees half angle, (d) planar illumination, (e) illumination with $\theta = 130$ degrees (f) focus of the beam situated at $x = 1800$ nm, (g) $\lambda = 600$ nm and (h) silver tip with 5nm apex radius. (b,e) correspond to $3\mu\text{m}$ long tips.

Eq. (2.3) quite accurately, by individually changing different parameters.

- The influence of the tip length is studied first. Sufficiently long tips present a good fit with Eq. (2.3), as illustrated in Fig. 2.10(a) for the 200nm long tip. For a 50nm long tip the fit is worse, and for a sphere the rotational symmetry is considerably lost and the field distribution is not correctly described by Eq. (2.3). Short tips also results in smaller *FWHM*.
- A good fit is also obtained for sharp tips, independently of the exact tip radius,

which illustrate how the field around the apex scale almost perfectly with R . The case $R = 2\text{nm}$ is shown in Fig. 2.10(b). For $R = 50\text{nm}$ a worse fit and rotational symmetry was observed.

- For semi-angle of aperture between 5° and 30° a good fit is observed. The largest deviation is found for 30° (Fig. 2.10(c)).
- The results are almost unaffected by the waist radius of the beam. The planar wave illumination case is shown in Fig. 2.10(d).
- The fit remains good for illumination angles θ between 15° and 110° . It is worse outside of this range, being very bad for the limiting cases of 0° and 180° . Fig. 2.10(e) shows the obtained fit for 130° .
- A good fit is obtained when the beam focus is situated close, but not exactly, at the apex of the tip. As the focus is moved further from the apex, the behavior of the fields depend on the direction of the displacement. The obtained fit for $x = 1800$ is shown in Fig. 2.10(f), where only a slight asymmetry is observed. The fit is much worse, for example, for $z = 800\text{nm}$. Notice that in the latter case the top hemisphere is more strongly illuminated than the tip apex, which may explain the observed behavior.
- Changing the wavelength between 400 and 600 nm, and accordingly changing the dielectric constant, does not significantly affect the near field distribution. Fig. 2.10(g) represent the obtained fit for wavelength 600nm.
- To study the effect of a more dramatic change of the dielectric constant, silver tips are also considered ($\epsilon_{Ag} = -9.448 + 0.209i$) [114]. For a geometry otherwise identical to the typical in in this chapter, the fit is worse than for silicon as tip material. If, however, the tip length is reduced to 500nm or the apex radius to 5nm, Eq. (2.3) apply again. Fig. 2.10(h) shows the fit for the 5 nanometer apex radius.

2.2 Discussion

Values of scattered far field intensity and near field enhancement have been calculated for a tip in vacuum and different geometries of interest. The scattered far field is the physical magnitude directly measured in experiments and often facilitates the understanding of the physical processes involved. However, before the substrate and the demodulation are introduced, it is often difficult to establish the contribution from the tip apex –of special interest because it interacts most closely with the sample– to the total scattered field. Thus, to gain further information about the apex volume the near fields around it are also analyzed.

Typical values of near field enhancement obtained here are in the 5-10 range. This is in the low spectrum of field enhancements reported in related studies, which range from values less than 10 up to many tens [91, 93, 100, 115]. The variation derives from different illumination and tip characteristics. Notice that I have considered a dielectric tip, which does not exhibit the plasmonic resonances often utilized for high near fields.

The results from this chapter allow to determine experimental values which result in stronger near fields in the vicinity of the apex. For aSNOM imaging purposes, it is interesting to know how such conditions translate into the tip-substrate interaction. Although a direct proof requires the inclusion of a sample in the simulations, a high near field enhancement for the tip in vacuum is promising for strong interaction. Notice that the physical phenomena that enhance the field around the apex in this chapter –lightning rod effect, material contrast and antenna resonances –, are likely to be less affected by the presence of the substrate than plasmonic resonances (Sec. 1.1.3) .

The tip length is the first parameter which I have systematically varied. The dependence of the near field enhancement and scattered far field with tip length may be looked at from two different perspectives. First, one can follow a typical approach in the literature and choose the conditions that result in “optimal”, i.e. biggest enhancement. Selecting a length close to the $\sim \lambda/2$ antenna resonance indeed increases the near field enhancement. However, fabricating such a tip is a significant challenge, and the ob-

tained excess increase of 60 percent over the long-tip value make the effort questionable for this particular structure. Besides, the increase in the observable far field scattered intensity (more than 4 times the value of very long tips) likely results from all of the small tip's volume. This could complicate the extraction of the contribution from the apex volume.

The second perspective is to keep in mind the long tips actually used in typical *aSNOM*. The longer tips simulated here, under tightly focused illumination, are weakly sensitive to further increases of length and should be comparable to large experimental tips. The effect of simulating too short a tip can be estimated from Fig. 2.2. For a given tip length and geometry, I found several relevant length scales:

- λ_{vacuum} : the wavelength of the light in vacuum. Antenna resonances are found as long as the tip length is comparable with low order integral multiples of λ_{vacuum} .
- λ_{matter} : the wavelength in the tip material. Oscillations with this periodicity are found in both scattered far field and near field enhancement. Their strength is related with the absorption of the material. A small but finite absorption coefficient ensures that waves generated near the apex do not travel too far inside the domain up to the top cap and generate standing wave patterns extending over the complete tip volume.
- Waist radius of the beam: If it is comparable of bigger than the tip length, the upper termination of the tip gains in significance, a contribution often negligible in real experimental conditions.

Another relevant geometrical parameter is the tip apex radius. I find that the near field diverges with decreasing tip radius, which can be related to the infinite near field of perfectly sharp conical tips [116]. The strong near fields suggest that highly sharpened tips will interact strongly with the substrate, albeit in a smaller volume. The scattered far field also increases with decreasing tip radius, but it does not diverge for reasons of energy conservation. The increase of scattered far field is nonetheless relevant, as it

occurs when the strong fields near the apex are actually more confined spatially [30]. For high resolution imaging it is indeed desired to obtain stronger signal for sharper tips, but the tip-substrate interaction and the eventual use of a demodulation scheme must all be included for reliable predictions.

Not only the tip geometry, but also the illumination characteristics are relevant for *aSNOM*. It offers new options to optimize the near field enhancement. I study here the influence of angle of incidence, waist radius and position of the focus. I find that, for example, the optimal angle of incidence θ differs from the case of polarization exactly along the tip axis. $\theta \sim 40$ is found for the considered isolated tip, but for *aSNOM* measurements the optimal value can be influenced by the substrate [115].

Displacing the position of the focus in the proximity of the apex shows a simple proportionality relationship between the square of the local fields at the apex and scattered radiation. It suggests a focus characterization technique, to be discussed in Ch. 6. Notice, however, that absence of a substrate was assumed, which avoids the influence of strong tip-substrate interaction and strongly spatially inhomogeneous near fields.

Besides near field enhancement and scattered far field, I have also analyzed the distributions of the fields just below the tip apex. In particular, I found that Eq. (2.3) describes very well the field distribution for a large range of geometries. The equation implies a good rotational symmetry and a simple scaling of the fields with apex radius, at least up to moderate values [113]. Reducing the radius could thus result in a proportional improvement in resolution. The rotational symmetry may simplify mathematically deconvoluting the effect of the instrument response function.

It is illustrative to compare Eq. (2.3), obtained for a rounded cone, with some limiting cases. The critical term in Eq. (2.3) is of the form $(d/R)^{-\alpha}$, with R being the apex radius, d the distance to a point close to the center of the apex, and α a fitting parameter close to 2. Infinite, perfectly sharp cones of real dielectric constant are known to exhibit a $d^{\nu-1}$ behavior, with d being the distance to the apex and $\nu > 0$ the critical exponent, which depends on the cone angle as well as the dielectric material. $\nu < 1$ indicates that

the strong fields are infinitely confined in a point [116]. For sharp tips (either perfectly sharp or not), the tip axis is an axis of symmetry. On the other hand, E near a simple dipole polarizable sphere scales as $(d/R)^{-3}$, with the direction of \vec{E} being an axis of symmetry. R is the radius of the sphere and d the distance to the center of the sphere. The difference in the coefficient of the power law for long rounded cones and spheres illustrates how short tips result in stronger confinement of the field. A too optimistic estimation of achievable resolution for simulations using short tips is illustrated in Ch. 4.

Strong near fields near the apex seem to be important for Eq. (2.3) to apply. For silicon tips and beam focus at a position where the fields at the tip apex are significantly stronger than at the top cap, a good fit has been obtained when the maximum strength of the scattered fields at the apex is $\gtrsim 5-6$ larger than the excitation fields at the same position. For illumination focused at the apex, this is the same as saying that the near field enhancement as defined in this thesis must be $\gtrsim 5-6$.

This conclusion does not apply to off-focus illumination, as a good fit is possible even for much lower values, but notice that, in this case, the local fields in the proximity of the tip apex can still be large in comparison with the excitation strength near this volume. In this case, Eq. (2.3) seems to apply if the strength of the near fields near the apex is enhanced by contributions from the lower region of the tip (not the top cap).

The applicability of Eq. (2.3) for changes of the dielectric constant is also of interest. For a silver tip 1400 nm long and with a 10nm apex radius, Eq. (2.3) results in a worse fit that could be expected from the obtained > 5 near field enhancement. If the length is reduced to 500 nm long tip, or the apex radius to 5nm, the near field enhancement increases more than twofold, and Eq. (2.3) regains its validity. A strong near field enhancement looks still important for Eq. (2.3) to be valid, but I believe that it is important to consider how strong a role is played by the elongated shape of the tip, and not, for example, by dielectric contrast. A more quantitative analysis, valid for a large range of materials, requires further study, perhaps considering the separate influences of antenna resonances, lighting rod effect, material contrast and plasmonic resonances.

The small observed variation in the field distribution is promising for experiments, as it implies reproducibility in the presence of small changes of the experimental conditions. For imaging purposes it should be verified, however, that this holds also in the presence of a substrate.

2.3 Conclusion

In this chapter I have studied how both near and far fields of optically excited conical tips evolve with tip geometry and illumination conditions.

A strong tip-length dependence of the near field enhancement and scattered far field intensity is observed for short tips, but it levels out for tips that are long compared to the beam waist radius and the wavelength. Appropriately long tips and focused illumination should be simulated if typical experimental conditions are to be approached. Too short tips also result in more confined fields for a tip in vacuum.

For decreasing apex radius the near field enhancement grows without bounds. The detectable scattered far field intensity, i.e., the quantity measured in experiments, remains finite in accordance with energy conservation. Smaller apex radius also gives rise to a proportional increase in near field confinement, which is expected to translate to better lateral resolution. Besides this scaling effect, the field distribution remains approximately constant for many geometries and experimental conditions. If extrapolated to the presence of a substrate, this will facilitate obtaining robust experimental images. The fields present a very good rotational symmetry and can be described by a simple equation.

For strong near field enhancement and scattering, $\theta \sim 40^\circ$ is optimal. Different tip materials or geometries, of the presence of a sample surface, will likely alter the exact value, and simulating other scenarios is required. Notice, however, that the obtained angle will not necessarily realize an electric field vector parallel to the tip's axis.

The simple relationship between the scattered far field intensity and the local fields at the apex suggests a convenient method for three dimensional focus characterization

and for optical alignment in *aSNOM* experiments.

Chapter 3

Simulations of tips over homogenous substrates

Up to now I have treated a tip in vacuum, without considering any substrate. This allowed to systematically study the influence of several tip and illumination properties. To vary all these properties together in the presence of a substrate would have considerably increased the computational effort, particularly if the demodulation needed to discriminate the near field information is included. I expect many of the results to carry over when a sample is present, as discussed in Sec. 2.2.

However, a complete understanding of how *aSNOM* works does require including the substrate. This is the objective of the present chapter. At this stage, I focus on the tip-substrate interaction and how the near field information contained in the scattered fields can be recovered from the considerable background signal. The actual imaging process is covered in the next chapter.

The so-called dipole model [44, 117–119] is frequently used in *aSNOM* to discuss the tip-substrate interaction. A tip, situated over a perfectly flat surface, is approximated by a subwavelength-sized polarizable sphere, whose radius corresponds to the effective curvature at the tip apex. If retardation effects are neglected and a quasi-static dipole proportional to the local field is assumed to be excited at the sphere, a simple analytical expression can be obtained for the effective polarizability of the tip-substrate system [60].

$$\begin{cases} \alpha_{\perp}^{eff} \\ \alpha_{\parallel}^{eff} \end{cases} = \frac{\alpha(1 \pm \beta)}{1 - \frac{3 \pm 1}{2} \frac{\alpha\beta}{32\pi\epsilon_0(d^{(ts)} + R)^3}} \quad (3.1)$$

with

$$\alpha = 4\pi R^3 \epsilon_0 \frac{\epsilon_t - \epsilon_0}{\epsilon_t + 2\epsilon_0} \quad (3.2)$$

$$\beta = \frac{\epsilon_s - \epsilon_0}{\epsilon_s + \epsilon_0} \quad (3.3)$$

Here α_{\perp}^{eff} and α_{\parallel}^{eff} correspond to the effective polarizability obtained for polarization perpendicular and parallel to the surface. ϵ_t , ϵ_s and ϵ_0 are the dielectric constants of tip, substrate and vacuum, respectively, $d^{(ts)}$ is the distance between the lower edge of the tip and the substrate and R is as usual the radius of the tip. The interaction for polarization perpendicular to the surface is usually stronger. Assuming finally that the detectable far field intensity is proportional to the square of the effective polarizability of the coupled system, the dependence on ϵ_s illustrates how material contrast can be obtained in aSNOM [20, 60, 77, 120, 121]. When the tip approaches the substrate to distances $d^{(ts)}$ on the order of its radius R a nonlinear increase in the scattered field strength is predicted.

This simplified model disregards, however, many relevant phenomena. A dipolar approximation is insufficient for small tip-substrate distances, and expansions of higher order are required even for a spherical sub-wavelength tip [76, 122]. Further, the tip shape (Ch. 2) is also relevant here, both for the near field enhancement [70, 90, 92, 115, 123] and the detectable far field signal [77, 124, 125].

I simulate the interaction between tip and substrate for a scenario that resemble those from experiments. In Ch. 2, where no sample was considered, I gave both near field enhancement and scattered far field equal attention, partly because the latter is

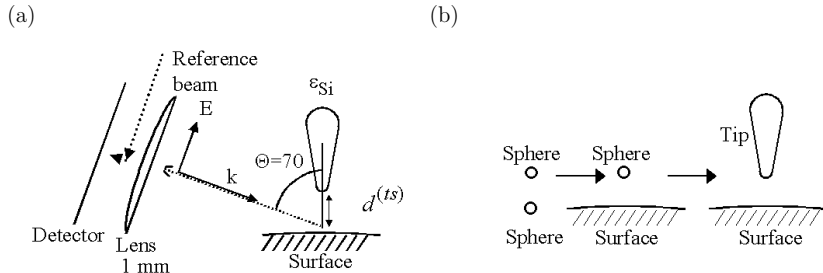


Figure 3.1: (a) Illustration of the geometry used. The reference beam is used in interferometric detection. (b) Evolution of the models simulated in the present paper, from two small spheres to a more realistic tip and substrate

the measurable quantity but the former is helpful to estimate expected tip-substrate interaction strength. Once the substrate, and thus the interaction, is included in the simulations, I concentrate on the scattered fields. References to near field enhancement will be occasionally made.

Further, just to consider the field scattered by a static tip is often not enough. For strong background fields, a demodulation technique [58, 60–64] helps to retrieve the information from localized near field interactions (Sec. 1.1.2). I show here that the information from the near fields can indeed be discriminated for a sharp silicon tip. In addition I discuss how too big an oscillation amplitude or a slightly anharmonic oscillation of the tip can significantly complicate the discrimination of the near field signal.

3.1 Transition from the dipole model towards realistic models

The scenario I am ultimately interested in is conveniently displayed in Fig. 3.1(a). A tip several wavelengths long (typically $1.4\mu\text{m}$) and a substrate consisting of a homogenous gold sphere of $2\mu\text{m}$ are considered. To avoid the influence of the top cap, a gaussian beam illumination is used when long tips are of interest. The distance between the tip

and the substrate $d^{(ts)}$ is varied between 1nm and several hundreds nanometers. The fields are collimated at $1mm$, i.e. in the far field region. I first consider the scattered intensity, and afterwards (Sec. 3.2) the interferometric signal demodulated at higher harmonics. Other details are given in Sec. 1.2.

Instead of directly presenting the results for this model, I start by discussing some simple cases that allow to gain insight into the origin of the different signal contributions and confidence that the final model closely describes the experimental situation. I briefly consider the well known system of two small and closely situated spheres illuminated by a planar wave (frequently used in studies of SERS [122]), and proceed via a “sphere over a surface” to an “elongated tip over surface” model [Fig. 3.1(b)].

Even for two spheres of 10nm radius illuminated by a planar wave, using dipoles is insufficient to correctly describe the strong interaction present at short distances. I have simulated this geometry by placing at the center of each spheres a multipole expansions (for the fields at the exterior of the spheres) and a Bessel expansions (for the interior). One sphere is interpreted as the Si tip and the other as a Au substrate. For short separations, a large number of orders is required to achieve convergence of the numerical description. In this case, for $d^{(ts)} \gtrsim 1$ nm multipoles up to ~ 15 th order are required. Due to the interaction, the near fields in the gap scattered by the two spheres system are considerably stronger for short distances, up to more than 20 times the excitation strength at 1nm. A steep increase of the scattered far field intensity can also be observed in Fig. 3.2.

I increase next the radius of the sphere serving as substrate up to $2\mu\text{m}$, still for planar wave excitation (Fig. 3.2). The constant contribution from the isolated substrate is ignored, as in the rest of this thesis. For $d^{(ts)} \gtrsim R$ and large substrates, a modulation of the far field intensity in the length scale of λ appear, due to retardation effects. First, a standing wave will be obtained in the proximity of the surface. Second, the field scattered directly by the tip and via reflections at the substrate surface can interfere constructively or destructively. For large substrates, the traces are qualitatively similar.

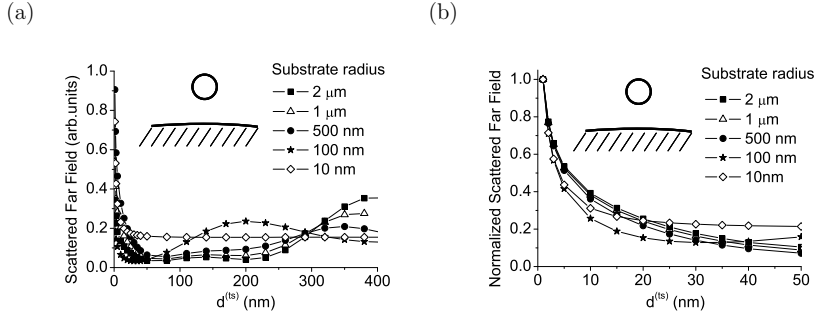


Figure 3.2: (a) Scattered far field intensity (in linear arbitrary units) as a function of tip-substrate separation for different radii of the spherical gold substrate. The tip is modeled as a silicon sphere of 10 nm radius. (b) represents a zoom of (a), normalized to the value at $d^{(ts)} = 1\text{nm}$.

The sharp increase of the far field intensity with decreasing distance for $d^{(ts)} \lesssim R$ is, as before, indicative of the near field interaction. It can be better appreciated in Fig. 3.2 (b), a zoom for small $d^{(ts)}$ normalized to the value at 1 nm distance to facilitate comparison. The localized character of the interaction is credited with the high achievable resolution (Sec. 1.1). Notice also the asymptotic behavior at short distances for increasing substrate radius. Under these conditions, the surface is essentially flat in the proximity of the apex, and the interaction becomes numerically similar to the flat substrate case. In the following, I use a substrate sphere diameter of 2 μm .

To arrive at our final model, the length of the tip is increased. A focused beam is used to avoid the strong scattering from the top cap for the larger tips. It also represents the experimental conditions more closely than planar wave illumination. As expected, both near field enhancement and scattered fields are affected. In particular, the near field enhancement in the gap at $d^{(ts)} = 1$ nm for the 1400nm long tip is up to ~ 65 , more than 5 times larger than that of the spherical tip.

The far field is even more dramatically affected, as a small sphere has a scattering cross section orders of magnitude smaller than a large tip. At $d^{(ts)} = 1$ nm the scattered field intensity exhibits ratios of $\sim 34000 : 1300 : 1$, for 1400 nm, 150 nm and spherical (20nm) tips, respectively. For 1 mW incident power, $\sim 1.5 \mu\text{W}$, 60nW and 45pW are

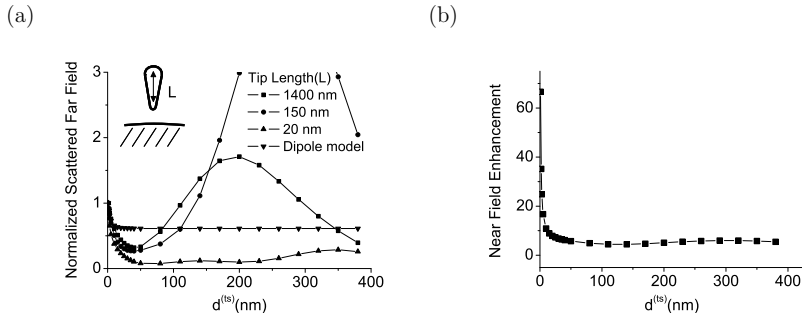


Figure 3.3: (a) Scattered far field intensity(normalized to the 1nm value) as a function of tip-substrate separation for silicon tips of different length and the prediction of the quasi-static dipole model. The substrate is a gold sphere of $2\mu\text{m}$ diameter. (b) Near field enhancement as a function of tip-substrate separation for a 1400nm long tip

collected. Fig. 3.3(a) shows the scattered far field obtained for different tip lengths, as well as the predicted values for the dipole model, normalized to the value at $d^{(ts)} = 1\text{ nm}$ for comparison. The scattered far field obtained for tips 1.2, $1.6\mu\text{m}$ long are similar to those shown for $1.4\mu\text{m}$. Notice also that while a very strong signature of the interaction is observed for the near field enhancement(Fig. 3.3(b)), it is much less clear in the far field, which points to the need of an effective discrimination scheme.

3.2 Near field optical contrast

A demodulation scheme to discriminate the near field information was already described in Ch. 1. Its main idea is to detect the signal at higher harmonics of the tip oscillation frequency. I will show how the background can be effectively suppressed and how the characteristics of the tip oscillation are very important for *aSNOM*. Interferometric detection is assumed.

In an optimal experimental measurement, only the scattered fields containing near field information would be detected after demodulation, with all the background being effectively suppressed. Consequently, if the tip is separated from the substrate, the signal will die out. This is the idea behind the so-called approach curves [121,126–128],

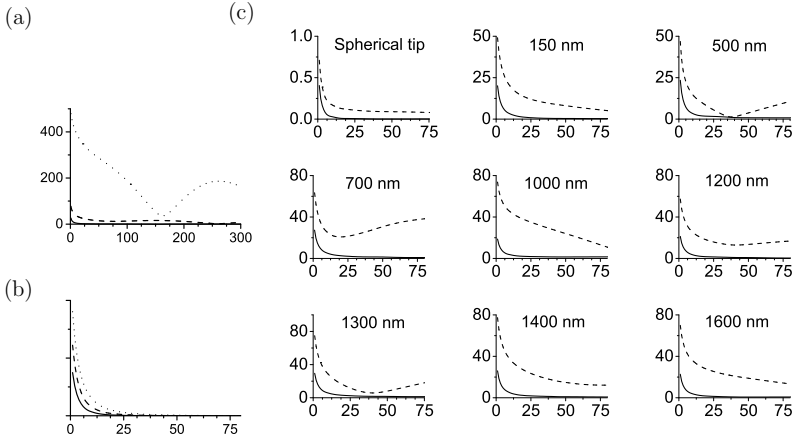


Figure 3.4: Approach curves for the first (dotted), second (dashed), and third harmonic (continuous) as functions of d_{min} for (a) a $1.4 \mu\text{m}$ tip, (b) the dipole model and (c) tips of variable length. All traces are scaled to the same arbitrary linear scale, except for the dipole model. Notice that the values for the spherical tip are much smaller. The oscillation amplitude is 20 nm . The very weak third harmonic in (a) is better appreciated in (c) in the graph corresponding to $1.4 \mu\text{m}$. For readability, only second and third harmonic are displayed on (c).

in which the amplitude of the demodulated signal is plotted for different tip-substrate distances. A satisfactory approach curve will show a rapidly increasing detected signal for $d_{min} \lesssim R$.

To numerically simulate them, it is necessary to obtain the evolution of the scattered fields as a function of $d^{(ts)}$ and subsequently compute the integral Eq. (1.1) for different positions of the oscillating tip, described if not otherwise stated as $d^{(ts)} = d_{min} + \mathcal{A}[1 + \cos(\omega t)]$, where d_{min} is the minimum value of $d^{(ts)}$. As discussed in Sec. 1.1.2, only the component contained in the plane of incidence of the detector is considered. Fig. 3.4(a) shows simulated approach curves for the 1400 nm silicon tip, distances up to 300 nm and 20 nm modulation amplitude. The second and especially the third harmonic present a considerable signal increase when d_{min} is small, as desired. Higher harmonics offer better background suppression and are promising for higher lateral resolution [63, 64], but the signal level is smaller, an interplay further discussed in Ch. 4.

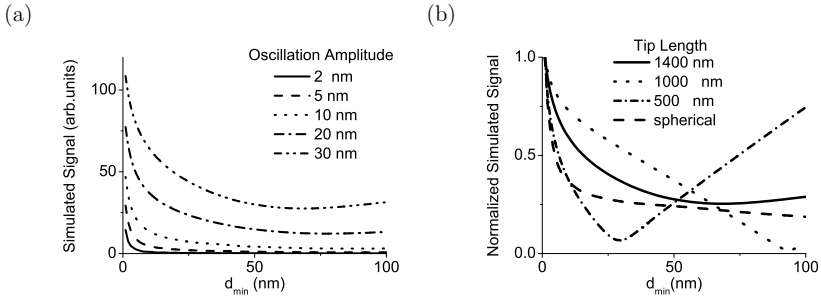


Figure 3.5: Approach curves for the second harmonic (a) for a 1400 nm tip changing the oscillation amplitude, (b) for tips of different lengths and 30 nm oscillation amplitude.

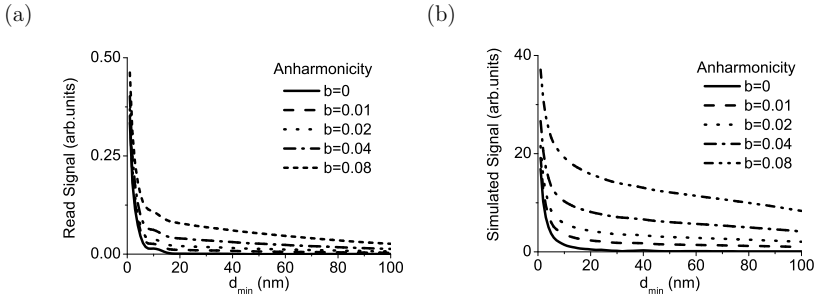


Figure 3.6: Approach curves for third harmonic demodulation with increasing anharmonicity b , modeling (a) a spherical tip, (b) a 1400 nm long conical tip. Both tips have an apex radius of 10 nm and the modulation amplitude is 10 nm.

To obtain good background suppression, it is important to correctly choose the experimental parameters. In particular, the oscillation amplitude \mathcal{A} was already mentioned in Sec. 1.1.2 to be important. Fig. 3.5(a), where approach curves for different \mathcal{A} at the second harmonic are plotted, shows how increasing the amplitude can increase the level of signal but also deteriorate the background suppression, which requires a compromise [129]. Here, it is convenient to use amplitudes not much above R , as the background increases considerably faster than the near field contribution.

Experimentally, the tip oscillation is not perfectly sinusoidal [130–132]. Even for small oscillation amplitude, the background suppression can be inadequate in the presence of anharmonicities in the movement of the tip. Consider as an example a tip

motion described by $d^{(ts)} = d_{min} + A[1 + b + \cos(ut) + b \cos(3ut)]$, with b a parameter that describes the anharmonicity. The approach curve for the 1400nm long tip at the third harmonic, plotted in Fig. 3.6(b), clearly show how an anharmonicity of just a few percent gives rise to noticeably deteriorated background suppression. Thus, the anharmonicity should be kept at acceptable levels or a more sophisticated scheme must be used to extract reliable near field optical information [43,61].

I study next how the approach curves are affected by considering other tip lengths. They have been calculated for the dipole model and for several tip lengths (Fig. 3.4(b-c)). I concentrate in harmonics higher than the first and d_{min} up to 80 nm the conditions more relevant to near field optical microscopy. Beyond the much smaller signal obtained for the spherical tip, the evolution of the signal with d_{min} , and thus the background suppression, depends on tip length even for tips larger than the wavelength. The tips that are longer than one or two wavelengths behave qualitatively similar, but a dependence with length is observed even for the longer tips here considered. This conclusion is further stressed by Fig. 3.5(b), which shows approach curves at the second harmonic for $\mathcal{A} = 30\text{nm}$ and different tip lengths, normalized to the maximum value for readability.

Last, I study the influence of considering too short tips when the effect of the anharmonicity is of interest. Fig. 3.6 shows how for the spherical tip the deterioration of the approach curves is much smaller than in the 1400nm case, which is attributed to the stronger background for the long tips. Thus, to model an adequate tip length is important for accurate predictions and in particular to establish the exact influence of oscillation amplitude and anharmonicity.

3.3 Experimental Results

Although this chapter focuses on numerical simulations, it is closely related to experiments. With this in mind, I have used the experimental set-up in our group (Ch. 6), to measure approach curves similar to the ones presented here, for bare silicon tips.

Fig. 3.7(a) exemplifies an approach curve in the third harmonic over the metallic

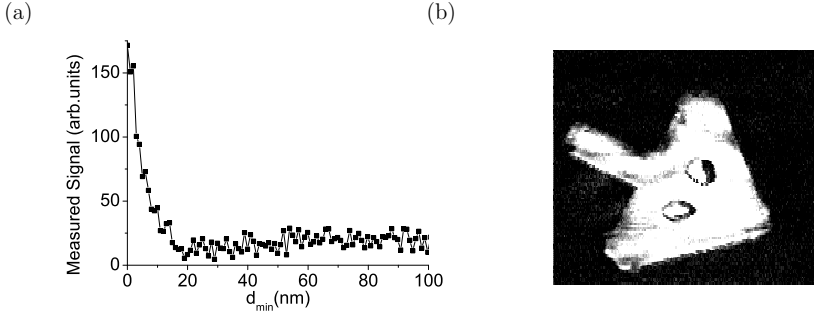


Figure 3.7: Example of measured results illustrating the possibility of using silicon tips for aSNOM. (a) Measured approach curve in the third harmonic. The modulation amplitude is roughly 13 nm. In both images $\lambda \sim 820$ nm is used (b) Image of a metallic structure on glass. The glass appears black in the picture due to the much smaller level of received signal. The image size is $3 \times 3 \mu\text{m}$.

(AuPd) substrate shown in (b), to be compared with Fig. 3.4. As the tip is separated from the surface, the signal decays in $\sim 20\text{nm}$ to the background level, a clear near field signature. It looks qualitatively very similar to the simulations shown in this chapter. A complete quantitative agreement cannot be expected at this stage as it would require a perfect knowledge of tip and illumination characteristics.

The approach curve measured indicates a good near field discrimination, which further strengthens the claim that silicon tips can be used successfully in aSNOM. This is confirmed in Fig. 3.7(b), an experimental measurement for a metal structure over a glass substrate¹. In the big structure, two smaller particles are observed. The topography indicates that they are significantly higher than the rest of the structure, and SEM images suggest that they are made of AuPd left-overs from the fabrication process. As expected, the signal is clearly stronger over the metal and the resolution is significantly superior to the diffraction limit. Comparable signal is obtained at the small particles and at the rest of the metal structures, independent of the considerably different height, as desired for measurement dominated by the optical interaction. At the steep edges, other effects may appear [22, 133, 134].

¹Fig. 3.7(b) was measured following the homodyne approach given in Sec. 5.1.3, and Fig. 3.7(a) a slightly modified scheme. Both are exactly identical for the assumed perfectly sinusoidal tip oscillation.

3.4 Discussion and conclusion

Quantitative estimates have been obtained of expected near field enhancement and scattered far field signal for a realistic scenario. I concentrate on the latter, which is the measurable signal in aSNOM experiments. I illustrate how the near field signal can be discriminated with a convenient demodulation scheme and adequate tip oscillation.

To quantitatively model a typical experimental scenario, large tips and substrates are necessary. A compromise between approaching realistic tip sizes and achieving numerical convergence in a reasonable time is found for a spherical substrate of $2\mu\text{m}$ diameter, which can be considered locally flat, and a 1400nm long tip. An exact convergence with the very long tips used in experiments requires even larger lengths (Fig. 3.4).

Considering not small spherical tips but long rounded cones is important to include the increased near field enhancement due to the lightning rod effect and the much larger cross section characteristic of big particles. For long tips, a near field enhancement of ~ 65 has been found for $d_{min} = 1\text{nm}$. For 1 mW incident power, solid angle of detection $NA = 0.342$ and 500nm beam radius, $\sim 1.5\mu\text{W}$ scattered signal is expected.

Both theoretical and experimental results in this chapter illustrate that a good discrimination of the near field signal is indeed possible with silicon tips, whose advantages were discussed in Sec. 1.1.3. In my simulations, second and third harmonic demodulation results in a good near field discrimination with amplitudes similar to the apex radius. Much larger amplitudes significantly increase the background without a proportional increase of the near field signal detected. Anharmonicities in the tip movement must also be carefully controlled. This exemplifies the importance of an adequate choice of the experimental parameters to improve the discrimination of the local optical information.

The model in the present chapter demonstrates that it is possible to fully accounts for the tip-substrate interaction of realistic tips and substrates. A very good discrimination of the near field information is possible for sharp silicon tips. Anharmonic tip motion or too high vibration amplitudes are found to deteriorate the near field discrimination. The natural next step is to study the imaging of structured substrates, as will be done

in the next chapter.

Chapter 4

Simulations of the imaging process

In Ch. 3, I have studied *aSNOM* by simulating the oscillation of the tip over a fixed point of the substrate. To better understand experimentally obtained images, it is meaningful to simulate scans over patterned substrate. Much work in the literature is not specific to *aSNOM*, but insofar as it concentrates on the near field distribution, it relates also to it. The localized nature of the near fields [135, 136], the convenience to scan near the sample [88, 137] and the influence of optical and topographical contrast were all studied. Additional studies continued this work [54, 55, 138–140] for more specific *aSNOM* scenarios. However simulating the imaging process with the complete 3-dimensional Maxwell equations, for tips and substrates approaching realistic geometries, strong interaction and high harmonic demodulation is still challenging. Such results are presented in the present chapter.

4.1 Modeling

Details of the geometry are shown in Fig. 4.1. I choose 500 nm long silicon tips and planar wave illumination as a reasonable compromise between numerical requirements and the desire to resemble typical experimental conditions. Specifically, near field enhancement and scattered far field intensity can be expected to be comparable to those of much longer tips (Chs. 2,3). I also expect the spatial field distribution in the proximity of

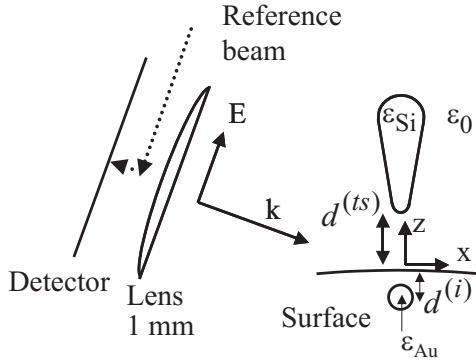


Figure 4.1: Illustration of the geometry used. The reference beam is used for the interferometric detection

the apex of the tip to be almost unaffected by further increases in length or the use of focused illumination, which assumes that the results from Sec. 2.1.3 remain true in the presence of a substrate.

The substrate is a glass sphere of $2\mu\text{m}$ diameter and $\epsilon_{\text{glass}} = 2.1$, with a 10nm gold spherical inclusion situated at a few nanometers of the glass-vacuum interface, $d^{(i)}$. The origin of the coordinate axis is situated at the point of the glass vacuum interface exactly over the center of the inclusion. The detector is situated at 1 mm distance as in Ch. 3 and, as usual for the demodulated results, I only consider the component of the field in its plane of incidence and ignore the contribution from the glass substrate. The remaining parameters correspond to the description from Sec. 1.2.

The substrate has been chosen with several things in mind. First, it should contain some structure –the gold inclusion– much smaller than the wavelength, to illustrate the lateral resolution capabilities of *aSNOM*. The inclusion should be, however, big enough for the interaction with the tip to scatter strongly enough for correct discrimination of the local information after demodulation. Second, the substrate and inclusion material, glass and gold, present very different values of the dielectric constant, with gold expected to result in a considerably stronger optical signal than glass [126]. Third, no point from the given geometry is adjacent to three regions of different dielectric, and there is no

infinitely sharp corner or edge, which simplifies numerical simulations. Last, changing the distance between the inclusion and the vacuum-glass interface, $d^{(i)}$ provides a natural way to study how deep into a sample *aSNOM* can probe.

In this chapter, the evolution of the amplitude of the demodulated signal as the tip moves along the x is typically discussed. For each x , simulations are solved for different tip positions along the axis z , to account for the tip oscillation (described as $d^{(ts)} = d_{min} + \mathcal{A}[1 + \cos(wt)]$ except for anharmonic movement of the tip). The minimum tip-substrate distance d_{min} is kept constant, i.e. I work in constant distance mode, which allows to obtain topography-free signal [59]. The units of the obtained signal are arbitrary, as they depend on the reference signal power or photodetector sensibility, but they are directly comparable to last chapter's.

I discussed in Sec. 1.1.2 that I call near field signal to the contribution influenced by the substrate volume in the immediate proximity of the tip apex. In this chapter, it reveals itself most clearly in a steep increase of the signal when the tip interacts strongly with the gold inclusion. Near field information can also be generated by the tip-glass interaction, but is typically weaker and a strong signal for large $|x|$ is attributed to the influence of the background.

In this chapter I study the influence of the inclusion depth, $d^{(i)}$, and other experimentally relevant parameters on expected level of signal, background suppression and achievable resolution. I also compare the simulated images from the long tip with those from a spherical, 10 nm radius sphere, to better understand the limitations of simulating too short tips.

4.2 Results

4.2.1 Numerical Convergence

I already discussed in Sec. 1.2 the need of good numerical convergence. For *aSNOM*, besides scattered far field intensity and near field enhancement, the signal after demod-

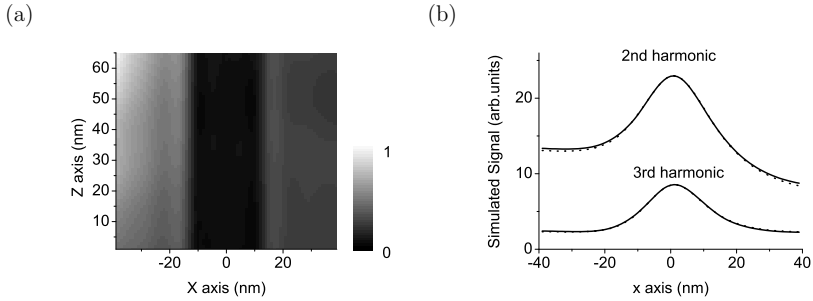


Figure 4.2: (a) illustrates the difference between two sets of solutions of the Maxwell equations, the second using ~ 25 percent more free coefficients in the expansions. The signal generated at the photodetector by the interferometric term was calculated for each positions of the tip along a 2-dimensional map. The modulus of the relative signal change is plotted in percentage. (b) corresponds to the demodulated signal amplitude for 1-dimensional scans, for the second and third harmonic, $\mathcal{A} = 20\text{nm}$, $d_{\min} = 1\text{nm}$ and $d^{(i)} = 1\text{nm}$. The continued line have been obtained using fewer free coefficients than the dotted one.

ulation is also important. The latter is a not just a function of the signal in a particular tip position, but on how the signal changes along the tip trajectory. Small numerical error between two closely situated tip positions can make a considerable difference on the derivatives. I illustrate here the convergence that can be achieved for the complex geometries considered in this chapter, in particular for 500nm long tips and inclusion depth $d^{(i)} = 1\text{nm}$

Fig. 4.2(a) shows the difference on the results obtained interferometrically before demodulation for two sets of solution of the Maxwell equations, the second using 25 percent more parameters to minimize errors. I plot the modulus of the relative change of the (complex-valued) simulated signal for different positions of the tip, considered static here. A variation smaller that 1 percent is obtained, i.e., for the signal before demodulation, the obtained discrepancies are negligible.

Fig. 4.2(b) shows the simulated signal amplitude for a 1-dimensional scan at the second and third harmonic. The signal amplitude is plotted for the two mentioned sets of solutions, for $d_{\min} = 1\text{nm}$ and oscillation amplitude $\mathcal{A} = 20\text{nm}$. The behavior of the obtained scans is discussed below, I just stress here that both solutions are highly similar,

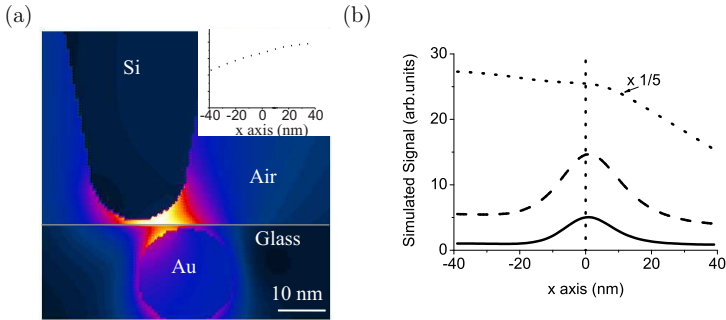


Figure 4.3: (a) Example of the field distribution of the average scattered electric field in the proximity of the tip apex, for 500nm long tip and $d^{(i)} = 1\text{nm}$. The colors indicate values between 0 and 15, the stronger fields in white, where the excitation field strength is 1. The insert indicate the amplitude of the interferometric term of the signal before demodulation, for 1nm distance to the substrate. (b) Example of the obtained amplitude for one-dimensional scans of the samples, for the first (dotted), second (discontinued) and third (continuous) harmonics, the geometry described in (a), $d_{min} = 1\text{nm}$ and $\mathcal{A} = 10\text{nm}$. For visibility, the first harmonic signal is scaled by 1/5.

ultimately giving confidence in the convergence of the demodulated signal obtained in this thesis. The relative difference is, however, still bigger than the very small error in Fig. 4.2(a).

4.2.2 General characteristics of the obtained signal

The tip and the inclusion can interact strongly, and very strong near fields are possible in the gap, as can be seen in Fig. 4.3(a). As indicated in the insert, however, the obtained signal at the far field before demodulation does not present a clear signature of the presence of the inclusion. I illustrate first how for adequate oscillation of the tip ($d_{min} = 1\text{nm}$, $\mathcal{A} = 10\text{nm}$) the near field information from the inclusion can be discriminated at the higher harmonics, and I discuss some peculiarities of *aSNOM* imaging.

The 1-dimensional scans at the first three harmonics are plotted in Fig. 4.3(b). Although not in the first harmonic, the presence of the inclusion is clearly revealed at the second and third harmonics by clear signal maxima. The width of the maxima is much smaller than the wavelength, illustrating the possibility of lateral resolution much

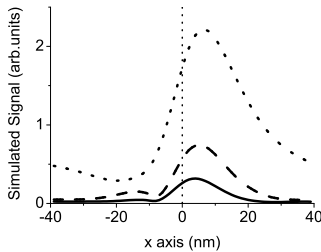


Figure 4.4: One-dimensional scans of the sample when a small spherical tip is considered, for the first (dotted), second (discontinued) and third (continuous) harmonics. $d^{(i)} = 1\text{nm}$, $d_{min} = 1\text{nm}$ and 10nm oscillation amplitude are used.

below the diffraction limit. For a more quantitative study I will use the full width at half maximum $FWHM$. To concentrate on the information with high spatial resolution content, an approximate value for the level of the slowly varying signal for large $|x|$ is subtracted first. More exactly, I subtract the average of the values at $x = -39\text{nm}$ and $x = 39\text{nm}$. This definition is somewhat arbitrary, but its exact form does not seem critical for the cases discussed here. Note that a $FWHM$ was already introduced in Sec. 2.1.3 in a different context, namely the confinement of the fields around the apex for a tip in vacuum.

For Fig. 4.3(b), $FWHM \approx 17\text{nm}$ and $\approx 21\text{nm}$ are obtained for the second and the third harmonic, respectively. The signal contrast between tip close and far from the inclusion is also better for the third harmonic. The second harmonic, however, presents a stronger signal level, so that the optimal choice is not obvious a priori.

4.2.3 Tip length and inclusion depth

aSNOM studies often consider small tips to simplify modeling. In particular, a spherical tip of same radius as the tip apex is frequently discussed. The consequences of this simplification are illustrated with Fig. 4.4, where except for the tip shape identical conditions as in Fig. 4.3(b) were used. Several important differences are observed besides

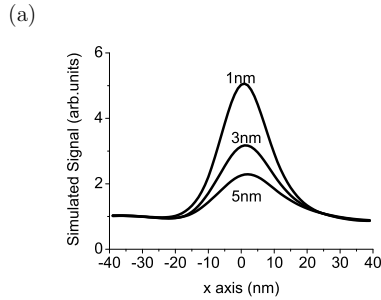


Figure 4.5: Influence of the depth of the inclusion, for the third harmonic, on the amplitude of the signal for 1-dimensional scans. 500nm long tip, oscillation amplitude 10nm and $d_{min} = 1\text{nm}$ are considered.

the expected decrease in received signal (Ch. 3). For example, the central maximum dominates the obtained signal even for the first harmonic.

The maxima obtained are also narrower for the spherical tips. For the given conditions and the third harmonic, the *FWHM* found for the spherical tip is ~ 15 percent smaller than for the long tips at the third harmonic. It is also interesting that the maxima in Fig. 4.4 are *not* situated at $x = 0$, i.e., the asymmetry introduced by the illumination has a strong influence. It differs from the long tip case (Fig. 4.3(a)), where the near field signal is much more symmetric.

The influence of the depth of the inclusion, $d^{(i)}$, is studied next [126, 141]. The simulated images for the long tips are shown in Fig. 4.5. The amplitude of the third harmonic is considered for $d_{min} = 1\text{nm}$ and a 10 nm oscillation amplitude. It is readily seen that the level of signal rapidly diminishes when $d^{(i)}$ is increased, so that the tip-substrate interaction is mostly sensitive to distances less than approximately the apex radius. For 5nm distance, the contrast between the signal for the tip directly over and far from the structure decreases to approximately a third. Not only the signal level diminishes with increasing $d^{(i)}$, but a less narrow maximum is also obtained, from *FWHM* ~ 17 to $\sim 21\text{nm}$ at a distance of 1 and 5nm, respectively.

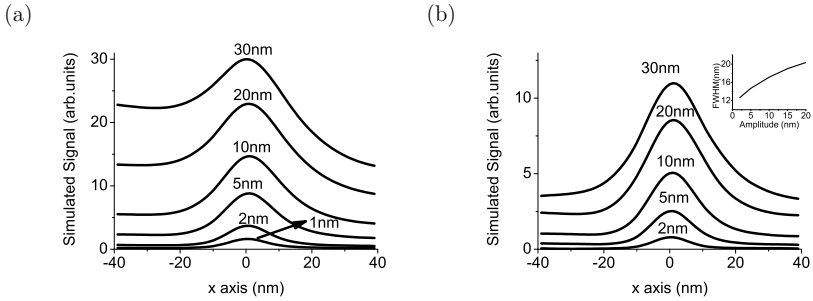


Figure 4.6: Influence of the oscillation amplitude on the obtained signal amplitude for the second (a) and third (b) harmonics. $d^{(i)} = 1\text{nm}$ and $d_{min} = 1\text{nm}$. The insert in (b) shows the influence of the amplitude on the *FWHM* of the central maximum.

4.2.4 Scanning parameters

It was already discussed in Ch. 3 that a correct choice of oscillation characteristics is necessary to properly discriminate the near field information. Approach curves were used there, but as there was no lateral structure the consequences on imaging could not be quantified, the objective of the present subsection. As the limitations of using spherical tips to model typical experiments have just been illustrated, from now on only the 500nm long tips will be considered.

I study first the influence of the oscillation amplitude [41, 129], for $d^{(i)} = 1\text{nm}$ and $d_{min} = 1\text{nm}$. Fig. 4.6(a) shows the second harmonic amplitude for increasing oscillation amplitude. In the infinitesimal amplitude case, the signal will be proportional to the square of the oscillation amplitude. For the smaller amplitudes considered here, up to values on the order of the apex radius, the dependence is weaker than quadratic but still important. For much larger values, however, the main effect is a shift of the whole curves towards larger signal, as the increase for the slowly varying background dominates over the comparatively small change in the near field signal. The ratio between the signal at the maximum and for large values of $|x|$ diminishes, making the discrimination of the near field from the inclusion more difficult.

A similar trend is observed when the third harmonic is considered, Fig. 4.6(b). The

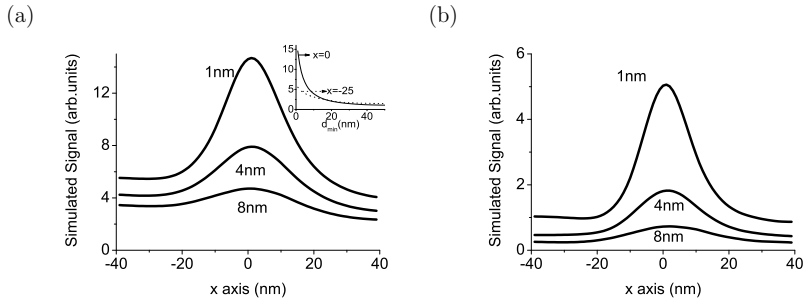


Figure 4.7: Influence of d_{min} on the signal amplitude for 1-dimensional scans at the second (a) and third (b) harmonics. $d^{(i)} = 1\text{nm}$ and the oscillation amplitude is 10nm. The insert in (a) represent approach curves for $x = 0$ and $-x = 25\text{nm}$.

main difference is that slightly bigger oscillation amplitudes are acceptable, up to values on the order of twice the apex radius. The insert illustrates how increasing the amplitude also affects the $FWHM$ [62,64], which in this case is a ~ 60 percent larger for $\mathcal{A} = 20\text{nm}$ than for 2nm.

Next, I consider the influence of changing the minimum distance between tip and substrate d_{min} , for $d^{(i)} = 1\text{nm}$ and 10nm oscillation amplitude [142]. Fig. 4.7 shows the amplitude for second and the third harmonic. Increasing d_{min} rapidly diminishes the overall quality of the detected signal, with the central maximum getting considerably weaker and a moderate increase in the $FWHM$ (at the second harmonic, from $FWHM \sim 21\text{nm}$ at $d_{min} = 1\text{nm}$ to $FWHM \sim 25\text{nm}$ at $d_{min} = 4\text{nm}$). Incidentally, the fast increase of signal observed for decreasing d_{min} even for large $|x|$ points to the presence of a weak but measurable signal from the tip-glass interaction. It is further illustrated by the insert of Fig. 4.7(a), approach curves for the tip at $x = 0$ and $x = -25\text{nm}$. The latter remains approximately unchanged for $-39\text{nm} > x > -25\text{nm}$ indicating that the influence of the inclusion is small. The increase for $x = -25\text{nm}$ and small tip substrate distance, although much smaller than for the tip directly over the substrate, is originated by the tip glass interaction.

Last, an anharmonicity component in the tip oscillation is introduced. As already done in Sec. 3.2, I consider the tip oscillation as not perfectly sinusoidal but according

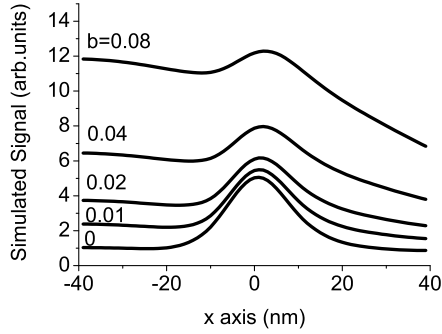


Figure 4.8: Influence on 1-dimensional scans of anharmonic movement of the tip, represented by b . The amplitude of the third harmonic signal is considered, for $d^{(i)} = 1\text{nm}$, $d_{min} = 1\text{nm}$ and 10nm oscillation amplitude.

to equation $d^{(ts)} = d_{min} + A[1 + b + \cos(wt) + b\cos(3wt)]$ where b is the parameter used to change the strength of the anharmonicity. Fig. 4.8 shows the simulated images for the second and the third harmonic, considering $d^{(i)} = 1\text{nm}$, $d_{min} = 1\text{nm}$ and 10nm oscillation amplitude. Already for a value of b of 1 percent, a increase of signal for large x is observed. For a value of b close to 10 percent a dramatic change is observed, with a much less clear central maximum. The change can be attributed to mechanical [61], and not optical, contributions, and is generally undesired for *aSNOM* measurements.

4.3 Discussion and conclusions

In this chapter, I have simulated *aSNOM* imaging in a one-dimensional cut over a patterned sample, in particular a spherical gold inclusion situated in a glass substrate. The influence of several relevant experimental parameters has been discussed. A silicon tip was used, to further illustrate the validity of such tips for *aSNOM*.

I have also discussed the convergence achievable with the numerical method used for this thesis. Although it can be worse for the demodulated results than for the scattered field intensity, it is still very satisfactory. In general, I have observed that changes in

the parameterization of the simulations (e.g., to the number of orders considered in the multipole expansions) for two closely situated tip positions can transfer into an abrupt change of the signal and introduce a significant error into the final demodulated signal. It is convenient to avoid abrupt changes in the way the simulation is being performed when the tip is moved along z .

To judge the quality of *aSNOM* images, the achievable resolution, the strength of the received signal and the degree of discrimination of the information from the inclusion are all relevant. For most of the presented images, the signal amplitude for the tip laterally approaching the position of the inclusion increases sharply, which indicates a very good discrimination of the desired near field information. For large $|x|$, a slowly varying signal is obtained with contributions from the background and the weaker tip-substrate interaction, which can be approximately separated by approach curves like those in Fig. 4.7. In general the signal from tip-glass interaction is weaker than from tip-gold interaction, and if the signal at large $|x|$ and for $x = 0$ are comparable, either the interaction between the tip and the inclusion is small or the background is not suppressed as desired. In simulations, without noise and a perfectly defined geometry, near field information can in principle be also obtained for large background, but this is greatly complicated under typical experimental conditions.

To estimate resolution, I use the width of the central maximum, here quantified by the *FWHM*. Resolution is typically defined as the minimum distance at which two small objects can be distinguished. The obtained *FWHM* does not directly correspond to the definition, but it seems clear that both are closely related, and a *FWHM* as small as possible is desired. As mentioned, an offset has been subtracted before calculating the *FWHM*, to focus on the signature from the inclusion. If this were not done, the cases with large background would show an increased *FWHM*, which would in general accentuate the trends discussed in Sec. 4.2.

A *FWHM* as low as $\sim 12.5\text{nm}$ has been found, less than $\lambda/40$ and on the order of both the tip and sphere diameter. For comparison, a topography image of a 10 nm

radius hemisphere scanned by an AFM tip with 10 nm apex radius will result in *FWHM* more than twice larger, which further illustrates the high resolution achievable with *aSNOM* [143]. In general, to keep the tip close to the inclusion (small \mathcal{A} , d_{min} and $d^{(i)}$) seem favorable to improve the resolution. As an intuitive explanation, a displacement of the tip along x under these conditions results in a fast relative increase of the tip-inclusion distance, and thus a steep reduction of the obtained signal.

I have focused on comparing how the signal level evolves when the characteristics of the substrate or of the scanning are changing. The significance of the absolute level of the obtained signal depends on aspects such as the experimental noise, the intensity of the beams used or how the beams interfere (Ch. 5), which requires further work.

The *FWHM* increases and the signal level sharply decreases for depths of the gold inclusion or d_{min} on the order of half the apex radius or larger. For the geometry here, the signal is thus mostly sensitive to the region close to the interface. *aSNOM* measurements sensitive to larger depths has been predicted [139] and observed [144], but the structures imaged were significantly bigger than in the present study, which add further phenomena such as a modified substrate reflectivity. Larger apex radii could equally result in increased sensitivity to larger depths.

The tip should ideally oscillate close to the substrate, not only to improve resolution but also to strengthen the tip-substrate interaction, and thus the near field signal. Also, a perfect sinusoidal movement of the tip is desired, at least if no alternative scheme is utilized to separate optical and mechanical contributions. Both are not completely independent in a realistic experimental set-up: if the attempt to reduce d_{min} results in too strong a contact between the tip and the surface, anharmonicities in the tip movement and fast wear of the tip apex ensue [61].

It is not possible to give an optimal value of oscillation amplitude valid for all experimental conditions, even considering ideal oscillation. A small value reduces the *FWHM* and improves the background suppression, but it also considerably diminishes the level of signal. Ideally, one would desire to use the smallest amplitude that results in a suffi-

cient signal to noise ratio. As a coarse rule, amplitudes on the order of the apex radius seem a reasonable compromise for the presented geometry.

Notice also that for the same oscillation amplitude, the third harmonic can result in better background suppression and smaller *FWHM* but also in smaller signal level. For a given value of desired signal, it is generally possible to use a smaller oscillation amplitude for the second than for the third harmonic. Simulations like those presented here are useful to determine the optimal choice. For example, if $d_{min} = 1\text{nm}$ and $d^{(i)} = 1\text{nm}$, imaging at the second harmonic with 5nm oscillation amplitude result in a similar image than 20nm oscillation amplitude at the third harmonic, except that the *FWHM* is a ~ 10 percent smaller. In this particular example, the second harmonic measurement is slightly favorable.

The results in this chapter also allow to study significant limitations of models considering short tips. A clear near field signature is achievable for both short and long tips, but significant differences exist. As expected, both background and near field signal increase markedly for the long tips. The background increases in a bigger proportion, though, and discriminating the near field information is more challenging. Further, the central maximum presents a clear asymmetry with respect to $x = 0$ for the spherical, but much smaller for the 500nm long, tips. In particular, considering a short tip induces to expect a shift between the position of the inclusion and the measured signal maximum, shift likely to be quite small in typical experimental measurements. The asymmetry is introduced by the illumination and is small for the long tips, whose axis contribute an additional symmetry. Last, a better *FWHM* is observed for the spherical tips, which points to the interaction being more spatially confined for short tips [145] and reminds of their larger field confinement observed in vacuum(Sec. 2.1.3).

I expect the shape of the tip apex to be a critical parameter for the discussed results [126]. It will influence, for example, the achievable resolution, the sensitivity for sub-surface imaging or the optimal amplitude. Due to this, many results have been discussed not only on absolute terms, but relating them to the apex radius.

This chapter studies imaging in *aSNOM*, including signal demodulation. I show the shortcomings of using the spherical tip approximation and obtain demodulated images for long tips. For the given conditions, the near field signal is sensitive to the first nanometers of the substrate. A very good discrimination of the local information from the inclusion is possible for small oscillation amplitude, scanning close to the substrate and highly harmonic tip oscillation. Simulating scans along 2 dimensions is a natural next step, but it could not be subject of this thesis due to the the high computational requirements.

Chapter 5

Studying the detector response: Interferometric measurement over extended areas for oscillating tips

Up to now, I have directly used Eq. (1.1) to simulate the demodulation. I derive in the present chapter this equation, and discuss in more detail how the optical phase and optical amplitude combine over the whole area of the detector to result in the measured value. I show that failing to account for the phenomena involved can easily result in inaccurate predictions.

5.1 The model

5.1.1 The considered geometry

Different scenarios will be considered in this chapter, including the interference between idealized beams or the scan of a beam focus by the tip. The most complex scenario, in which the strong interaction between a tip and a sample is of interest is illustrated in Fig. 5.1. The sample is homogeneous gold (Ch. 3), or a gold inclusion inserted in a glass substrate (Ch. 4). The fields are collected by a lens considered perfect.

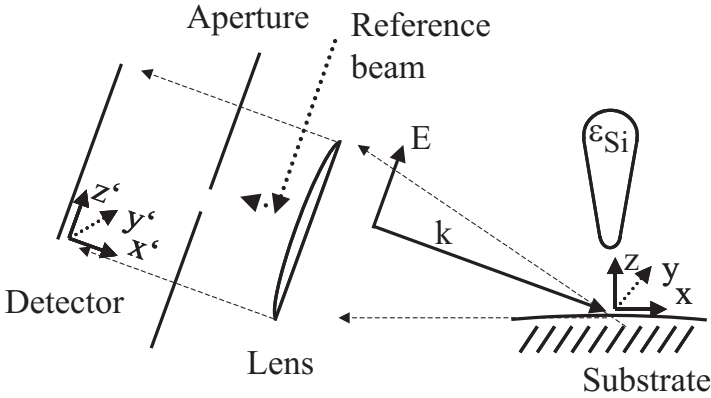


Figure 5.1: Illustration of geometry used in this chapter. The scattered radiation is collected by a lens and detected at the photodetector, usually after going through an aperture. The reference beam is included for interferometric detection. To ease the discussion, I define one axis system over the substrate and a second where the detector is placed.

Most relevant parameters have already been discussed in Sec. 1.2. Here, it will be of interest to obtain the local fields at each position \vec{r} of the detector area. This is equivalent to considering a quadratic aperture which blocks most of the cross section of the parallel beam. Both infinitesimal and finite apertures will be considered in this chapter. As discussed, I consider only the component of the electric field contained in the plane of incidence of the detector for the interferometric signal and I ignore the constant contribution from the substrate (but not from the inclusion).

5.1.2 Modeling the detector response for each tip position

The expression used for the signal generated by a photodetector is derived here. I first consider the signal generated by the detector for a particular position of the AFM tip. The effect of oscillating the tip and detecting at the n -th harmonic of the tip frequency is included next.

I start by considering the contributions to the total photocurrent from each areal detector element. They are assumed to be proportional to the square of the local field

modulus

$$\mathcal{I}(\vec{r}, d^{(ts)}) \propto |\vec{E}_{ref}(\vec{r}) + \vec{E}_{scat}(\vec{r}, d^{(ts)})|^2 \quad (5.1)$$

where \vec{E}_{scat} refers to the fields scattered by the tip-sample system, \vec{E}_{ref} to the fields from an external reference source, and \mathcal{I} to the signal generated by the photodetector. I include explicitly the dependence on tip position $d^{(ts)}$ and the location \vec{r} of the photodetector element. In the following, I will use $\vec{E}_{scat} = |E_{scat}| \exp i(\Omega t + \Theta_{scat}) \hat{e}$ and $\vec{E}_{ref} = |E_{ref}| \exp i(\Theta_{ref} + \varphi) \hat{e}$. As was mentioned, I only consider the component of the fields contained in the plane of incidence (linear polarization along \hat{e}). The phase of the reference beam is divided into the absolute part, Θ_{ref} , which is constant for a given tip position and depends on the exact experimental conditions, and the relative phase φ , which can be well controlled by changing the path length difference at the interferometric arms and will be useful for homodyne detection ($\Omega=0$). $\Omega \neq 0$ refers to the finite difference in frequency between the two beams used in a heterodyne scheme.

In typical experiments, $|E_{ref}| \gg |E_{scat}|$ and only the interferometric term $\vec{E}_{scat} \cdot \vec{E}_{ref}$, where the second factor is the complex conjugate of \vec{E}_{ref} , is both significant and dependent on $d^{(ts)}$. The signal obtained can be written as

$$\mathcal{I}(\vec{r}, d^{(ts)}, t) \propto \mathcal{I}_0(\vec{r}, d^{(ts)}) \cos(\Omega t + \Theta(\vec{r}, d^{(ts)}) - \varphi) \quad (5.2)$$

in which $\mathcal{I}_0 = |E_{scat}| |E_{ref}|$ and $\Theta = \Theta_{scat} - \Theta_{ref}$ have been redefined to lighten the notation. Although the signal from Eq. (5.1) will be positive, Eq. (5.2) refers to the interferometric component and can be both positive and negative, relative to the large constant contribution from $|E_{ref}|^2$. Contributions from different positions \vec{r} can thus partially cancel, which turns out to be important for experiments.

Finally, I obtain the signal from the complete area of the detector as an integral over the different contributions

$$\mathcal{I}^*(d^{(ts)}, t) \propto \int_{A_{det}} \mathcal{I}(\vec{r}, d^{(ts)}, t) dr \quad (5.3)$$

It includes the influence of the interferometric phase and the extended nature of the detector. This expression is strictly valid only for a static tip, but it is an excellent approximation as long as the tip movement ($\sim 10^5$ Hz) is much slower than the time dependence of the optical field ($\sim 10^{15}$ Hz), which is clearly verified in experiments. Under such circumstances, the only change in Eq. (5.3) is that $d^{(ts)}$ is a function of time.

5.1.3 Modeling the detector response for an oscillating tip

In *aSNOM* the tip is typically oscillated at a frequency $w \sim 10^5$ and the n -th harmonic signal is measured. The signal obtained under such conditions is analyzed here.

To detect the n -th harmonic signal, a lock-in amplifier is used with a reference frequency $\Omega + nw$, where $\Omega \sim 10^8$ is included for heterodyne detection ($\Omega = 0$ for homodyne detection). The lock-in response is modeled by the integral $\frac{1}{T} \int_0^T \mathcal{I}(t) \exp(i(\Omega t + nwt + \Theta_{lock})) dt$. The result is a complex number, which carries information about both the amplitude and the phase. Θ_{lock} is a phase shift between the electric reference signal and the internal phase of the lock-in amplifier, which will just add to the final phase. Experimentally, T is often an interval much larger than the periods associated with Ω and w . Considering Eq. (5.3), a very general expression is directly obtained

$$H_n = \frac{K}{T} \int_0^T \int_{A_{det}} \mathcal{I}_0(\vec{r}, d^{(ts)}) \cos(\Omega t + \Theta(\vec{r}, d^{(ts)}) - \varphi) e^{i(\Omega t + nwt + \Theta_{lock})} dr dt \quad (5.4)$$

The movement of the tip is often modeled as an oscillation along the z axis described by $d^{(ts)}(t) = d_{min} + \mathcal{A}[1 + \cos(wt)]$, where d_{min} is the position of the tip when closest to

¹The sign of the exponential can be chosen as positive or negative, and depends on the particular implementation of the lock-in.

the substrate, \mathcal{A} the oscillation amplitude and w the corresponding angular frequency. However, the equations obtained in this section apply to generic periodic movements, i.e., they also describe the case of anharmonic motion.

Eq. (5.4) can be further developed for two relevant experimental set-ups, heterodyne interferometry and a homodyne scheme that uses two measurements in quadrature. I will show that for typical conditions they result in exactly the same algebraic expressions: Which set-up to use is then a question of experimental convenience. The heterodyne scheme requires two beams of slightly shifted frequencies, while the homodyne scheme needs two successive measurements.

Heterodyne detection scheme

The heterodyne case corresponds to Eq. (5.4) for two beams of different frequency ($\Omega \neq 0$). Here φ is constant and is considered to be zero. Writing the cosine as a sum of two exponentials, two terms of the form $\exp[i(2\Omega t + nwt + \Theta_{lock} + \Theta(r, d^{(ts)}))]$ and $\exp[i(nwt + \Theta_{lock} - \Theta(r, d^{(ts)}))]$ appear in the time integral. The first exponential integrates to zero for large T and the final expression is obtained

$$H_n \propto \frac{e^{i\Theta_{lock}}}{2T} \int_0^T \left[\int_{\mathcal{A}_{det}} \mathcal{I}_0(\vec{r}, d^{(ts)}) e^{-i\Theta(\vec{r}, d^{(ts)})} dr \right] e^{inwt} dt \quad (5.5)$$

which corresponds to Eq. (1.1) and completes the derivation.

Homodyne detection scheme

Homodyne schemes are characterized by $\Omega = 0$. The path length phase difference φ is assumed controllable by changing the optical path of one of the beams. I consider a typical technique which combines at each pixel two measurements taken for φ and $\varphi + \pi/2$. Alternative techniques modulate φ continuously, or measure for more than two values of φ , but the general concept is similar [146]. More explicitly, I define the final signal as $H_n(\varphi = 0) \pm iH_n(\varphi = \pi/2)$, where each term refers to the result of Eq. (5.4)

for the corresponding value of φ . The resulting expression is of the form

$$H_n \propto \frac{1}{T} \int_0^T \left[\int_{A_{det}} \mathcal{I}_0(\vec{r}, d^{(ts)}) [\cos(\Theta(\vec{r}, d^{(ts)})) \pm i \sin(\Theta(\vec{r}, d^{(ts)}))] dr \right] e^{i(n\omega t + \Theta_{lock})} dt \quad (5.6)$$

The cosine and sine terms can be combined into a complex exponential. If the minus sign is chosen, Eq. (5.5) is again obtained, which shows the fundamental equivalency of homodyne and heterodyne detection schemes. This only holds as long as the signal from the interferometric term predominates, an assumption typically verified for *aSNOM* measurements. Notice also the equality only holds because measurements from several values of φ are combined, otherwise homodyne and heterodyne measurements present considerable differences [147].

5.2 Results

In this section, I first compare briefly interferometric and noninterferometric detection. Afterwards, I emphasize three aspects of the former that can be deduced from Eq. (5.5) and that are important for measurements. First, in addition to the intensity, the phase is also modulated by the oscillation of the tip. Secondly, the change of phase over the area of the detector results in constructive and destructive interferometric contributions to the integral which diminishes the magnitude of the total signal. And last, as the fields are in general a function of \vec{r} , using an aperture to select a particular area affects the signal generated by the photodetector. I will consider here several experimentally relevant situations which serve to illustrate the importance of these phenomena for *aSNOM*. Instead of directly evaluating the complex Eq. (5.5), I will select for each example the terms responsible for the effect under analysis.

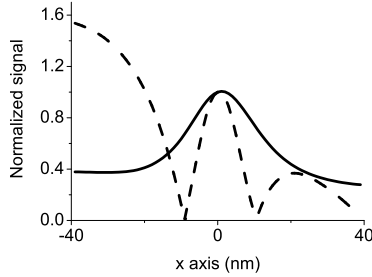


Figure 5.2: Simulated amplitude detected for a scan over a gold inclusion, as described in Ch. 4. Second harmonic demodulation, $\mathcal{A} = 10\text{nm}$, $d^{(i)} = 1\text{nm}$ and $d_{min} = 1\text{nm}$ were considered. The traces are normalized to the values at $x = 0$. The continued line corresponds to interferometric detection, and the dashed to noninterferometric detection.

5.2.1 Interferometric and noninterferometric detection

Interferometric detection is used throughout this thesis, because it typically results in a stronger signal and allows to obtain information about the optical phase. I discuss here how images obtained with an interferometric and a noninterferometric scheme can differ even qualitatively, with the near field signal from a gold inclusion more easily detected with the interferometric scheme [128].

Writing the lock-in amplifier response as $H_n \propto 1/T \int_0^T \mathcal{I}^* \exp(in\omega t)$, $\mathcal{I}^* = \int_{A_{det}} \mathcal{I}_0(\vec{r}, d^{(ts)}) e^{-i\Theta(\vec{r}, d^{(ts)})} d\vec{r}$ corresponds to an interferometric scheme (Eq. (5.5)). For noninterferometric detection, $\mathcal{I}^* = \int_{A_{det}} \overrightarrow{S(r, d^{(ts)})} d\vec{A}$ is considered, i.e, the integral of the Poynting vector average over the area of the detector.

I illustrate in Fig. 5.2 the simulated amplitude obtained for interferometric and noninterferometric scans over a gold inclusion. For the interferometric measurement, the maximum from the tip-inclusion interaction clearly dominates the demodulated signal. A very different behavior is observed for the noninterferometric scheme, where a signature of the interaction appears near $|z| = 0$ but is not the global maximum of the signal for the scanning conditions chosen. It seems easier to discriminate the near field signal from the background for the interferometric scheme.

5.2.2 Phase modulation for an oscillating tip

For lock-in detection and sufficiently low oscillation amplitude, a Taylor series expansion of the signal as a function of tip position can be used to express the n -th harmonic as proportional to the n -th derivative, in the direction of oscillation of the tip, of the complex valued signal generated at the detector. However, the amplitude read at a lock-in amplifier is *not* proportional to the n -th derivative of the optical amplitude, which is shown here by explicitly dividing the complex-valued signal into real valued amplitude and phase. I obtain an analytical expression for the scan of beams in vacuum which serves to illustrate the consequences of the phase modulation to experiments, also under more general conditions. Some of the phenomena have also been discussed in [148].

As I am not interested here in the spatial field distribution over the detector area, I write Eq. (5.5) as

$$H_n \propto \frac{1}{T} \int_0^T |\mathcal{I}^*(d^{(ts)})| e^{-i\Theta^*(d^{(ts)})} e^{i(n\omega t + \Theta_{lock})} dt \quad (5.7)$$

in which $|\mathcal{I}^*|e^{-i\Theta^*}$ represents the result of the integration over r . At this level of analysis, it is enough to know that they depend on the position of the oscillating tip (and thus on time).

Planar waves

I consider a simple case first, in which the amplitude of the fields $|\mathcal{I}^*(d^{(ts)})| = |\mathcal{I}^*_{cte}|$ is kept constant and the phase $\Theta^*(d^{(ts)})$ is considered to vary linearly with the phase. This corresponds to a tip in vacuum under planar illumination. Assuming a perfectly harmonic movement of the tip, $\Theta^*(d^{(ts)}) = \Theta_{lock} - \alpha + \beta \mathcal{A} \cos(i\omega t)$, where α and β are real constants. Eq. (5.7) becomes

$$H_n \propto \frac{1}{T} \int_0^T |\mathcal{T}_{cte}^*| e^{imwt+i\alpha-i\beta A \cos(iwt)} dt \quad (5.8)$$

Using the equality

$$e^{-i\beta A \cos wt} = \sum_{m=-\infty}^{\infty} i^{-m} J_m(\beta A) e^{-imwt} \quad (5.9)$$

where J_n is the bessel function of order n , a sum of terms appears in the integral. All integrate to zero except for $m = n$ and finally

$$H_n \propto i^{-n} |\mathcal{T}_{cte}^*| e^{i\alpha} J_n(\beta A) \quad (5.10)$$

Even in the considered case of constant amplitude of the fields, the phase modulation results in a signal contribution from all the harmonics. The amplitude for the n -th harmonic is proportional to the field amplitude (and not its derivatives, as when complex-valued signals are considered) and to the Bessel function of order n , $J_n(\beta A)$. $|\beta A|$ may be interpreted as the change of phase from the center to the outer points of the oscillation.

The obtained equation is illustrated in Fig. 5.3, in which the evolution of the different harmonics as a function of the amplitude is plotted. Although the illumination is not strictly planar, it varies sufficiently slowly for Eq. (5.10) to be approximately valid. An excellent fit is obtained, with the slightly bigger deviation in the zeroth harmonic probably due to residual background contributions. Only two fitting parameters have been used for the four plots, β and a scaling factor for the intensity. A proportional error between the estimated and the real oscillation amplitude (Sec. 6.3) is also corrected by the fitting of β . Notice that if β is known, the obtained curves may be used to calibrate the oscillation amplitude ([149]).

Gaussian beams

To illustrate the behavior of the solution for spatially variable amplitude of the field, I choose an example which is relevant for experiments and which allows to obtain a

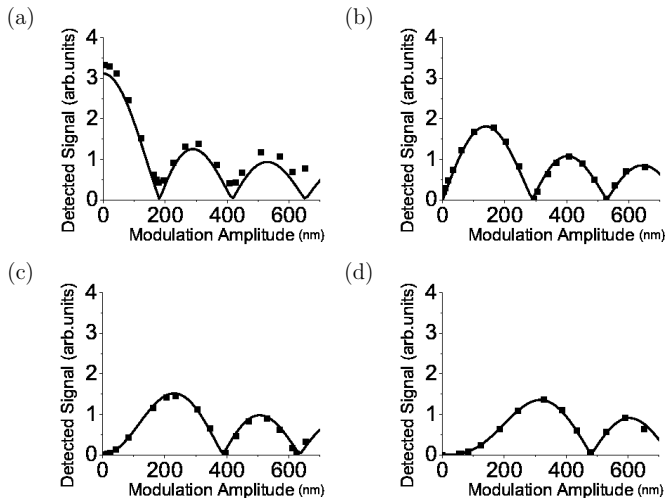


Figure 5.3: Theoretical (line) and measured (dots) modulus of the signal amplitude detected from a harmonically oscillated tip under weakly focused illumination. The oscillation amplitude is changed for the (a) 0th, (b) 1st, (c) 2nd and (d) 3rd harmonics. One set of two parameters was used to fit all the curves

relatively simple analytical expression: the scan of a weakly focused beam by a tip whose oscillation amplitude is sufficiently small. Such scans can be useful for the correct optical alignment (Sec. 6.2).

In the considered scenario, $|\mathcal{I}^*|$ is assumed proportional to the local fields at the apex at least for illumination polarized in the plane of incidence (plane xz)². Scanning a beam thus serves to characterize its field distribution. I develop $|\mathcal{I}^*|$ in a Taylor series around the center of oscillation and assume sufficiently small oscillation amplitude, \mathcal{A} , obtaining

$$|\mathcal{I}^*(t)| = \sum_{k=0}^{\infty} \frac{1}{2^k k!} \mathcal{I}^{*(k)} \mathcal{A}^k \cos(kwt) \quad (5.11)$$

where $\mathcal{I}^{*(k)}$ refers to the k th derivative. For a sufficiently weakly confined beam, the variation of the phase with tip position may be modeled as linear. If the exponential

²From Sec. 2.1.2 and assuming that the integral over the field amplitude is proportional to the square root of the integral over the intensity A correction could be present for inhomogeneous field distribution (Secs. 5.2.3, 5.2.4).

$\exp(-i\Theta^*(d^{(ts)}))$ is expanded again in a series of Bessel functions,

$$H_n \propto \frac{e^{i\alpha}}{T} \int_0^T \sum_{k=0}^{\infty} \frac{1}{2^k k!} \mathcal{T}^{*(k)} \mathcal{A}^k \frac{e^{ikwt} + e^{-ikwt}}{2} e^{inwt} \sum_{m=-\infty}^{\infty} i^{-m} J_m(\beta\mathcal{A}) e^{-imwt} dt \quad (5.12)$$

is obtained. Only the terms $k = |m - n|$ remain after the integration for large T , which gives

$$H_n \propto \frac{e^{i\alpha}}{2} \left[\mathcal{T}^{*0} i^{-n} J_n(\beta\mathcal{A}) + \sum_{m=-\infty}^{\infty} \frac{1}{2^{|m-n|} |m-n|!} \mathcal{T}^{*(|m-n|)} \mathcal{A}^{|m-n|} i^{-m} J_m(\beta\mathcal{A}) \right] \quad (5.13)$$

The first term of the sum accounts for the special case $m = n$. As expected, the obtained equation simplifies to Eq. (5.10) in the limiting case of infinitely slow spatial variation of the fields ($\mathcal{T}^{*(|m-n|)} \rightarrow 0$ for $m \neq n$). However, when the derivatives cannot be ignored, the amplitude and the phase read in a lock-in amplifier will be a complex combination of contributions from both the optical amplitude and phase. Even for small oscillation amplitudes, the n -th harmonic is not simply proportional to the n -th derivative of the (real valued) optical amplitude. Also, the phase read at the lock-in amplifier is in general not simply the phase at the center of oscillation.

Illustrate next how Eq. (5.13) helps to interpret experimental scan images of focused beams. Considering only the terms of order \mathcal{A} for the first harmonic, and remembering that $J_m(\beta\mathcal{A})$ is of order \mathcal{A}^m for small amplitudes, the first harmonic can be written

$$H_1 \propto \frac{e^{i\alpha}}{2} \left[\frac{1}{2} \mathcal{T}^{*(1)} \mathcal{A} J_0(\beta\mathcal{A}) - 2\mathcal{T}^{*(0)} i J_1(\beta\mathcal{A}) \right] \quad (5.14)$$

For sufficiently slow variation of the fields, the first term may be ignored and the measured signal is basically proportional to $\mathcal{T}^{*(0)}$ and thus to the local fields. Such behavior can be seen in Fig. 5.4(a), a typical first harmonic scan near the focus. It does indeed look like an oblique (to account for the angle of incidence) cut through the focus of a

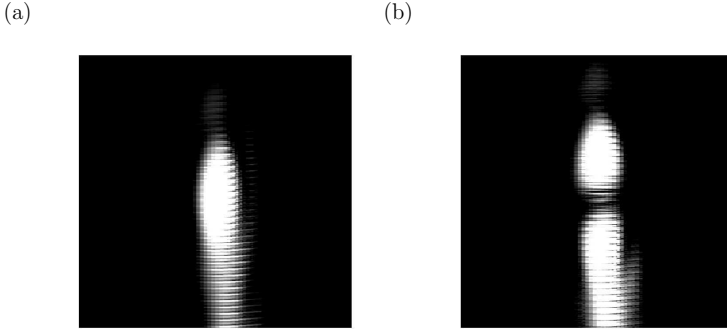


Figure 5.4: Scans of the beam at the first harmonic. (a) represents a typical scan, (b) has been done under the same conditions as (a) but with an oscillation amplitude close to the first zero of the Bessel function of zeroth order. The signal is considerably weaker in (b), and different color scales are used for better visibility. The image size is $20 \times 20 \mu\text{m}$ in both cases.

Gaussian beam.

However, if the oscillation amplitude is chosen such that the first order Bessel function approximately cancels (and assuming that it is still small enough for Eq. (5.14) to be valid), the signal is then approximately proportional to the derivative of the field. Fig. 5.4(b) illustrates how the image obtained can indeed completely change. Two lobes are now obtained, with a minimum near the position where the maximum was found before. Notice that at the position of the focus, a global maximum, the first derivative is indeed expected to cancel.

5.2.3 Phase distribution over the detector

In this section I examine some consequences of the dependence of the fields on the position at the detector \vec{r} . In particular, the absolute value of

$$\int_{A_{det}} \mathcal{I}_0(\vec{r}, d^{(ts)}) e^{-i\Theta(\vec{r}, d^{(ts)})} d\vec{r} \quad (5.15)$$

can be much smaller than for a constant phase. The reason is that the phase can vary quickly between 0 and π radians, and constructive and destructive contributions

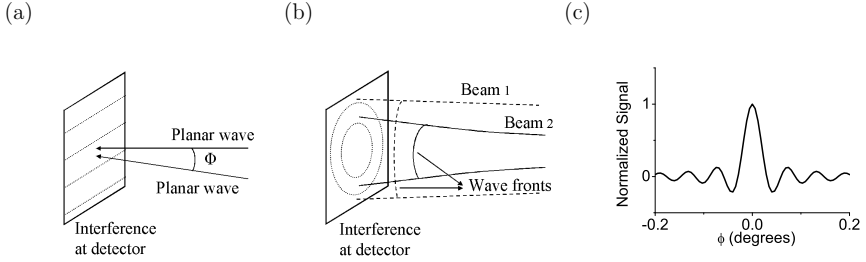


Figure 5.5: Scheme illustrating the interference between (a) two planar waves with slightly different incidence angle and (b) two gaussian beams with wave fronts of different radius of curvature. Linear (a) and concentric (b) fringes can be observed at the detector due to the succession of constructive and destructive interference. (c) represents the evolution of the integral over the area of the detector in the scenario illustrated in (a), as a function of ϕ

will partially cancel. Notice that although the contribution from each position of the detector will be positive for the complete signal, only the interferometric term is being discussed here, which can be both positive and negative.

Phase distribution for planar waves and gaussian beams

I begin with some examples which are not specific to aSNOM but more general to interferometric measurements. They are well known and I discuss them only briefly here. First, I consider two planar waves that are identical except for a slightly different propagation direction. This scenario is sketched in Fig. 5.5(a). An interference pattern is observed at the detector, with bright (dark) horizontal fringes at the positions of constructive (destructive) interference. The integral over the interferometric term Eq. (5.15) is proportional in this case to

$$\mathcal{I}^*(d^{(ts)}) \propto a \frac{\sin\left(|\vec{k}| \frac{a}{2} \sin(\phi)\right)}{|\vec{k}| \frac{a}{2} \sin(\phi)} \quad (5.16)$$

where ϕ refers to the difference of angle between the beams and a to the lateral size of the detector. The detector is normally much bigger than the wavelength ($|\vec{k}|a \gg 1$), and even for relatively small values of ϕ the complex exponential oscillates very fast and contributions with π radians phase difference cancel. As an example, the dependence of

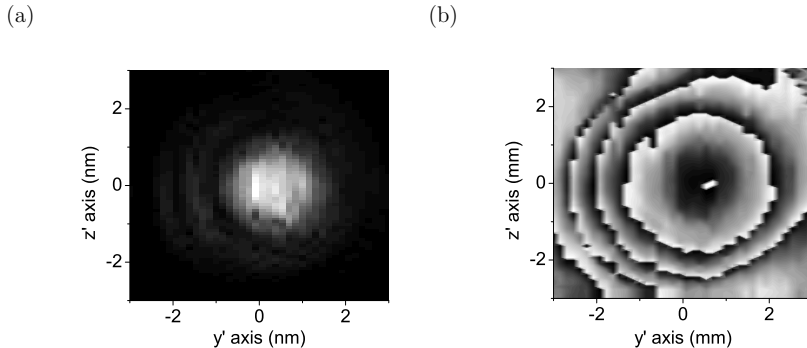


Figure 5.6: Measured amplitude (a) and phase (b) of the signal at the photodetector by changing the place of an iris blocking the beam except at the desired area. The scattered beam was collected by a lens with solid angle $NA \sim 0.25$. $\lambda \sim 865\text{nm}$.

the integral with ϕ is plotted in Fig. 5.5(c), for $\lambda = 514\text{nm}$ and $a = 1\text{mm}$.

Next, I consider two parallel gaussian beams, as schematically shown in Fig. 5.5(b). Real beams cannot be perfectly collimated, and thus the wave fronts exhibit finite curvature radii. If these values differ between the two beams used, the phase difference will not be constant over the area of the detector. For otherwise identical beams, concentric interference rings appear. Positive and negative contributions to the integral ensue again, and the total total signal generated by the photodetector will be smaller than for constant phase difference.

Both effects may in principle be avoided with an adequate beam alignment. Fig. 5.6 illustrates a typical situation in my measurements in which a perfectly constant phase is not achieved, as will be discussed in Ch. 6. I used an iris to block the beam except in a small region, which allows for a spatial map of both the amplitude (Fig. 5.6(a)) and the phase (Fig. 5.6(b)) of the interferometrically measured signal. The phase is projected onto the interval $[0..360)$, which explains the abrupt jumps on the signal. It illustrates the radial variation expected from the previous discussion. At the center of this radial pattern the phase changes slowly, the signal integrates (mostly) constructively over all the area of the used iris and a strong lock-in amplitude signal is obtained. Under the

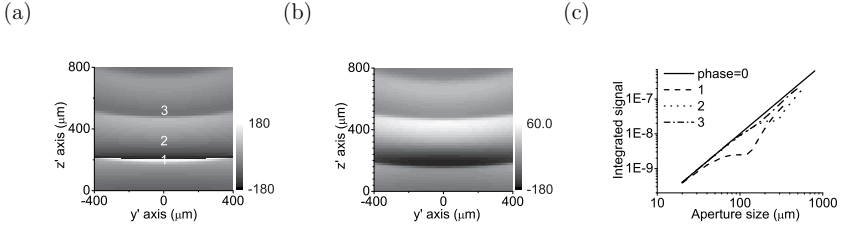


Figure 5.7: Calculated phase ($-\Theta_{scat}$) distribution at the detector for a tip over a gold inclusion in a glass substrate for the tip situated at (a) 1nm and (b) 50nm above the substrate. The inclusion is at depth $d_{min} = 1\text{nm}$, and the tip at $x = y = 0$. (c) Signal detected considering just the phase distribution on (a), as a function of the size of the side of an aperture used to block most of the beam. The different curves corresponds to changing the position of the aperture, the numbers referring to the locations indicated in (a). “phase=0” correspond to the idealized case in which the phase is constant over the detector.

conditions plotted here, increasing the size of the iris will not increase the signal from the photodetector if the additional signal is of opposite sign.

Phase distribution for the backscattered beam

For perfect alignment and gaussian beams, it is possible to obtain a constant phase difference over the complete area of the detector. However, this could be impossible in an aSNOM measurement, as the fields scattered by the tip-substrate system can present a complex spatial variation that depends on the tip position. To study this case, the scattered fields calculated for the geometry illustrated in Fig. 5.1 are used.

The phase distribution of the scattered fields on the detector is represented in Fig. 5.7(a) for a 500nm long tip. The sample consists of a glass substrate with a spherical gold inclusion at depth $d_{min} = 1\text{nm}$. The tip is situated 1nm above the substrate directly over the inclusion(Ch. 4).

The observed phase is not homogeneous, but presents a fringe-like pattern. Moreover, the phase distribution depends on the exact experimental conditions, as illustrated in Fig. 5.7(b). Here, the tip has been displaced to a 50nm distance to the substrate, where no strong near field interaction is present. The main difference between both distributions is a larger variation of the phase in Fig. 5.7(a) for $z' \sim 200\mu\text{m}$. I have also

verified that for a tip at a 1nm distance of a homogeneous gold substrate, horizontal fringes are still obtained on the phase distribution, but the variation of the phase over the area of the detector is slower than for the gold inclusion.

To illustrate the consequences of the phase distribution, I simplify $\mathcal{I}_0(\vec{r}, d^{(ts)})$ in Eq. (5.15) to a constant and set the phase of the reference beam to zero. A term of the form $\int_{A_{det}} e^{-i\Theta_{scat}(r, d^{(ts)})} dr$ is left, A_{det} corresponding here to the area of the aperture in Fig. 5.1. The module of this integral will be smaller than for a constant phase. In particular, contributions to the integral with a π radians phase difference will add up destructively

The behavior of the module of the integral is illustrated in Fig. 5.7(c), for the phase distribution from Fig. 5.7(a). The integral is calculated as a function of aperture size, for three different positions of the aperture, all for $y' = 0$ and for increased values of z' . For comparison, I also obtain the signal to be obtained for a homogeneous phase distribution. As expected, the signal for a realistic phase distribution and finite aperture is smaller than if the phase were constant all over the detector. In some cases, a larger aperture does not result in a noticeable larger signal.

5.2.4 Location of the detector area element

I concentrate here on another important consequence of the dependence of the fields on \vec{r} [150]. The inhomogeneity of the field distribution has been suggested to improve the *aSNOM* signal to noise ratio [151]. I show here for a realistic imaging scenario, including demodulation, how the position of the aperture can affect the simulated images not just with a uniform global factor in the intensity but also pixel by pixel with a variable factor.

With this goal in mind, I calculate the demodulated signal obtained from the detector element at \vec{r}

$$H_n(\vec{r}) \propto \frac{1}{T} \int_0^T \mathcal{I}_0(\vec{r}, d^{(ts)}) e^{-i\Theta(\vec{r}, d^{(ts)})} e^{im\omega t} dt \quad (5.17)$$

It corresponds to considering a minute aperture whose position is being changed. The

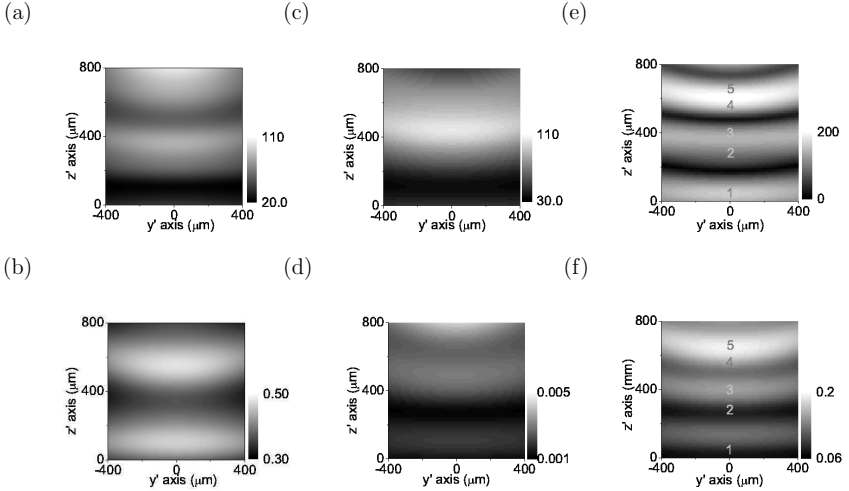


Figure 5.8: Distribution of the amplitude of the signal over the detector, in arbitrary units. The first row correspond to the continuous component, and the second to the signal demodulated by the lock-in amplifier for the third harmonic. For the demodulation, an oscillation amplitude of 10nm is considered. (a,b) correspond to a tip strongly interacting with a homogeneous gold substrate, with the minimum distance $d_{min} = 1\text{nm}$ and (c,d) to $d_{min} = 100\text{nm}$. (e,f) correspond to a tip directly, $d_{min} = 1\text{nm}$, over a gold inclusion situated in a glass substrate at 1nm depth, $d^{(i)}$. The positions marked will be used as a reference in later graphs.

phase and module of the reference beam is assumed to be constant over the area of the detector and polarized along the z' axis. The amplitude and phase for the scattered beam are simulation results, where also the z' component is considered.

Fig. 5.8(a) shows the amplitude of the continuous component generated by the photodetector (equivalent to calculating H_0 in Eq. (5.17)) as a function of \vec{r} for a $1.4\mu\text{m}$ long tip situated at 1nm distance above a gold substrate. Fig. 5.8(b) shows the distribution of the third harmonic signal for a 10nm oscillation amplitude and $d_{min} = 1\text{nm}$. In both cases, fringe-like patterns parallel to the horizontal y' direction appear [151], with clear changes along the z' axis. The positions where maximum and minimum signal is obtained is however a function of the harmonic. The first and the second harmonic present also fringe-like patterns, with the second harmonic being similar to the third.

The field distribution also depends strongly on other experimental parameters.

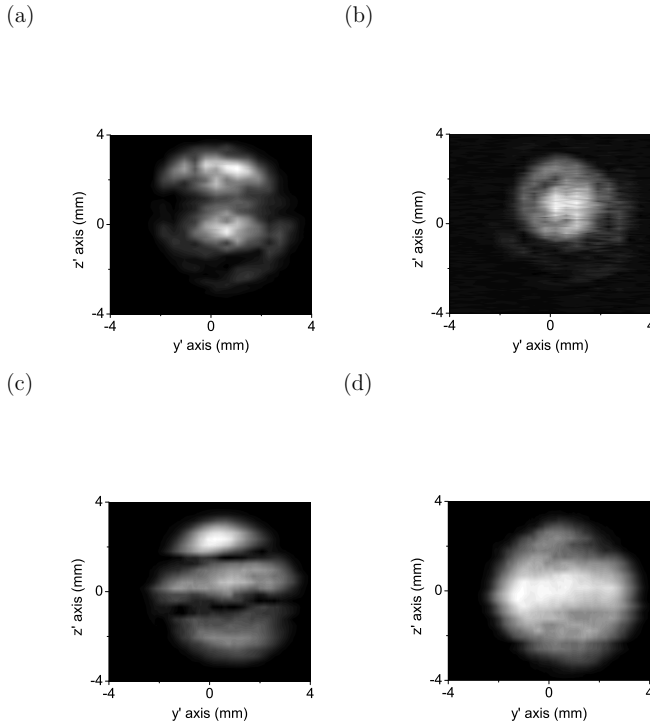


Figure 5.9: Spatial distribution of the fields at the detector, measured by displacing the position of an aperture and recording the amplitude read at the lock-in amplifier. (a,b) are measured with the tip oscillating close to a metallic substrate, for the first (a) and third (b) harmonics. (c) correspond to the first and (d) to the second harmonic without a closely situated substrate for noninterferometric detection. Commercial Silicon tips are used; in (a,b) the native oxide layer have been etched to increase the strength of the interaction between the tip and the substrate. $\lambda \sim 820\text{nm}$ is used. The scattered beam was collected by a lens with solid angle $NA \sim 0.25$. Different color scales are used in the images.

Fig. 5.8(c,d) show the continuous component and third harmonic over the area of the detector for conditions as before except $d_{min} = 100\text{nm}$. Fig. 5.8(e,f) are the equivalent plots for the tip strongly interacting with a spherical gold inclusion in a glass substrate. Fringes are always obtained, but their width, visibility and the position of the minimum and maximum depend on the exact conditions considered. In particular, a faster variation along z' is observed for the tip over the gold inclusion than over the homogenous gold. Notice that the third harmonic signal for short tip-substrate distance is dominated in both cases by a very similar physical phenomenon, the near field interaction between a silicon tip and a gold structure.

I have found experimental indications of some of the phenomena above. Fig. 5.9(a,b) show the field distribution measured interferometrically for the first and third harmonics, for a tip oscillating directly over a metallic substrate. Fig. 5.9(c,d) represent a different set of measurements for the first and second harmonic without any closely situated sample, measured noninterferometrically, which avoids the complications involved in optimizing the interferometry over a large area of the cross section of the beam. Each pixel corresponds to a different position of an iris which blocks the scattered and reference beam except for the area to be measured. As in the simulations, the positions of the maxima and minima of the signal are a function of the observed harmonic. In Fig. 5.9(a,c), indications of a fringe structure of the pattern are also observed.

The maxima and minima on the third harmonic clearly indicate that the position of the aperture can affect the strength of the detected signal. Further, Fig. 5.8 shows the signal over the area of the detector to be a function of the environment of the tip -which can change, for example, by scanning a sample. The question arises to what degree the position of the aperture will affect the general appearance of obtained images.

To further explore this aspect, I simulated the imaging of a gold inclusion in a similar way as in Ch. 4. Instead of the integrated signal over the detector area, I use here the fields at single points of the detector. The demodulated signal for the second and third harmonics are presented in Fig. 5.10(a,b), for an inclusion at 1nm depth, 10nm

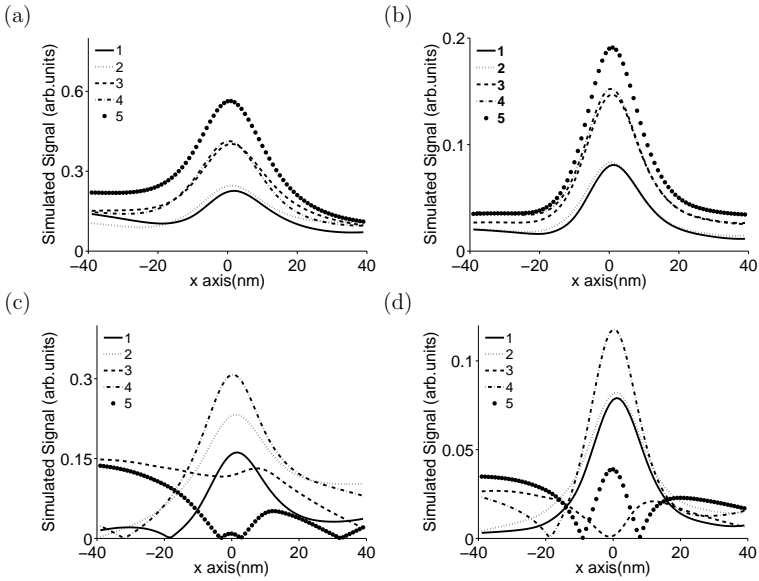


Figure 5.10: (a,b) Simulated amplitude detected at the lock-in when scanning a gold inclusion on a glass substrate for demodulation at the second (a) and third (b) harmonics, for an aperture situated at different points of the detector. 10nm oscillation amplitude and 1nm closest distance between tip and substrate have been chosen. The labels refer to Fig. 5.8(e-f). (c,d) is calculated with identical conditions than (a,b), but after setting the value of the optical phase to zero.

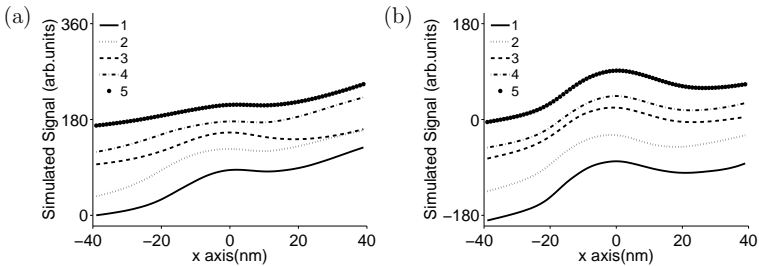


Figure 5.11: Simulated phase detected at the lock-in when scanning a gold inclusion on a glass substrate for demodulation at the second (a) and third (b) harmonics, for an aperture situated at different points of the detector. 10nm oscillation amplitude and 1nm closest distance between tip and substrate have been chosen. The indicated labels refer to Fig. 5.8(e-f). Each trace is shifted a different amount vertically for better visibility.

oscillation amplitude and a minimum distance to the substrate of 1nm. The different traces correspond to several points at the detector situated at $y' = 0$ and increasing z , as indicated in Fig. 5.8 (e,f). The position clearly influences the strength of the detected signal. Also, an effect beyond a simple scaling is found (Fig. 5.10(a,b)), as clearly apparent in the second harmonic. In particular, the ratio between the signal obtained for the tip directly over the inclusion and far from it can be maximized by adequately choosing the detector position. The qualitative behavior of the image is, however, mostly independent of the position of the aperture, which is promising for experimental reproducibility.

As the optical phase is included in the calculations, it is possible to obtain the phase that would be measured with a lock-in amplifier, and in particular its dependence on the aperture position. Notice, for example from combining the cosine and sine terms in Eq. (5.6) into an exponential, that there is a certain arbitrariness on phase sign, which depends on the exact experimental implementation. An example of the phase is shown in Fig. 5.11 for the second and third harmonic for the same positions of the aperture. A signature from the tip interaction with the gold inclusion is observed, and thus the phase also allows to obtain local information about the substrate. The change of phase due to the presence of the inclusion is, however, small.

To conclude, I study the effect of neglecting the phase on the imaging process. Fig. 5.10(c,d) shows simulated images obtained in the same way as Fig. 5.10(a,b), but with the optical phase set to zero. While some curves in Fig. 5.10(c,d) look qualitatively similar to those in Fig. 5.10(a,b), with a clear maximum when the tip is situated directly over the inclusion, others present a weaker maximum or not maximum at all. It illustrates the importance of including the phase for reliable simulation results.

5.3 Discussion and conclusion

In this chapter, I first compare interferometric and noninterferometric detection to illustrate that how the scattered fields are detected can influence the obtained images. While

in both cases near field information is achievable, the simulated images which assume interferometric detection show a more clear signature from a gold inclusion, a further advantage beyond the usually discussed enhancement of signal strength and capability to obtain phase information.

Secondly, I use Eq. (5.5) to study diverse aspects of the *aSNOM* interferometric imaging process. In particular, the detector signal results from different contributions from each area element and it is affected by the interplay of optical phase and amplitude.

For a better understanding of the consequences of the optical phase dependence on tip position, I chose a model that allows to arrive at a relatively simple analytical expression, Eq. (5.13), sufficient to describe fields of low spatial frequencies. It provides a key message also valid for more general interferometric conditions: both the optical phase and amplitude of the local fields affect simultaneously and in a nontrivial manner the amplitude and phase read at a lock-in amplifier. To disentangle the contributions from the optical phase and amplitude, a more sophisticated scheme has to be used. Fig. 5.10 directly illustrates for a scan over a patterned substrate the importance of including the optical phase to accurately simulate the amplitude read at the lock-in amplifier.

When Eq. (5.13) is applied to beam scans (Eq. (5.14)), it illustrates, together with Fig. 5.4, the possible dramatic changes in the nature of the detected signal: it changes from being mostly proportional to the local field amplitude to being sensitive to its first derivative merely by varying the tip oscillation amplitude. A method to cancel background components, at least those of approximately constant amplitude and linearly varying phase, has been suggested on the basis of similar considerations by Gucciardi et al. [148].

It is also necessary for a complete understanding of *aSNOM* to notice that the fields at the detector are not necessarily homogenous, with a different contribution to the total signal from each area element. As a simple example, it explains why a precise alignment of the interfering beams is crucial. Differences of the incidence angle or the wavefront

curvature radius between the interfering beams severely decrease the strength of the received signal.

I have further shown that, independently of the alignment, the fields scattered by the tip do not have to be homogeneous over the detector. Horizontal fringe patterns clearly appear on the simulations for both the optical amplitude and phase, and promising experimental indications have also been found. To obtain a good correspondence between both, a detailed knowledge of the experimental conditions is important. As a hypothesis, sharp and geometrically regular tips may be necessary to obtain a fringe visibility in the experiments as good as in Fig. 5.8. The influence of the experimentally used lens has also been suggested to spread the pattern [151]

Ideally, the contribution from each area element of the detector would be separately recorded and processed, thus obtaining different signal channels. The images obtained depend on the channel being considered, the influence going beyond the strength of the obtained signal. The changes on the overall shape for the examples presented in this chapter were not dramatic, mostly qualitative, but certainly not given by a simple uniform factor. Further studies are necessary to check whether this holds true for other tip sample geometries (and also other illumination and light collection schemes) or if more dramatic effects are possible. As an example, I have obtained a different spatial distribution of the signal over the detector when the tip is interacting with a gold homogenous sample, or with a small gold inclusion. The channel being considered is thus influencing the signal ratio between structures of the same material but different shape.

The multichannel scheme described is experimentally very challenging, but it is easy to select one channel of interest by using an aperture. This often implies a weaker intensity of the remaining radiation, but assuming the aperture is large enough for a good signal to noise ratio, this is not necessarily a critical concern. The extra degree of freedom obtained by changing the position of the iris could then compensate the decrease on signal level.

Further, due to the interferometric nature of the measurement, the decrease on the signal strength due to the aperture is in general smaller than if the phase in Eq. (5.5) were constant over all the detector. If different contributions partially cancel because of a $\sim 180^\circ$ phase difference, it is even possible to increase the signal level by reducing the effective detector area with an aperture of adequate size. Indeed, with my experimental set-up, a nonmonotonic dependence of the strength of the signal with the size of the aperture has often been observed. Here, the changes on the phase difference over the detector were probably predominantly introduced by difficult to avoid imperfections in the experimental conditions, such as different wavefront curvature of the beams. An additional contribution is to be expected from the spatial variation of the scattered beam's phase, as discussed in Sec. 5.2.3. In Fig. 5.7, the decrease on the achievable signal due to this source of phase variation was small, but may gain in significance for other geometries.

Lastly, the possibility to image using the lock-in amplifier phase was also considered. Comparing Fig. 5.10(a,b) and Fig. 5.11 suggests that the lock-in amplifier amplitude is more convenient to identify the presence of sub-surface structures, as the phase signature from the inclusion is relatively weak. Phase imaging was, however, useful for some experimental *aSNOM* studies [23, 152], and the capacity to obtain it is a further advantage of my simulations.

In this chapter I have shown that a complete modeling of the signal given by a detector, including phase modulation and the different contributions from different areas of the detector, is necessary to accurately model *aSNOM*, and offer new ways to optimize experiments.

Chapter 6

Experimental Set-up and procedures

In the previous chapters I have already presented several experimental results that illustrated the connection between the different theoretical scenarios considered and real measurements. Many of the characteristics of the used set-up have already been described [153]. A brief overview is given in this chapter, together with a more detailed description of an alignment procedure that I developed to reduce the time required for convenient near field discrimination. Last, I discuss the influence of excitation and detected polarization on the experiments, and show how a careful control can facilitate passive measurements. The measurements in Ch. 7 will make use of the techniques described here.

6.1 General description of the set-up

Fig. 6.1 shows a scheme of the experimental set up typically used in this thesis. It corresponds to a homodyne scheme that makes use of two consecutive measurements in phase quadrature. Fig. 5.3 was obtained with a heterodyne scheme [153, 154]. I have shown in Sec. 5.1.3 that both are equivalent under typical experimental conditions.

The laser radiation from a tunable Ti:Sa laser is transmitted by a fiber optic and

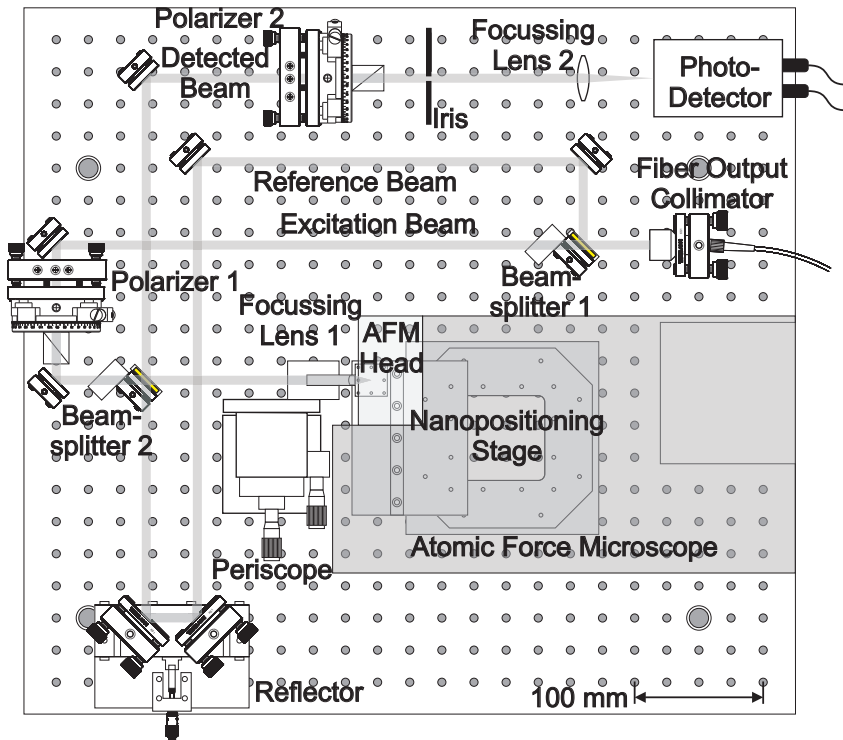


Figure 6.1: Schematic of the homodyne experimental setup used in this thesis

collimated at the output. The beam is split at the first beam-splitter, and two beams are obtained labeled excitation and reference beam. After going through a linear polarizer, the excitation beam is focused near the apex of the tip and the backscattered radiation is collected and collimated by the same lens used for the focusing. It is then mixed with the reference beam at a second beam splitter, the resulting interference beam being referred to as detected signal. After choosing the analyzed polarization at a second linear polarizer, an iris allows to select which area of the cross-section of the beam is actually used for the measurement. As the area of the photodetector is relatively small in our experiments, a final lens focuses the signal to ensure that all the remaining beam –for any position and size of the iris– is utilized. The electrical signal from the photodetector is fed to a dual phase lock-in amplifier that discriminates the signal at the $n - th$ harmonic of vibration of the tip.

One of the guiding principles when deciding the position of the different optical components was to have independent control over the excitation, reference and detected beam: the different paths are long enough to allow modifying the original beams. Here, I have made use of this freedom to control the polarization of the detected and excitation beams [155, 156]; more complex transformations are also possible. Beyond the applications described below, control of the polarization in *aSNOM* can be used, for example, for magnetic measurements [45].

The desired signal is a combination of two different measurements (Sec. 5.1.3), which differ by a $\sim 90^\circ$ phase change of the reference beam. The optical path is controlled by the mirrors labeled "reflector" in Fig. 6.1, which are mounted on a piezo stage controlled by the computer. To be able to determine which voltage must be applied to achieve the 90° change, a first calibration measurement is taken in which the voltage is continuously changed over a sufficiently large range. It can be seen from Eq. (5.4) (for $\Omega = 0$) that a periodic signal is obtained, from which the relationship between applied voltage and difference of optical phase can be extracted.

For the measurements, the distance between tip and sample has to be carefully

controlled. Here, a standard atomic force microscope (AFM) mechanism is used, in which the tip is vibrated perpendicularly to the sample (z direction) at a fixed frequency. By monitoring the position along z that is required to keep the oscillation amplitude constant, the topography is obtained together with the optical information.

aSNOM is a scanning technique, in which values have to be recorded for each pixel of an image, i.e., for each position of the nanopositioning stage. The latter is displaced, not the tip, to avoid altering the optical alignment between the tip and the focus of the excitation beam. As explained, the tip is moved along the z axis to follow the topography, but the displacement required is typically much smaller than the waist radius of the beam.

To speed up the measurement, a complete line is obtained for a given reflector position by continuously moving the nanopositioning stage while recording the lock-in signal periodically. Afterwards, the complete line is taken again with the shifted reflector position and each pair of values corresponding to the same location is mathematically combined as required. I usually take two images simultaneously (i.e. four values are measured for each location), the first in the forward direction and the second for the backward direction. I have verified that the influence of the scanning direction in the images discussed in this thesis is small and do not affect their interpretation. A mechanical artifact [133,134] sometimes present in *aSNOM* measurements is thus of little significance in this thesis.

6.2 Optical alignment

For *aSNOM*, it is desired to place the apex of the tip near the focus of the illumination, which increases the energy density at this crucial region of the tip and diminishes it elsewhere. Further, the backscattered fields from the apex will be then efficiently collected by the same lens as used for the focusing. Afterwards, the collected radiation is led to interfere with the reference beam, a process that also requires careful control. In this section I will describe the techniques used during my work to better handle these

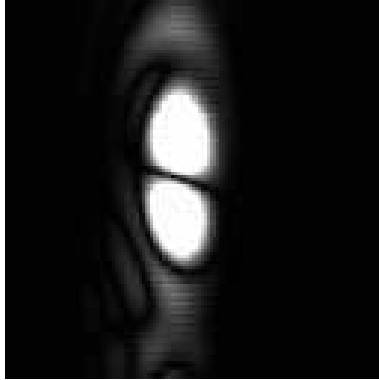


Figure 6.2: Example of a beam scan, for noninterferometric detection at the first harmonic and illumination polarized in the plane of incidence. The complete picture corresponds to a $20 \times 20 \mu\text{m}$ area.

experimental steps. They are usually necessary after each tip change, so that speed and reproducibility are important considerations. If the final measurement requires both polarizers to be oriented at mutually perpendicular directions (Sec. 6.4), the alignment is performed for a different orientation of the second polarizer. Otherwise the signal is greatly diminished and the alignment complicated.

6.2.1 Characterizing the focus volume

As mentioned, it is important to locate the position of the focus with respect to the tip, and ideally to characterize its field distribution. The method described here was found to be useful.

With the help of cameras to observe the general area under illumination, and the cantilever shadow, it is possible to obtain a first rough alignment by moving the relevant mirrors. Afterwards, successive scans of the beam [105,106] at different tip heights are obtained, and a 3-dimensional view of the scattered fields emerges. Knowledge about the local fields can be obtained by assuming that the scattered intensity is proportional to the square of the electric fields at the position of the tip apex, as suggested by the results in Sec. 2.1.2 at least for illumination polarized in the plane of incidence (plane

xz).

While an interferometric measurement is possible, it requires to have a correct alignment, something more easily done after the focus is found. Thus noninterferometric measurements are used, typically at the first harmonic. For sufficiently small oscillation amplitude, the first harmonic is approximately proportional to the first derivative of the detected signal with respect to the direction of oscillation. Notice that the signal of the detector for a noninterferometric scheme is a function of the (real valued) scattered intensity and the discussion in Sec. 5.2.2 does not apply.

For the assumed proportionality relationship between the square of the local fields and the scattered fields intensity, a horizontal map of the fields across the focus of a gaussian beam will show a zero at the center and two lobes at either side. Such pattern is indeed observed in Fig. 6.2, where a beam diameter of a few micrometers can be estimated. Fig. 5.4 and Fig. 6.2 serve to compare interferometric and noninterferometric schemes. The idealized interferometric measurement is proportional to the local fields amplitude or to its derivative, the latter for a particular oscillation amplitude. The idealized noninterferometric measurement is proportional to the derivatives of the *square* of the local fields. Thus, only for adequate oscillation amplitude is the interferometric measurement strongly sensitive to the derivative of the local fields and the corresponding image can be similar to those from noninterferometric schemes.

Experimentally, a strong signal is also obtained when the beam is focused at certain locations of the cantilever far from the the apex. This could be due, for example, to a strong scattering from corners. With the help of cameras and some knowledge of the tip and illumination geometry, such undesired maxima of signal can be recognized and avoided.

Once the fields have been mapped, it remains to decide where to place the tip. Although the estimated center of the focus looks as a promising first choice, I have found experimental indications of an improved near field discrimination when the tip is placed close but not exactly at this position— in my case, at the upper frontal region of

the focus volume. At this stage, the reason of this observation is not clear.

6.2.2 Interferometry

I discussed in Sec. 5.2.3 how, even for the interference between two ideal gaussian beams, imperfections in the alignment result in a phase difference which is no longer constant over a cross-sectional area of the resulting detected beam. To characterize the phase difference distribution, and improve the alignment if necessary, two techniques are routinely used in my measurements.

The fastest technique just involves projecting the beams onto a screen, as depending on the phase difference constructive or destructive interference ensues and an interference pattern is observed. It requires to be working with wavelengths that can be observed by the naked eye or an external camera. Temporarily attenuating the reference beam can help to obtain a better visibility of the interference patterns, but care must be taken not to affect the alignment conditions. It is also convenient to maintain the tip fixed or with small oscillation amplitude, as the fast signal modulation can blur the interference pattern. Similarly, this technique can be impractical for a heterodyne set-up, as the difference of frequency Ω between the two beams is equivalent to a shift phase too fast to observe visually, $2\pi\Omega$ rad/s with $\Omega = 80\text{MHz}$ being a typical value.

For a more accurate measurement of the spatial phase difference distribution, valid for heterodyne and homodyne schemes and any wavelength, the iris in Fig. 6.1 is used. With a small-sized aperture size, the iris is placed at different positions of the detected beam and the corresponding amplitude and phase are characterized with a lock-in amplifier, for example at the first harmonic of the vibration of the tip. An example of a typical spatial phase difference distribution was already shown in Fig. 5.6. The direction of propagation is close to identical for the two beams, as neither horizontal nor vertical fringes patterns are observed. The phase difference is however nonconstant, with an approximately radial distribution, which could originate in a different wavefront curvature of the two beams. Once a satisfactory phase distribution has been achieved, I typically

chose the position where it is nearly constant to place the iris aperture. For an adequate iris size the interference is mostly homogeneous over all the effective area.

6.3 Amplitude calibration

As discussed in previous chapters, the oscillation amplitude of the tip is crucial for *aSNOM* imaging; too small a value can result in a too weak obtained signal, but increasing it complicates the discrimination of the near field component.

Unfortunately, the oscillation amplitude reported by the commercial AFM I use is not calibrated, and seems to differ even between tips of the same type by as much as a factor of 2. I briefly propose here a scheme that can help to solve this problem. A similar idea has been recently studied by Gucciardi et al. [149].

As shown in Sec. 5.2.2, the signal obtained at the n th harmonic under weakly confined illumination conditions is proportional to the bessel function of order n , $J_n(\beta\mathcal{A})$. \mathcal{A} is the oscillation amplitude and β a constant corresponding to the change of the phase of the detected signal for a unit displacement of the tip along its oscillation direction. By slowly increasing the amplitude and monitoring the signal at the lock-in amplifier, the value of $\beta\mathcal{A}$ which corresponds to the first zero of the bessel function can be determined. Once β is known, a proportionality factor between \mathcal{A} and the amplitude given by the AFM software is easily obtained. Last, this factor is assumed to hold for other oscillation amplitudes, an assumption supported by the excellent fitting on Fig. 5.3.

β depends on the wavelength and the angle between the excitation and the direction of oscillation of the tip. The former is easily measured, so that if the latter, macroscopic parameter is assumed to be constant for tips of the same kind, β needs to be characterized only once. This can be done with a detailed knowledge of the geometry, or by some other technique. Here, a rough estimate of β was deemed sufficient.

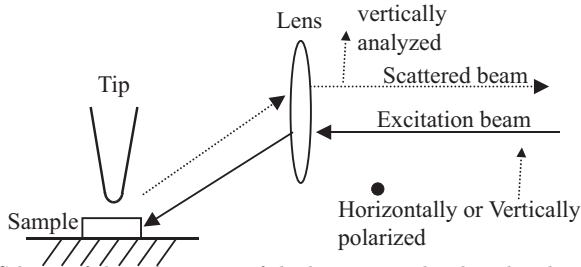


Figure 6.3: Scheme of the polarization of the beams considered in this thesis. The vertical polarization is usually analyzed. The excitation polarization is typically vertical for strong interaction between tip and substrate and horizontal for nonperturbative measurements

6.4 Controlling the polarization

As described in Sec. 6.1, I can choose the linear polarization for the excitation of the sample and for the detection. The vertical component is typically analyzed (Fig. 6.3), as for an elongated tip the near fields perpendicular to the substrate are expected to be the most relevant, and to be preferentially scattered with vertical polarization [105,147,155]. Results below and in the next chapter are in agreement with these expectations.

The focus here is thus on the polarization exciting the sample, and how it is possible to influence the strength of the interaction between tip and substrate and switch between predominantly passive and active configurations. The scheme in Fig. 6.3 illustrates the two possibilities considered.

In *aSNOM*, a strong interaction between the tip and the substrate is frequently desired, as it can maximize the scattered signal and can be very helpful, for example, to determine material contrast [60,121]. Vertically polarized excitation is then usually preferred. A simple dipole model explains why maximum near field signal is expected under such conditions (Ch. 3). Including the elongated form of frequent AFM tips further strengthen the advantages of vertical over horizontal polarization [93,102]. As an example, for Fig. 3.7 strong interaction was desired.

A very different situation arises when a non-perturbative measurement is desired. In this case, strong near fields are already present in the sample. A sharp tip is used

as a scattering center, which converts the near field into far field radiation to be detected by external optics. Ideally, the tip does not alter the field distribution that was originally present. To reduce the interaction, the excitation beam polarization is chosen as horizontal [157], i.e., perpendicular to the analyzed polarization. I will refer to this configuration as cross-polarization scheme. Notice that horizontal polarized excitation excites a different response in the sample [142, 147] than vertical polarization. I discuss in Ch. 7 that, when combined with oblique illumination, it can be used to directly observe resonances of higher order than the dipolar.

A further and very significant advantage of the second polarization scheme is its capability to improve the discrimination of the near field signal. Much of the radiation scattered by the tip-substrate system does not contain information about the localized near fields. Fortunately, it is also predominantly polarized in the direction of the excitation, and thus is suppressed to a large extent by the vertically polarized analyzer.

I illustrate next some of the advantages of the cross-polarization scheme. I discuss measures on structures consisting of two closely situated gold disks, in which plasmonic resonances can be excited. They will be described in detail in the next chapter. At this point, it is sufficient to accept Fig. 6.4(a) and Fig. 6.5(a) as examples of good measurements, which serve as comparison standard. Both images are not identical because of differences in the structures, the wavelength and the tip apex (Ch. 7).

Fig. 6.4(a) illustrates a measurement at the second harmonic using a silicon tip covered by its native oxide. The height represents the topography, and the texture the detected signal amplitude. The near fields are concentrated at the edges of the structure and exhibit mirror symmetry. The negligible signal when the tip is situated far from the structures indicates a good background suppression, facilitated by both the cross polarization and the high harmonic demodulation. It is nonetheless interesting that, with the described scheme and under favorable conditions, it is possible to get near field information even at the first harmonic, as illustrated in Fig. 6.4(b). The background has increased but localized near field contributions are still clearly visible.

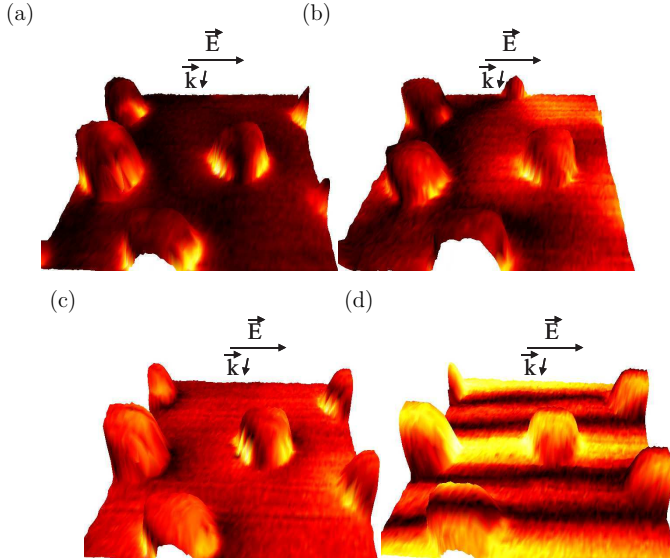


Figure 6.4: Measurements of plasmonic structures, consisting of two stacked gold disks separated by a 40nm spacer, the larger disk of $\sim 170\text{nm}$ diameter, which will be described in more detail in the next chapter. The indicated \vec{E} and \vec{k} correspond to the approximate polarization of the excitation and projection of the propagation vector into the sample, respectively. The angle between the incident illumination and the substrate normal is $\sim 65 - 70^\circ$. The measurements are obtained for $\lambda \sim 865\text{nm}$, some tens of nanometers towards the red from the low energy resonance maximum of this particular sample. The height information represents the topography and the texture the detected optical amplitude. In (a,b) the vertical polarization is analyzed, in (d) the horizontal, and (c) represents an intermediate case in which the polarizer is shifted $\sim 30^\circ$ with respect to the vertical position. (a,c,d) are measured at the second harmonic, and (b) at the first. Silicon tips covered by the native oxide layer were used. An area of $1\mu\text{m} \times 1\mu\text{m}$ is plotted.

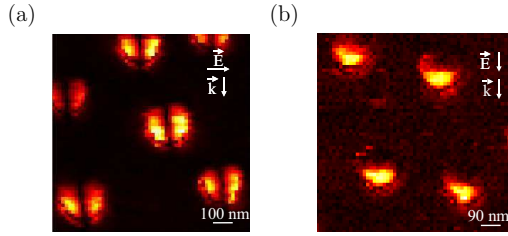


Figure 6.5: Measurements of the optical amplitude detected at the third harmonic for plasmonic structures formed by two gold disks separated by a 20nm spacer. The larger disk can be of ~ 170 or ~ 190 nm diameter. They will be described in more detail in the next chapter. The same sample and the same etched Silicon tip was used for both images. The indicated \vec{E} and \vec{k} corresponds to the approximate projection of the electric field and the propagation vector into the sample, respectively. The angle between the incident illumination and the substrate normal is $\sim 65 - 70^\circ$. $\lambda \sim 820$ nm was used, approximately at the position between the two observed dipolar resonances. (a) corresponds to horizontally and (b) to vertically polarized excitation.

To study the influence of the analyzer, I change its orientation for the second harmonic measurements. From the previous discussion, the horizontal polarization of the scattered fields is expected to contain weaker near field signal, and much enhanced background. Indeed, a $\sim 90^\circ$ shift of the analyzer polarization results in a completely degraded signal, in which no clear remanent of near field information is observed (Fig. 6.4(d)). If shifted $\sim 30^\circ$ instead of $\sim 90^\circ$, the near field component is just moderately influenced, but the background increases considerably, and the quality of the measurement deteriorates, as illustrated in Fig. 6.4(c). Here, the near field signature was strong and can still be distinguished. Besides the orientation of the polarizers, I have observed that other aspects, such as the position of the iris or the location of the tip with respect to the focus [158], can influence the achieved background suppression.

I study next the capabilities of the cross-polarization scheme to facilitate nonperturbative measurements (Fig. 6.5). A bare silicon tip is chosen, as I have shown in Chs. 3,4 that for vertical polarization they can interact strongly with the substrate. The excitation beam polarization is changed between vertical (b) and horizontal (a) excitation. Fig. 6.5(b) is of completely different nature than Fig. 6.5(a), the results presented on the following chapter or images from other groups for similar systems [50,157]. To include

a strong tip-substrate interaction is likely needed to explain the obtained pattern. On the other hand, the image taken under horizontal polarization (Fig. 6.5(a)) presents the expected mirror symmetry and are in general close to the expectations for nonperturbative measurements for a broad tip (Sec. 7.3). Bare silicon tips were used here but they are covered by the native oxide, which is transparent and of low dielectric constant, in my typical measurements, further strengthening my confidence on the non-perturbative nature of the measurements.

6.5 Tip choice

In this section I briefly comment on the tips used, and in particular on why different tip materials can be convenient depending on the specifics of a measurement. I have used commercial Silicon advanTECTM AFM tips, whose tip orientation facilitates direct illumination of the apex by the focused excitation beam.

As discussed in Ch. 1, when a strong interaction between the tip and the substrate is desired, both metallic and silicon tips are possible choices. Silicon tips are promising for ultimate lateral resolution. To etch the native oxide layer and temporarily passivate the surface, HF is used.

Tips with an adequate metallic surface do not oxidize and can be used longer, but the fabrication of sharp tips is challenging (Sec. 1.1.3). Although I concentrate on Silicon tips in this thesis, I verified the possibility to obtain near field signal using tips fabricated by metallic coating of commercial silicon tips.

For a passive probe, the tips can be used directly without any processing steps. The low and real dielectric constant of the native oxide reduces the tip-sample interaction. The tips can be very sharp, offering the possibility of very high resolution. The downside of sharp tips with small dielectric constant is the weak near field signature expected. Higher harmonic demodulation and the cross polarization scheme are used to discriminate it.

6.6 Discussion and conclusions

In this chapter I have described in more detail the experimental set-up used during my thesis work. I have focused on ways to facilitate the optical alignment and the discrimination of a near field signal. Comparing the obtained alignment for different tips can also help to improve reproducibility.

To place the tip, the beam is scanned without a sample. The discussion of Secs. 2.1.2 suggests that for vertical polarization the intensity of the scattered fields is proportional to the square of the fields at the apex of the tip. The question arises if this simple relationship is maintained for real tips, in particular when they present irregularities in their shape. At least for some area around the apex, the measurements do compare well with the expected images, which points to the validity of the idealized model.

Assuming the simple proportionality to hold, I have also described that the optimal position for near field discrimination is not necessarily at the estimated position of the center of the focus, which requires further work to understand but is potentially relevant for optimizing aSNOM measurements. From a purely pragmatic point of view, and independently of the above, a tip position must be found where the near field signature is strong enough to be discriminated. It is useful to place each new tip close to a position already proved convenient for a reference tip, which is helped by the information gained from the beam scans. Such scans are thus helpful to discriminate the near fields.

After choosing the position of the tip, the interferometry between the excitation and reference beam is characterized. Simply projecting the detected beam into a screen is often enough for a qualitative knowledge on how the both used beams interfere. If more quantitative information is desired, or if the experimental set-up uses a heterodyne scheme or wavelengths not easily imaged, systematically blocking the beam except at selected areas is useful.

A slowly varying phase difference over the area of the photodetector is desired. It helps to obtain a strong enough signal (Sec. 5.2.3) even at the higher harmonics and low oscillation amplitudes typically needed for good background suppression (Sec. 4.2.4).

In my experimental set-up, the effect of remaining alignment imperfections, due to, for example, differences on the wavefront curvature, can still be clearly seen in the spatial distribution of the phase distribution. Notice also that, even for perfect alignment, the phase difference is not necessarily constant over the detector, due to the spatial phase distribution of the fields scattered by the tip-sample system (Sec. 5.2.3). For spatially heterogeneous phase difference, an area of almost constant value can still be selected by an aperture of adequate size. The phase difference must vary slowly enough for the corresponding aperture size not to block most of the signal scattered by the tip-substrate. Requiring the variation to be too slow, on the other side, increases the experimental difficulty, especially for a nonperfectly achromatic set-up and frequent wavelength changes. An equilibrium must be found.

Once the interferometry is optimized, the knowledge of the exact experimental conditions can be further increased by the proposed scheme to measure the oscillation amplitude (Sec. 6.3). It requires to know the value of β , a parameter that depends on the macroscopic geometry of the cantilever and illumination and is assumed to vary little between tips of the same kind. For a good knowledge of β , the described scheme promises a very good achievable precision. Also, it is possible to compare the oscillation amplitude for two different tips as far as β remains approximately constant, even if its exact value is not known.

One advantage of the chosen experimental configuration is the possibility to control the polarization of the beams, which allows to choose between two conceptually different schemes. The first uses vertical polarization for excitation and analysis and corresponds to the typical aSNOM case, in which a strong interaction between tip and substrate is desired. I have discussed in this thesis how bare silicon tips are a promising alternative to the metal tips often considered.

The second scheme aims to improve background suppression and to reduce the interaction between the tip and substrate for nonperturbation measurements. It utilizes horizontal excitation and vertical detection, and it allows for sharp and easy to use

commercial silicon tips, in this case covered by the native oxide layer. The clear images obtained from this and next chapter illustrate its promising capabilities for passive measurements. For tips that scatter efficiently the near fields, an efficiency attributed to a relatively blunt apex, it is possible to obtain a near field signature even in the first harmonic. For the second harmonic, a useful signal stronger than the background has been consistently obtained, as will be illustrated in the next chapter.

To verify that this method is indeed nonperturbative, the obtained images can be compared with simulations (Ch. 7) and a good agreement is found. As a further check, I measure the structures for bare tip using both horizontally and vertically polarized excitation. I have already shown how, for the latter, a strong interaction between the tip and the substrate is possible. Indeed, some of the measurements performed under vertical excitation seem altered by the interaction, to a degree which depends on the particular conditions. Images obtained with the cross polarization scheme are, on the other hand, consistently similar to the expectations for a passive method. That this is the case even for bare silicon tips, while most measurements are done for tips covered by silicon oxide, of low dielectric constant, further strengthens the confidence on the nonperturbative nature of the measurements.

I have regularly obtained a clear near field signal for the plasmonic structures studied in the next chapter, where the time interval between changing to a new tip and obtaining an adequate near field signature was typically not more than 3-4 hours. The main factor still reducing the yield of usable tips appeared to be not optical but fast tip deformation of the tips due to poor mechanical properties, which could be helped by a better AFM system. The described cross-polarization scheme is thus very promising for measuring the near field distribution from samples systems requiring good background suppression and passive probe.

Chapter 7

Near field measurements beyond dipolar resonances

Plasmons are the quanta of coupled collective charge density and electromagnetic field oscillations. In particular, plasmons at small metallic structures exhibit strong coupling to external radiation for particular resonant frequencies [159]. Such resonances are associated with strong and localized near fields in the vicinity of the structures, but measurements are usually performed in the far field.

Collaborators in Chalmers University fabricate a range of resonant nanostructures that can be used to design optical metamaterials and biosensors. Metamaterials are novel, artificial materials that, by using structures of subwavelength dimensions, can achieve permittivity and permeability responses not found in bulk matter [160]. Label-free optical biosensors based on plasmonic structures make use of the high sensitivity of the resonances to the dielectric constant of the surrounding medium [161–167]. By functionalizing the particle chemically, the sensors can be made sensitive to specific molecular species. The optical response of these plasmonic structures is typically characterized experimentally in the far field. Their near field can be simulated, often assuming significant simplifications. To complement these techniques, I measure directly their near field distribution using *aSNOM*. I characterize resonant structures of different size and shape, for different wavelengths.

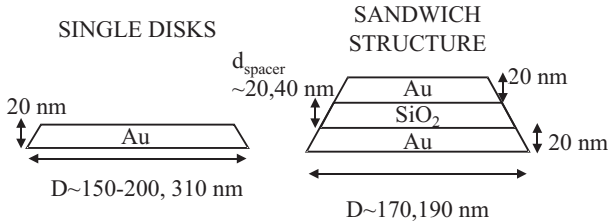


Figure 7.1: Side view of the plasmonic structures considered in this chapters. They are approximately rotationally symmetric

7.1 The samples: description of previous work

A cross section of the samples studied is shown in Fig. 7.1. The samples are approximately rotationally symmetric. Two kinds of samples are used, a single gold disk and a nanosandwich structure consisting of two gold disks of different lateral diameter, separated by a silica spacer of variable thickness d_{spacer} . All the gold disks are approximately 20nm high. Each nanosandwich structures can be seen as two dipoles coupled by the short range near field interaction to form an hybridized system, the strength of the hybridization depending on d_{spacer} . Dipole-dipole interaction exists up to large distances, but is of less interest here. Different wavelengths and different diameters of the structures have been considered. The diameter at the base will be referred to as \mathcal{D} .

The fabrication, far field characterization and the simulations in this chapter have been done by our collaborators, and only a brief overview will be presented in this thesis. For a more detailed description, [168–170] can be consulted.

The fabrication utilizes a hole-mask lithography method, where the mask is defined by the self-organization of electrostatically charged polystyrene spheres on a substrate. After selective etching and materials evaporation, arrays with typical nearest neighbor distance of around twice the diameter of the nanospheres are obtained. Due to the large inter-particle distance, the interaction between the structures is assumed to be a minor correction. Spheres of different radius can be simultaneously used, which leads to arrays with mixed sized and is useful for their *aSNOM* characterization.

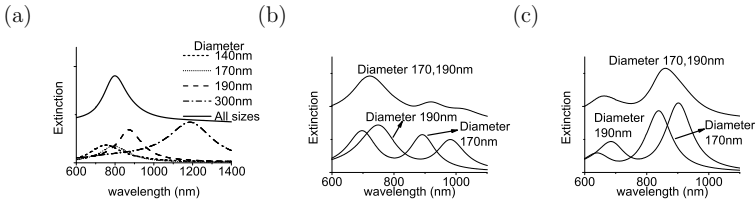


Figure 7.2: (a) Extinction spectra for single disks of $D \sim 150, 180, 200, 310$ nm, measured for samples containing one size only and a mixtures of the different sizes. Larger disks correspond to spectra shifted towards the red. (b,c) Extinction spectra for nanosandwich structures of $D \sim 170, 190$ nm and $d_{\text{spacer}} \sim 20$ (b), or 40 nm (c); samples that contain just one diameter, of both of them together were characterized. Some of the spectra in the images are vertically shifted for visibility

7.1.1 Far field characterization

The resonances are characterized in the far field by measuring the extinction spectrum (Varian Cary 500). I show in Fig. 7.2 example of resonances for single disks and nanosandwich structures of the different geometries considered. This resonances should be taken as a guide, as even nominally identical samples can show some variability in the spectra measured. I also show the resonance measured on the samples used in Figs. 7.4,7.5(a,b),7.6, which contain structures of several diameters. The spectra have been measured if not otherwise stated for normal incidence. I use oblique incidence in the near field measurements, but as discussed in Sec. 7.3, the distinction is expected to be relevant only for the results in Sec. 7.2.2.

The resonances depend strongly on the shape and on the size of the structures. Two resonances are obtained for the nanosandwich structures, instead of one as for simple disks. Near field measurements of the nanosandwich structures will concentrate on the low energy resonance, i.e., corresponding to the larger wavelength.

7.1.2 Near field calculations

The simulations use the dispersive finite-differences time-domain technique, adapted to obtain both the near and the far fields. Planar wave excitation with incidence normal to the substrate is considered; the electric field is parallel to the substrate, as for the

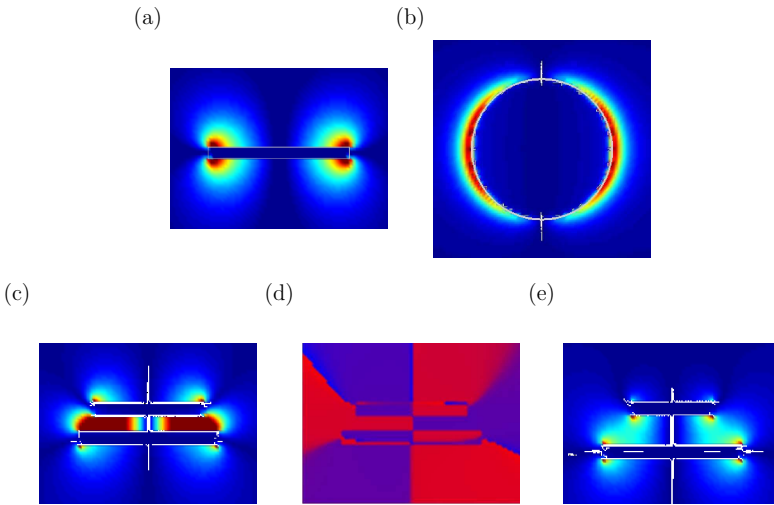


Figure 7.3: Simulated values of the electric field component perpendicular to the substrate for resonant (a,b) single disks of $\mathcal{D} = 192\text{nm}$ and (c,d,e) nanosandwich structures of $\mathcal{D} = 192\text{nm}$ and (c) $d_{\text{spacer}} \sim 20\text{nm}$ or (e) $d_{\text{spacer}} \sim 40\text{nm}$. The fields for the nanosandwich structures are calculated for the low energy resonance. Both optical amplitude (a,b,c,e) and phase (d) are considered. The phase is plotted between -180 and 180 degrees, and different amplitude scales are used for (a,b,c,d). (b) is plotted for a plane parallel to the disk, passing through it; the rest correspond for a cut at the center, parallel to the direction of the electric field and to the normal of the sample. The color scale is identical for (c,e), but differs otherwise. Normal incidence was used

aSNOM measurements. To ease the numerical complexity, no substrate is present and the nanosandwich structures are considered to be separated by vacuum. Although these simplifications will affect the value of the resonance wavelength, comparing the measured and calculated far field spectrum serves to approximately correct this effect. The considered model is expected to adequately describe the main properties of the near fields. Only the component of the fields perpendicular to the substrate is plotted, as *aSNOM* is expected to be mostly sensitive to it.

I plot in Fig. 7.3 the expected near field amplitude distribution for the single disks nanosandwich structures. Mirror symmetry is obtained with respect to a plane perpendicular to the excitation electric fields, as is most clearly seen in Fig. 7.3(b). For the dipolar resonance in the single disks, the near fields are clearly concentrated around the edges [157].

For the nanosandwich structures, two regions of strong near fields can be obtained at the top interface of the structure, one at each side of the axis of symmetry. Even stronger near fields are found at the edges (Fig. 7.3(c-e)). Fields at the top and at the edge present a clearly differentiated phase. The dependence of the fields at the edge with d_{spacer} helps to understand the hybridization between closely situated resonant particles [168, 169].

For the two disks situated at very short distance, the interaction mediated by the near fields is strong and it is not adequate to talk about two more or less independent disks, but they have to be considered together as a single hybridized system with two resonances. The thicker the spacer, the smaller the near field interaction, the weaker the hybridization and the more appropriate to discuss the gold disks as independent structures each of which with a different resonant wavelength (although a weaker, dipole-dipole coupling will remain). For $d_{spacer} \sim 20\text{nm}$, the maximum of the near field component perpendicular to the substrate is found in the area of the edges between the disks, and it is not possible to separate the contribution from each disk. For the less strongly hybridized nanosandwiches structures with $d_{spacer} \sim 40\text{nm}$, the corresponding

signal at the edges present more structure, with weaker signal at the center.

7.2 Near field characterization

The capability to directly probe near fields and the high achievable lateral resolution make *aSNOM* a very promising technique to study plasmonic structures. Two difficulties must be, however, overcome: the tip must not perturb the fields present in the sample, and the near field information must be correctly discriminated from the background. Hillenbrand et al. [50] used a carbon nanotube as a passive tip and were able to measure phase and amplitude of the dipolar resonance for a particular disk structure and wavelength. Anderson et al. [157] have also observed the amplitude signal from nanorods and nanodisks dipolar resonances by using two photon processes.

I am interested in going beyond dipoles towards higher order resonance patterns, an objective which is achieved by using the cross-polarization scheme described in Ch. 6. Both phase and amplitude are considered.

7.2.1 Dipole resonances

The most elementary resonance that can be excited in a small subwavelength particle is the dipolar. To image it in the near field, I consider singles disks of diameter between ~ 150 and ~ 200 nm. Some examples of $\mathcal{D} \sim 310$ nm are also present and will be discussed in Sec. 7.2.2. The near field signal for a particle with diameter around 180nm is shown in Fig. 7.4(a,b), as measured at the second harmonic for $\lambda \sim 800$ nm. The height information in the picture corresponds to the topography simultaneously obtained with the AFM and the optical information is encoded in the texture, for both amplitude (a) and phase (b). As expected (Fig. 7.3(a,b)), a dipolar like pattern is observed, with strongest signal at the edges and the two lobes clearly out of phase. Far away from the particles, the obtained signal amplitude is much reduced, which shows the good background suppression attainable by the combination of demodulation at higher harmonics and the cross polarization scheme described in the previous chapter.

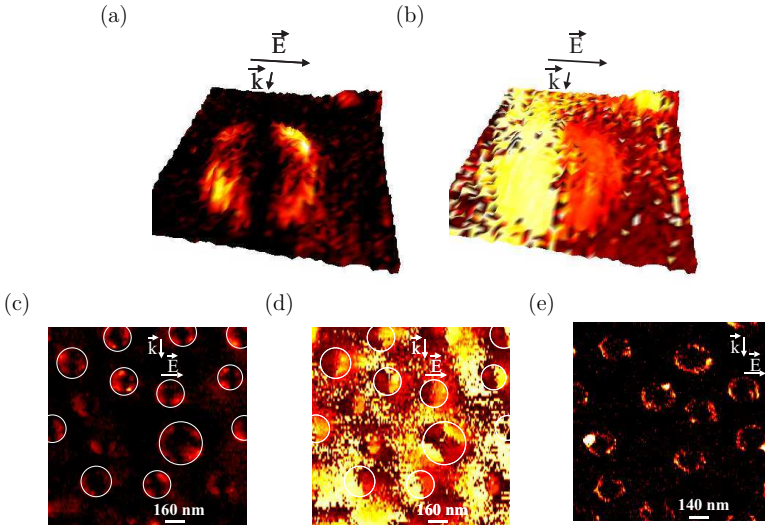


Figure 7.4: (a,b) Single disks measurement for a structure with $\sim 180\text{nm}$ estimated diameter. The height information corresponds to the topography and the texture to the obtained (a) amplitude or (b) phase for $\lambda \sim 800\text{nm}$. The area considered is $400 \times 400\text{nm}$ in both images. (c,d) correspond to the amplitude (c) and phase (d) for the same sample, but showing single disks of different size ($150 \lesssim \mathcal{D} \lesssim 200\text{nm}$ or $\mathcal{D} \sim 310\text{nm}$) for $\lambda \sim 800\text{nm}$. Circles are introduced as a visual guide for the approximate position of the disk. (e) amplitude measured for the same sample and $\lambda \sim 880\text{nm}$. (a,b,c,d) were obtained at the second harmonic, and (e) at the third. The phase have been plotted between -180 and 180 degrees. The indicated \vec{E} and \vec{k} correspond to the approximate polarization of the excitation and projection of the propagation vector into the sample, respectively. The angle between the incident illumination and the substrate normal is $\sim 65 - 70^\circ$.

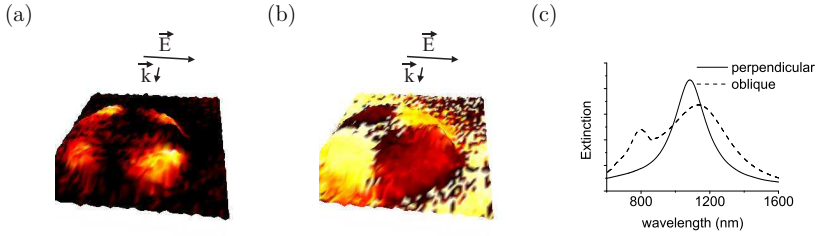


Figure 7.5: (a,b) Single disks measurements at the second harmonic for $\mathcal{D} \sim 310\text{nm}$ and $\lambda \sim 800\text{nm}$. The height information corresponds to the topography and the texture to the obtained amplitude (a) or phase (b). The phase is plotted between -180 and 180 degrees. The indicated \vec{E} and \vec{k} correspond to the approximate polarization of the excitation and projection of the propagation vector into the sample, respectively. The angle between the incident illumination and the substrate normal is $\sim 65 - 70^\circ$. The area considered is $500 \times 500\text{nm}$. (c) extinction spectrum for perpendicular and oblique incidence, in the latter case for an angle of incidence of 70 degrees with respect to the substrate normal. The spectrum is not exactly the same as in Fig. 7.2(a), as the results in (c) correspond to a slightly different sample.

To illustrate the reproducibility of the results, Fig. 7.4(c,d) shows a representative example of the resonances observed over several single disk structures, for similar conditions as in Fig. 7.4(a,b). As a guide for the phase image, circles indicating the position of several of the structures are also shown. A dipolar-like pattern is indeed observed in most of the structures. The phase difference between two lobes depends on the particular structure, but is comparable to the 180° expected for an ideal dipole.

A further example of the field amplitude distribution is shown in Fig. 7.4(e), in this case for a different wavelength $\lambda \sim 880\text{nm}$. The near field signature is less clear in previous images, likely because of a significantly sharper tip, but it serves to emphasize the high lateral resolution and the concentration of the near fields at a small volume near the edge of the structures. Besides the general resonance pattern, some points of particularly strong signal are observed, possibly local hot spots [72, 171] due to structure rugosity.

7.2.2 Quadrupole resonances

Even for structures as morphologically simple and symmetrical as the single disks, resonances of higher order than dipolar are possible. The extinction spectrum in Fig. 7.2(a), however, shows a single resonance, identified as dipolar in the simulations and in Sec. 7.2.1. At the wavelength range of my measurements, the far field response for $\mathcal{D} \sim 310\text{nm}$ is much weaker than for particles with diameter between $\sim 150 - 200\text{nm}$.

The behavior of the near fields is quite interesting. First, the strength of the measured near field signal is similar for all the sizes. Further, a closer look into the near fields of the larger disks reveal resonance patterns more complex than dipolar. Fig. 7.5(a,b), closely resemble a quadruple resonance, with four distinct areas of phase and amplitude. The main difference with a perfect mathematical quadruple is a significantly smaller phase jump than 180 degrees between some of the neighboring areas. The experimental measurement conditions are very similar to those used in Fig. 7.4(a,b), facilitating a direct comparison with the dipolar resonance observed there. The reasons for the difference between the near and far field measurements are discussed in Sec. 7.3

7.2.3 Coupled dipoles resonances

In the case of the nanosandwich structures, formed by two closely situated gold disks, the electromagnetic response of both disks is coupled, the strength of the coupling depending on the thickness of the spacer, d_{spacer} . A typical *aSNOM* phase and amplitude image of such coupled structures is shown in Fig. 7.6(a,b), for spacer thickness $d_{\text{spacer}} \sim 20\text{nm}$ and $\mathcal{D} \sim 170, \sim 190\text{nm}$. The wavelength chosen ($\lambda \sim 915\text{nm}$) is expected to excite the low energy resonance at least for the smaller particles (Fig. (7.2(b))). The main difference with the single disk images is the presence of four clearly differentiated areas where the near field is strong, each characterized by distinctive phase distribution. As before, two areas are situated at each side of the edge. The other two are situated at the top surface. The difference of phase between adjacent areas depends on the particle being considered but it is typically in the order of 180 degrees. The measurements closely correspond to

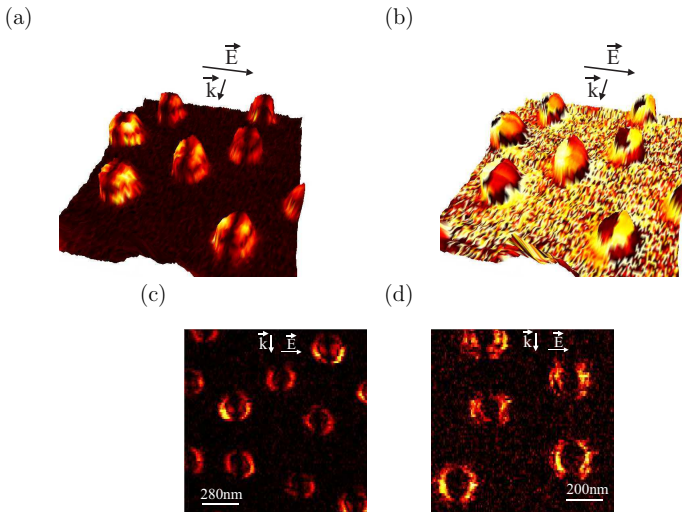


Figure 7.6: (a,b) Signal obtained for the nanosandwich structures, for $d_{\text{spacer}} \sim 20\text{nm}$ and $\mathcal{D} \sim 170, 190\text{nm}$, measured at the third harmonic and for $\lambda \sim 915\text{nm}$. The height information corresponds to the topography and the texture to the obtained amplitude (a) or phase (b). The phase is plotted between -180 and 180 degrees. The measured area is $1400 \times 1400\text{nm}$. (c,d) Amplitude measured at the third harmonic for $\lambda \sim 915\text{nm}$ for (c) $d_{\text{spacer}} \sim 20\text{nm}$ and (d) $d_{\text{spacer}} \sim 40\text{nm}$. Structures of $\mathcal{D} \sim 170\text{nm}$ and 190nm were fabricated in all samples. The indicated \vec{E} and \vec{k} correspond to the approximate polarization of the excitation and projection of the propagation vector into the sample, respectively. The angle between the incident illumination and the substrate normal is $\sim 65 - 70^\circ$.

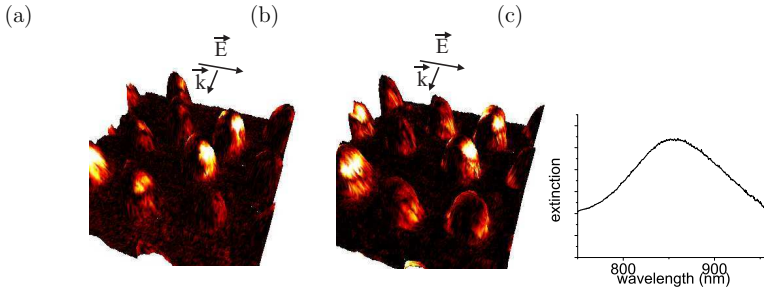


Figure 7.7: (a,b) Measured signal at the third harmonic, for structures with $d_{spacer} \sim 40$ nm and $\mathcal{D} \sim 170, 190$ nm, measured at $\lambda \sim 775$ (a) and ~ 865 nm (b). The height information corresponds to the topography and the texture to the obtained amplitude. The same area of the sample was measured in both images. The indicated \vec{E} and \vec{k} correspond to the approximate polarization of the excitation and projection of the propagation vector into the sample, respectively. The angle between the incident illumination and the substrate normal is $\sim 65 - 70^\circ$. The plotted area is 1400×1400 nm. (c) The relevant region of the extinction spectrum for this sample. It differs from Fig. 7.2 because a different sample was used.

the theoretical expectation from Fig. 7.3(c,d), both for the amplitude and the phase.

Further, I find indications of the influence of the hybridization strength in the near field distribution. Fig. 7.6(c,d) corresponds to the measured amplitude for $d_{spacer} \sim 20$ and 40 nm structures, respectively, in both cases for $\mathcal{D} \sim 170$ and 190 nm. Neither the tip nor the alignment were changed between images, to facilitate comparison. I chose again $\lambda \sim 915$ nm to excite the resonances of at least some of the particles characterized by $d_{spacer} \sim 20$ nm and by $d_{spacer} \sim 40$ nm, as can be seen from Fig. 7.2(b,c)

Focusing on the near fields at the edges, only one broad area of strong near field at each side is found for $d_{spacer} \sim 20$ nm (Fig. 7.6(c)), but a double maxima pattern is obtained for $d_{spacer} \sim 40$ nm (Fig. 7.6(d)). Notice that a second area of strong fields is obtained at the top of some of the structures with $d_{spacer} \sim 20$ nm, but the signal strength in this region depends on many experimental parameters and can be challenging to interpret (Sec. 7.3). The observed behavior at the edges closely relates to the simulation expectations from Sec. 7.1.2, but the agreement is not always as good as in Fig. 7.6(a), as will be discussed in Sec. 7.3.

In the near field distribution, I have also noticed that particles with $\mathcal{D} \sim 190$ nm often

result in stronger signature from the top of the structures than those with $\mathcal{D} \sim 170\text{nm}$. Such behavior is present in measurements taken using wavelengths ranging from ~ 775 to $\sim 915\text{nm}$, without clear correlation with the measured spectra. As an example, Fig. 7.7 shows a measurement of a fixed area at ~ 775 and $\sim 865\text{nm}$, for nanosandwich structures with $d_{\text{spacer}} \sim 40\text{nm}$ and the two discussed diameter sizes. Fig. 7.7 shows the measured far field extinction spectrum for such a sample, in the region of interest.

7.3 Discussion and conclusions

In this chapter, I have shown experimental images of the near field distribution for plasmonic structures excited close to resonance. Single disks are considered for studying dipolar and higher order resonances, and nanosandwich structures for discussing strong coupling between closely situated metallic particles. A broad agreement is often found between simulation and experimental results.

As expected from the far field measurements, a clear dipole-like near field pattern is typically observed for single disks with diameter between $150 - 200\text{nm}$, with two symmetric areas of distinctive amplitude and phase. Both areas present a phase shift comparable with the ideal 180 degrees, and the stronger intensity of the near fields near the edges also correspond with the expectations.

A more complex near field distribution is measured for the nanosandwich geometry, a structure consisting of two closely situated gold disks. The two disks interact strongly via the near fields, and a hybrid plasmonic system which can be described as coupled dipoles ensues. Interaction between metallic structures have been discussed as an interesting alternative to obtain negative permeability at optical wavelengths [172]. For $d_{\text{spacer}} \sim 20\text{nm}$, four clearly differentiated areas can be distinguished, two at the edges and two at the top of the structures. The large change of phase observed between adjacent areas (in the order of 180 degrees) is in good correspondence with the simulations. By comparing $d_{\text{spacer}} \sim 20\text{nm}$ and $d_{\text{spacer}} \sim 40\text{nm}$, indications have also been found of the dependence of the field distribution on the strength of the interaction between the two

closely situated gold disks.

I have also observed near field patterns more complex than simply dipolar for the larger single disks structures, with the phase and amplitude sometimes resembling a quadrupole. Notice that the quadrupolar four field symmetry observed in Fig. 7.5 is forbidden in rotationally symmetric structures for normal illumination and also for oblique illumination with polarization in the plane of incidence. It is possible in my experiments only because oblique incidence and polarization parallel to the substrate are simultaneously used. The fourfold symmetry is defined by the electric field orientation and the projection of the propagation direction of the beam on the substrate .

To complement this discussion, it is useful to perform new extinction measurements for single disks with $\mathcal{D} \sim 310\text{nm}$, this time with angle of incidence similar to the used in the *aSNOM* configuration. A clear second peak appears, at a wavelength close to the range selected for the *aSNOM* measurements, as shown in Fig. 7.5(c). The additional peak probably originates from the quadrupolar resonance and is thus consistent with the observed near field distribution.

After realizing the importance of oblique incidence for the large single disks, several new samples containing small single disks and nanosandwich structures of different sizes were fabricated to observe the influence on these structures. In general, a small peak and some broadening of the resonances is observed, and indications of the quadrupled resonance are also found for some of the single disks. The changes are nonetheless small for the measured samples and not expected to affect the obtained conclusions. In particular, single disks of $\mathcal{D} \sim 150, 180, 200\text{nm}$, and nanosandwich structures with $\mathcal{D} \sim 170, \sim 190\text{nm}$ and $d_{\text{spacer}} \sim 20, 40\text{nm}$ were characterized for oblique and normal incidence, concentrating on the low energy resonance for the nanosandwich structures, and a shift around 10nm was obtained.

The reproducibility of many of the observed features is good, for scans over a large area and also after a change of tip or of other experimental conditions, but additional work is still required in some cases. The most clear influence of the exact measuring

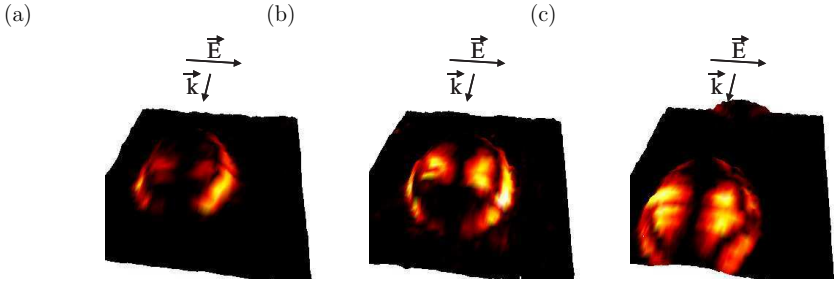


Figure 7.8: Examples of the detected signal at the third harmonics for structures of $\mathcal{D} \sim 170\text{nm}$ and $d_{\text{spacer}} \sim 20\text{nm}$, showing how the field distribution evolves from earlier (a) to latter (c) in the day. The height information corresponds to the topography and the texture to the obtained amplitude. The indicated \vec{E} and \vec{k} correspond to the approximate polarization of the excitation and projection of the propagation vector into the sample, respectively. The angle between the incident illumination and the substrate normal is $\sim 65 - 70^\circ$. The wavelength used here, $\lambda \sim 805\text{nm}$, correspond to the spectral region between the two measured resonance peaks for this particular sample. The measured area is $400 \times 400\text{nm}$

conditions is observed when comparing the ratio between the fields at the top and at the edge of the nanosandwich structure. It is influenced by the size of the fabricated particle and likely also the wavelength, but it can vary considerably even if both of them remains unchanged. This is exemplified in Fig. 7.8 for $d_{\text{spacer}} \sim 20\text{nm}$ and $\mathcal{D} \sim 170\text{nm}$, where the images are all taken with the same tip and ordered according to experimental time. The first image is dominated by the fields at the edge, while in the last the signal at the top of the structure have considerably increased in importance. This progression is not explained by which particular structure is being measured, because the last two images correspond to the same structure and a similar evolution was found for scans of larger areas over many particles.

I propose here a simple interpretation framework to explain the observed behavior as a consequence of tip degradation. The tip is thought of as an sphere, small for sharp tips and large for blunter ones. For a small enough sphere, it can be considered to be immersed in a homogeneous field, even in the near field region, and the strength of the scattered fields will be proportional to the strength of the local fields (the vertical component for aSNOM), i.e., stronger around the edges according to the simulations.

This case would correspond to Fig. 7.8(a). For a larger sphere, the spatial variation of the fields must be considered, as the scattering signal depends on the strength of the fields on its entire volume. Weaker near fields at the top of the structure can result in comparable or larger signal than stronger but more confined fields at the edge, a situation associated with Fig. 7.8(c). Experimentally, it is important to ensure that a difference observed between two images is not due to a change in the apex. For example, different tips should reproduce the change, or the feature under investigation should remain approximately unchanged if the first measurement is repeated after a set of experiments is completed.

More difficult to explain is the influence of the experimental conditions when comparing nanosandwich structures with $d_{\text{spacer}} \sim 20\text{nm}$ and $d_{\text{spacer}} \sim 40\text{nm}$; measurements do not always present the clear differences discussed here. Some of the difficulties can be due to some tips being too broad to resolve the double maxima expected at the edges for $d_{\text{spacer}} \sim 40\text{nm}$, and thus giving results similar to $d_{\text{spacer}} \sim 20\text{nm}$. Small morphological differences between nominally identical particles can also be relevant. A systematic variation of d_{spacer} should help to better understand its influence.

The exact field distribution also vary between particles for the larger single disks considered, where a quadrupole is expected to be excited. The differences may be linked to the phase jump being significantly smaller than the ideal 180 degrees for some of the neighboring regions, an observation still not fully understood but perhaps explained by the quadrupole resonance not being as strongly excited as desired. In some images, the phase jump may be so small as not to be clearly identified as such, with a gradual variation of the phase dominating the results. Additional work has to be done to better understand how the experimental conditions affect the measurements. Again, the shape of the tip apex and irregularities in the structures can be important.

Last, it is interesting to study the dependence of the signal with wavelength. However, In my experiments it is not possible to directly compare the signal strength, as the measurements are very sensitive to the exact experimental conditions¹. It would require

¹Thus, as in general in my thesis, the absolute signal is not compared between experimental images,

a way to normalize the obtained values at different wavelengths, or to use a perfectly achromatic set-up. Instead, I have compared the signal from structures of different sizes present at the same sample. A change of wavelength was expected to influence the optimal size to obtain a stronger near field signature, but such dependence have not been observed neither for the single disks (for $800\text{nm} \lesssim \lambda \lesssim 880\text{nm}$) nor for the nanosandwich structures ($775\text{nm} \lesssim \lambda \lesssim 915\text{nm}$). In the latter case, I do often observe stronger signal from the top of particles with $\mathcal{D} \sim 190\text{nm}$ than with $\mathcal{D} \sim 170\text{nm}$, but such behavior is found for the complete range of wavelengths used and it is not easily related to the measured far field spectra. To better understand the results, it is interesting to measure the resonance of each individual particle at oblique incidence, but notice that the wavelength range used is often significantly larger than the correction on the spectra expected from the new measurements. Considering a larger range of particles sizes and diameters should be helpful to better understand the interplay between size, wavelength and signal strength.

For the future, it is compelling not only to obtain more measurements under different conditions but also to use more refined simulation models, with larger similitude between the simulated and experimental particle morphology, and in particular to include the tip and the used demodulation scheme. The improved calculations can help to understand, for example, the influence of the tip apex shape, of irregularities in the particles shape and of interactions between particles in samples of narrow or broad size distributions.

In this chapter, I have used *aSNOM* to study the behavior of the near fields for several plasmonic structures that can present resonances of different nature: dipoles, quadrupoles and coupled dipoles. It is possible to achieve clear images and a very good lateral resolution, much below the diffraction limit. Simulated results in which only the component of the electric field perpendicular to the substrate is considered agree broadly with the measurements, which support both the nonperturbative nature of our measurements and the bigger sensitivity of *aSNOM* to the mentioned component.

and the color scales are chosen to improve the appearance of each individual image

Chapter 8

Summary and Outlook

This thesis has discussed *aSNOM* simulations and experimental results. Analytical expressions were also derived where possible and useful. The simulations performed represent a significant step towards modeling realistic scenarios. They consider many different geometries for the tip, illumination and substrate characteristics. The absolute power scattered was obtained. The final model in particular (Chs. 4,5) includes long tips, patterned substrates and imaging at higher harmonics, and also model carefully the detector response.

The measurements have two different objectives. The first is to experimentally demonstrate and complement the theoretical discussions to better understand *aSNOM* as a technique. The second is to obtain information about plasmonic structures, making use of a cross-polarization scheme that was studied in Ch. 6. Both sets of measurements are assisted by an alignment procedure developed to gain information about the interference and the focal field distribution of the excitation beam.

I have shown that modeling tips significantly longer than the wavelength and the waist radius is required to closely reproduce typical experimental conditions. As long as no plasmon resonances are present, tips on the order of one to a few wavelengths can be a convenient compromise between precision and numerical requirements. Much shorter tips resulted, however, in significantly diminished strength of the near fields near the tip apex and in scattered fields orders of magnitude weaker. Sufficiently long

tips are thus important to reliably study one of the key objectives of this thesis, how well the contribution from the near fields can be discriminated under different scanning conditions. For the model in Ch. 4, short tips were also found to result in a slightly more spatially confined near field signature.

Modeling long tips, I have obtained a very good discrimination of the near field signal from the tip-substrate interaction for higher harmonic demodulation. Silicon tips were used as a promising alternative for ultimate lateral resolution, and their viability as active *aSNOM* probes was confirmed experimentally. The simulations allow to discuss the influence of substrate and tip oscillation characteristics on the near field discrimination, resolution and demodulated signal strength. Small oscillation amplitude is convenient to improve resolution and near field discrimination, but can ensue in too small signal to noise ratio, and values on the order of the apex radius seem a reasonable compromise. The oscillation of the tip should be kept as sinusoidal as possible, as higher harmonic contributions rapidly increase the level of background. Further, I have shown that the near field signature from small subsurface structures can be discriminated for depths smaller than the tip apex radius, but the resolution slightly worsen and the near field signal rapidly becomes weaker with increasing depths. It illustrates the short range of the near field interaction between tip and substrate, and exemplifies the convenience to keep the distance between the tip and the structure of interest as small as possible, also shown by the behavior of approach curves.

The obtained near field optical signature from the a small structure is more spatially confined than the topography from an AFM image for similar tip apex and structure size. Further, the behavior of the near fields near the the tip apex for isolated tips suggests that the achievable resolution approximately scale with the inverse of the tip apex size. Thus, sub ten-nanometer resolution seems achievable for sufficiently sharp probes.

Interferometric measurements have been used in this thesis, as they allow to obtain stronger signal and are sensitive to the optical phase. I describe more in detail in Ch. 5

the consequences of this choice for the obtained signal. It is first shown that it can be easier to discriminate the near fields for interferometric than for non-interferometric measurements. I then discuss how the phase and amplitude of the signal read at a lock-in are functions of both the optical phase and amplitude. In particular, measurements and simulations serve to illustrate several instances in which the optical phase strongly influences and even changes the nature of images that are obtained using the lock-in amplifier amplitude. The influence of the phase should thus be considered for the correct interpretation of *aSNOM* results.

I also study the influence on *aSNOM* imaging of the spatial inhomogeneity of the scattered fields. The results show that each area element of an extended detector contribute differently to *aSNOM* images, an effect which goes beyond a simple scaling factor. Although the significance of this effect is not large for the experimental measurements and simulation examples discussed in this thesis, it can be more important for particular tip-sample geometries and offer an additional possibility for image optimization.

Last, I have measured the near fields distribution from several plasmonic structures. A cross polarization scheme is first studied and is shown to result in clear images, with low background, and confidence is gained on the passive nature of the AFM tip used as probe. These characteristics can benefit not only the imaging of plasmonic structures, but of many other samples requiring nonperturbative measurements. Single disks and nanosandwich structures are subsequently studied and a good correspondence is obtained between measurements and theoretical expectations. Beyond simple dipolar resonances, images are also obtained of nanosandwich structures which can be defined as strongly interacting dipoles. Measurements of larger disks serve to illustrate the promising capabilities of the used measurement scheme to image high-order resonances on structures of a very general nature.

For the future, it is interesting to extend the simulation work to full 2-dimensional images. Considering other substrates, tips and illuminations can help to better clarify

the ultimate possibilities of *aSNOM* and help in the interpretation of experimental results. Additional work on the near field measurements of the plasmonic structures can give new insights, for example, into the wavelength dependence of the near fields, quadrupole resonances, or the near field interaction between resonating particles. From a practical perspective, near field measurements on these and other plasmonic structures can ultimately help to improve the properties of biosensors and metamaterials.

Bibliography

- [1] M. G. L. Gustafsson, Proc. of the Natl. Acad. of Sciences **102**, 13081 (2005).
- [2] B. Bailey, D. L. Farkas, D. L. Taylor, and F. Lanni, Nature **366**, 44 (1993).
- [3] J. B. Pendry, Physical Review Letters **85**, 3966 (2000).
- [4] I. I. Smolyaninov *et al.*, Phys. Rev. B **72**, 085442 (2005).
- [5] M. J. Rust, M. Bates, and X. Zhuang, Nature Methods **3**, 793 (2006).
- [6] S. W. Hell, S. Lindek, C. Cremer, and E. H. K. Stelzer, App. Phys. Lett. **11**, 1335 (1994).
- [7] K. I. Willig, J. Keller, M. Bossi, and S. W. Hell, New J. of Phys. **8**, 106 (2006).
- [8] E. H. Synge, Philos. Mag. **6**, 356 (1928).
- [9] E. A. Ash and G. Nicholls, Nature **237**, 510 (1972).
- [10] D. W. Pohl, W. Denk, and M. Lanz, Appl. Phys. Lett. **44**, 651 (1984).
- [11] A. Lewis, M. Isaacson, A. Harootunian, and A. Muray, Ultramicroscopy **13**, 227 (1984).
- [12] S. I. Bozhevolnyi *et al.*, Nature **440**, 508 (2006).
- [13] L. Novotny and S. J. Stranick, Annu. Rev. Phys. Chem. **57**, 303 (2006).
- [14] A. Bouhelier, Microscopy research and technique **69**, 563 (2006).

- [15] Y. Inouye and S. Kawata, *Opt. Lett.* **19**, 159 (1994).
- [16] R. Bachelot, P. Gleyzes, and A. C. Boccara, *Microsc. Microanal. Microstruct.* **5**, 389 (1994).
- [17] F. Zenhausern, Y. Martin, and H. K. Wickramasinghe, *Science* **269**, 1083 (1995).
- [18] M. Specht, J. D. Pedarnig, W. M. Heckl, and T. W. Hänsch, *Phys. Rev. Lett.* **68**, 476 (1992).
- [19] B. Knoll and F. Keilmann, *Nature* **399**, 134 (1999).
- [20] R. Bachelot, P. Gleyzes, and A. C. Boccara, *Applied Optics* **36**, 2160 (1997).
- [21] J. Wessel, *J. Opt. Soc. Am. B* **2**, 1538 (1985).
- [22] T. Taubner, R. Hillenbrand, and F. Keilmann, *J. Microscopy* **210**, 311 (2003).
- [23] N. Ocelic and R. Hillenbrand, *Nature Materials* **3**, 606 (2004).
- [24] S. Grésillon *et al.*, *App. Surf. Sci.* **164**, 118 (2000).
- [25] Y. De Wilde, F. Formanek, and L. Aigouy, *Rev. Sci. Instrum.* **74**, 3889 (2003).
- [26] F. Formanek *et al.*, *Superlattices and Microstructures* **35**, 315 (2004).
- [27] J.-S. Samson *et al.*, *Phys. Chem. Chem. Phys.* **8**, 753 (2006).
- [28] B. Knoll, F. Keilmann, A. Kramer, and R. Guckenberger, *Appl. Phys. Lett.* **70**, 2667 (1997).
- [29] M. B. Raschke *et al.*, *ChemPhysChem* **6**, 2197 (2005).
- [30] H.-T. Chen, R. Kersting, and G. C. Cho, *App. Phys. Lett.* **83**, 3009 (2003).
- [31] A. Lahrech, B. Bachelot, P. Gleyzes, and A. C. Boccara, *Opt. Lett.* **21**, 1315 (1996).
- [32] H. F. Hamann *et al.*, *Opt. Commun.* **227**, 1 (2003).

- [33] A. Hartschuh, E. J. Sanchez, X. S. Xie, and L. Novotny, Phys. Rev. Lett. **90**, 095503 (2003).
- [34] T. Ichimura *et al.*, Appl. Phys. Lett. **84**, 1768 (2004).
- [35] A. Bouhelier, M. Beversluis, A. Hartschuh, and L. Novotny, Phys. Rev. Lett. **90**, 013903 (2003).
- [36] C. C. Neacsu, G. A. Reider, and M. B. Raschke, Phys. Rev. B **71**, 201402 (2005).
- [37] J. M. Gerton *et al.*, Phys. Rev. Lett. **93**, 180801 (2004).
- [38] D. Hu *et al.*, Rev. Sci. Instrum. **74**, 3347 (2003).
- [39] A. Bouhelier, M. R. Beversluis, and L. Novotny, Ultramicroscopy **100**, 413 (2004).
- [40] F. M. Huang, F. Festy, and D. Richards, App. Phys. Lett. **87**, 183101 (2005).
- [41] C. Xie, C. Mu, J. R. Cox, and J. M. Gerton, App. Phys. Lett. **89**, 143117 (2006).
- [42] H. Ma and J. Levy, Nano Letters **6**, 341 (2006).
- [43] J. Levy, C. Hubert, and A. Trivelli, J. of Chem. Phys. **112**, 7848 (2000).
- [44] S. C. Schneider, S. Grafström, and L. M. Eng, Phys. Rev. B **71**, 115418 (2005).
- [45] H. Wioland *et al.*, Eur. Phys. J. Appl. Phys. **5**, 289 (1999).
- [46] L. Aigouy *et al.*, J. of microscopy **194**, 295 (1999).
- [47] T. Kalkbrenner *et al.*, Phys. Rev. Lett. **95**, 200801 (2005).
- [48] H. G. Frey, F. Keilmann, A. . Kriele, and R. Guckenberger, App. Phys. Lett. **81**, 5030 (2002).
- [49] R. Eckert *et al.*, Appl. Phys. Lett. **77**, 3695 (2000).
- [50] R. Hillenbrand *et al.*, Appl. Phys. Lett. **83**, 368 (2003).

- [51] R. Bachelot *et al.*, *Microscopy Research and Technique* **64**, 441 (2004).
- [52] L. Stebounova *et al.*, *App. Opt.* **45**, 6192 (2006).
- [53] A. Madrazo, M. Nieto-Vesperinas, and N. García, *Phys. Rev. B* **53**, 3654 (1996).
- [54] A. Madrazo, R. Carminati, M. Nieto-Vesperinas, and J.-J. Greffet, *J. Opt. Soc. Am. A.* **15**, 109 (1998).
- [55] M. Quinten, *App. Phys. B* **70**, 579 (2000).
- [56] B. Hecht *et al.*, *J. Appl. Phys.* **81**, 2492 (1997).
- [57] R. Carminati, A. Madrazo, M. Nieto-Vesperinas, and J.-J. Greffet, *J. Appl. Phys.* **82**, 501 (1997).
- [58] M. Labardi, S. Patane, and M. Allegrini, *Appl. Phys. Lett.* **77**, 621 (2000).
- [59] R. Hillenbrand, B. Knoll, and F. Keilmann, *J. Microscopy* **202**, 77 (2001).
- [60] B. Knoll and F. Keilmann, *Opt. Commun.* **182**, 321 (2000).
- [61] A. Bek, R. Vogelgesang, and K. Kern, *Appl. Phys. Lett.* **87**, 163115 (2005).
- [62] J. L. Bijeon, P. M. Adam, D. Barchiesi, and P. Royer, *Eur. Phys. J. Appl. Phys.* **26**, 45 (2004).
- [63] P. M. Adam, J. L. Bijeon, G. Viardot, and P. Royer, *Opt. Commun.* **174**, 91 (2000).
- [64] J. N. Walford *et al.*, *J. Appl. Phys.* **89**, 5159 (2001).
- [65] D. Mehtani *et al.*, *J. Opt. A* **8**, 183 (2006).
- [66] C. C. Neacsu, G. A. Steudle, and M. B. Raschke, *App. Phys. B* **80**, 295 (2005).
- [67] A. V. Zayats, *Opt. Commun.* **161**, 156 (1999).

- [68] L. Novotny and B. Hecht, *Principles of Nano-Optics* (Cambridge University Press, Cambridge, 2006).
- [69] F. Zenhausern, M. P. Oboyle, and H. K. Wickramasinghe, *Appl. Phys. Lett.* **65**, 1623 (1994).
- [70] J. L. Bohn, D. J. Nesbitt, and A. Gallagher, *J. Opt. Soc. Am. A* **18**, 2998 (2001).
- [71] V. V. Protasenko, A. Gallagher, and D. J. Nesbitt, *Opt. Commun.* **233**, 45 (2004).
- [72] R. Hillenbrand and F. Keilmann, *Appl. Phys. B* **73**, 239 (2001).
- [73] T. J. Yang, G. A. Lessard, and S. R. Quake, *App. Phys. Lett.* **76**, 378 (2000).
- [74] O. J. F. Martin and M. Paulus, *J. of Microscopy* **205**, 147 (2002).
- [75] J. T. Krug II, E. J. Sánchez, and X. S. Xie, *J. Chem. Phys.* **116**, 10895 (2002).
- [76] J. A. Porto, P. Johansson, S. P. Apell, and T. López-Ríos, *Phys. Rev. B* **67**, 085409 (2003).
- [77] S. Renger, J. Grafström, L. Eng, and R. Hillenbrand, *Phys. Rev. B* **71**, 075410 (2005).
- [78] R. Carminati and J.-J. Greffet, *Ultramicroscopy* **61**, 11 (1995).
- [79] O. J. F. Martin, C. Girard, and A. Dereux, *J. Opt. Soc. Am. A* **13**, 1801 (1996).
- [80] D. E. Aspnes and A. A. Studna, *Phys. Rev. B* **27**, 985 (1983).
- [81] P. B. Johnson and R. W. Christy, *Phys. Rev. B* **6**, 4370 (1972).
- [82] L. W. Davis, *Phys. Rev. A* **19**, 1177 (1979).
- [83] J. P. Barton and D. R. Alexander, *J. Appl. Phys.* **66**, 2800 (1989).
- [84] T. Evers, H. Dahl, and T. Wriedt, *Electr. Lett.* **32**, 1356 (1996).
- [85] C. Girard and A. Dereux, *Rep. Prog. Phys.* **59**, 657 (1996).

- [86] J. J. Greffet, A. Sentenac, and R. Carminati, *Opt. Comm.* **16**, 116 (1995).
- [87] D. Barchiesi *et al.*, *Phys. Rev. E* **54**, 4285 (1996).
- [88] M. Xiao and S. Bozhevolnyi, *Opt. Comm.* **130**, 337 (1996).
- [89] R. G. Milner and D. Richards, *J. Microscopy* **202**, 66 (2001).
- [90] H. Furukawa and S. Kawata, *Opt. Comm.* **148**, 221 (1998).
- [91] Y. C. Martin, H. F. Hamann, and H. K. Wickramasinghe, *J. Appl. Phys.* **89**, 5774 (2001).
- [92] R. Fikri *et al.*, *Opt. Commun.* **221**, 13 (2003).
- [93] L. Novotny, R. X. Bian, and X. S. Xie, *Phys. Rev. Lett.* **79**, 645 (1997).
- [94] C. Hafner, *The Generalized Multiple Multipole Technique for Computational Electromagnetics* (Artech, Boston, 1990).
- [95] E. Moreno, D. Erni, C. Hafner, and R. Vahldieck, *J. Opt. Soc. Am. A* **19**, 101 (2002).
- [96] J. P. Kottmann, O. J. F. Martin, D. R. Smith, and S. Schultz, *Phys. Rev. B* **64**, 235402 (2001).
- [97] N. Calander and M. Willander, *J. Appl. Phys.* **92**, 4878 (2002).
- [98] K. L. Wang, A. Barkan, and D. M. Mittleman, *App. Phys. Lett.* **84**, 305 (2004).
- [99] R. E. Collin and F. J. Zucker, *Antenna Theory* (McGraw Hill, New York, 1969).
- [100] K. B. Crozier, A. Sundaramurthy, G. S. Kino, and C. F. Quate, *J. Appl. Phys.* **94**, 4632 (2003).
- [101] Y. C. Martin and H. K. Wickramasinghe, *J. Appl. Phys.* **91**, 3363 (2002).
- [102] O. J. F. Martin and C. Girard, *Appl. Phys. Lett.* **70**, 705 (1997).

- [103] L. Aigouy *et al.*, *Opt. Lett.* **24**, 187 (1999).
- [104] W. X. Sun and Z. X. Shen, *J. Opt. Soc. Am. A* **20**, 2254 (2003).
- [105] A. Bouhelier, M. R. Beversluis, and L. Novotny, *Appl. Phys. Lett.* **82**, 4596 (2003).
- [106] E. Descrovi *et al.*, *App. Phys. Lett.* **85**, 5340 (2004).
- [107] S. K. Rhodes, K. A. Nugent, and A. Roberts, *J. Opt. Soc. Am. A* **19**, 1689 (2002).
- [108] F. H'dhili *et al.*, *Appl. Phys. Lett.* **79**, 4019 (2001).
- [109] Y. Gilbert *et al.*, *Optics express* **13**, 3619 (2005).
- [110] R. E. Larsen and H. Metiu, *J. Chem. Phys.* **114**, 6851 (2001).
- [111] R. Esteban, R. Vogelgesang, and K. Kern, *Nanotechnology* **17**, 475 (2006).
- [112] F. Festy, A. Demming, and D. Richards, *Ultramicroscopy* **100**, 437 (2004).
- [113] A. L. Demming, F. Festy, and D. Richards, *Journal of Chemical Physics* **122**, 184716 (2005).
- [114] C. J. Flaten and E. A. Stern, *Phys. Rev. B* **11**, 638 (1975).
- [115] M. Micic, N. Klymyshyn, Y. D. Suh, and H. P. Lu, *J. Phys. Chem. B* **107**, 1574 (2003).
- [116] J. Van Bladel, *Singular Electromagnetic Fields and Sources* (Oxford University Press, Oxford, 1991).
- [117] R. Ruppin, *Surface Science* **58**, 550 (1976).
- [118] R. Ruppin, *Surface Science* **127**, 108 (1983).
- [119] J. Koglin, U. C. Fischer, and H. Fuchs, *Phys. Rev. B* **55**, 7977 (1997).
- [120] H. Sasaki and Y. Sasaki, *J. Appl. Phys.* **85**, 2026 (1999).

- [121] R. Hillenbrand and F. Keilmann, *Phys. Rev. Lett.* **85**, 3029 (2000).
- [122] M. Moskovits, *Review of Modern Physics* **57**, 783 (1985).
- [123] F. Demming, J. Jersch, K. Dickmann, and P. I. Geshev, *Appl. Phys. B* **66**, 593 (1998).
- [124] L. Aigouy *et al.*, *Appl. Phys. Lett.* **76**, 397 (2000).
- [125] L. Stebounova, B. B. Akhremitchev, and G. C. Walker, *Rev. Sci. Instrum.* **74**, 3670 (2003).
- [126] M. B. Raschke and C. Lienau, *Appl. Phys. Lett.* **83**, 5089 (2003).
- [127] F. Formanek, Y. De Wilde, and L. Aigouy, *Ultramicroscopy* **103**, 133 (2005).
- [128] D. Roy, S. Leong, and M. E. Welland, *Journal of the Korean Physical Society* **47**, 140 (2005).
- [129] T. Taubner, F. Keilmann, and R. Hillenbrand, *Journal of the Korean Physical Society* **47**, S213 (2005).
- [130] R. Hillenbrand, M. Stark, and R. Guckenberger, *App. Phys. Lett.* **76**, 3478 (2000).
- [131] R. W. Stark and W. M. Heckl, *Rev. Sci. Instrum.* **74**, 5111 (2003).
- [132] S. I. Lee, S. W. Howell, A. Raman, and R. Reifenberger, *Phys. Rev. B* **66**, 115409 (2002).
- [133] B. Knoll and F. Keilmann, *Appl. Phys. A* **66**, 477 (1998).
- [134] L. Billot *et al.*, *App. Phys. Lett.* **89**, 023105 (2006).
- [135] C. Girard and A. Dereux, *Phys. Rev. B* **49**, 11344 (1994).
- [136] C. Girard, A. Dereux, O. J. F. Martin, and M. Devel, *Phys. Rev. B.* **50**, 14467 (1994).

- [137] R. A. Frazin, D. G. Fischer, and P. S. Carney, *J. Opt. Soc. Am. A* **21**, 1050 (2004).
- [138] I. S. Averbukh, B. M. Chernobrod, O. A. Sedletsy, and Y. Prior, *Opt. Commun.* **174**, 33 (2000).
- [139] B. B. Akhremitchev, S. Pollack, and G. C. Walker, *Langmuir* **17**, 2774 (2001).
- [140] R. Fikri, T. Grosques, and D. Barchiesi, *Opt. Lett.* **28**, 2147 (2003).
- [141] N. Anderson, P. Anger, A. Hartschuh, and L. Novotny, *Nano Lett.* **6**, 744 (2006).
- [142] G. A. Wurtz, J. Hranisavljevic, and G. P. Wiederrecht, *Nano Lett.* **3**, 1511 (2003).
- [143] Z. Ma, J. M. Gerton, L. A. Wade, and S. R. Quake, *Phys. Rev. Lett.* **97**, 260801 (2006).
- [144] T. Taubner, F. Keilmann, and R. Hillenbrand, *Optics Letters Express* **13**, 8893 (2005).
- [145] Z. H. Kim, B. Liu, and S. R. Leone, *J. Phys. Chem. B* **109**, 8503 (2005).
- [146] N. Ocelic, A. Huber, and R. Hillenbrand, *App. Phys. Lett.* **89**, 101124 (2006).
- [147] L. Gomez *et al.*, *J. Opt. Soc. Am. B* **23**, 823 (2006).
- [148] P. G. Gucciardi, G. Bachelier, and M. Allegrini, *J. App. Phys.* **99**, 124309 (2006).
- [149] P. G. Gucciardi, G. Bachelier, A. Mlayah, and M. Allegrini, *Rev. Sci. Instrum.* **76**, 036105 (2005).
- [150] J. Renger, S. Grafström, L. M. Eng, and V. Deckert, *J. Opt. Soc. Am. A* **21**, 1362 (2004).
- [151] D. Ganic, X. Gan, and M. Gu, *Opt. Express* **12**, 5325 (2004).
- [152] M. Brehm, T. Taubner, R. Hillenbrand, and F. Keilmann, *Nano Lett.* **6**, 1307 (2006).

- [153] A. Bek, Ph.D. thesis, EPFL, 2004.
- [154] A. Bek, R. Vogelgesang, and K. Kern, *Rev. Sci. Instrum.* **77**, 043703 (2006).
- [155] S. Grésillon, R. Lecaque, L. Willame, and J. Rivoal, *App. Phys. B* **84**, 167 (2006).
- [156] G. Wurtz, R. Bachelot, and P. Royer, *Rev. Sci. Instrum.* **69**, 1735 (1998).
- [157] N. Anderson, A. Bouhelier, and L. Novotny, *J. Opt. A: Pure. Appl. Opt.* **8**, 227 (2006).
- [158] G. Zorinians, O. Kurnosikov, W. J. M. de Jonge, and B. Koopmans, *Jap. J. of App. Phys.* **45**, 2111 (2006).
- [159] K. Kreibig and M. Vollmer, *Optical Properties of Metal Clusters* (Springer, Berlin Heidelberg, 1995).
- [160] V. M. Shalaev, *Nature photonics* **1**, 41 (2007).
- [161] Y. Lu *et al.*, *Nano Lett.* **5**, 119 (2005).
- [162] T. Rindzevicius *et al.*, *Nano Lett.* **5**, 2335 (2005).
- [163] A. N. Grigorenko *et al.*, *App. Phys. Lett.* **88**, 124103 (2006).
- [164] A. Dahlin *et al.*, *J. Am. Chem. Soc.* **127**, 5043 (2005).
- [165] H. Wang *et al.*, *Nano Lett.* **6**, 827 (2006).
- [166] A. D. McFarland and R. P. Van Duyne, *Nano Lett.* **3**, 1057 (2003).
- [167] A. J. Haes *et al.*, *Nano Lett.* **4**, 1029 (2004).
- [168] A. Dmitriev, T. Pakizeh, M. Käll, and D. S. Sutherland, *Small* **3**, 294 (2007).
- [169] T. Pakizeh *et al.*, *Opt. Express* **14**, 8240 (2006).
- [170] T. Pakizeh *et al.*, *Phys. Rev. B* (Submitted) .

[171] S. Gresillon *et al.*, Phys. Rev. Lett. **82**, 4520 (1999).

[172] A. N. Grigorenko *et al.*, Nature **438**, 335 (2005).

Curriculum vitae

Name: Rubén Esteban Llorente

Date of Birth: May 5, 1978

Nationality: Spanish

1996–1997 Engineering, Université Libre de Bruxelles, Belgium

1997–2001 Telecommunications Engineering School, Polytechnical University of Madrid, Spain

2001–2002 Engineering at the Royal Institute of Technology, Degree Programme in Electrical Engineering, Stockholm, Sweden. Thesis title: “Quantum Effects in DG-MOSFETs with a sub-5 nm Thick Si Body”

Received M. Sc. from Royal Institute of Technology, Stockholm (Sweden) and Título de Ingeniería from the Polytechnical Univ. of Madrid (Spain)

2003–2007 PhD student in the group of Prof. K. Kern at the Max Planck Institute for Solid State Research, Stuttgart, Germany, PhD thesis: “Apertureless SNOM: realistic modeling of the imaging process and measurements of resonant plasmonic nanostructures.”

List of publications

Tip-substrate interaction in optical near field microscopy. R. Esteban, R. Vogelgesang and K. Kern. Phys. Rev. B 75, 195410, (2007)

Simulation of optical near and far fields of dielectric apertureless scanning probes. R. Esteban, R. Vogelgesang and K. Kern. Nanotechnology 17, 475 (2006).

Beyond lock-in analysis for volumetric imaging in apertureless scanning nearfield optical microscopy. R. Vogelgesang, R. Esteban and K. Kern. Accepted in Journal of Microscopy.

Kinetic origin of island intermixing during the growth of Ge on Si(001) G. Katsaros, G. Costantini, M. Stoffel, R. Esteban, A.M. Bittner, A. Rastelli, U. Denker, O.G. Schmidt and K. Kern Phys. Rev. B 72, 195320 (2005).

A gettering simulator: evaluating contamination and gettering processes, C. del Cañizo, L.J. Caballero, R. Esteban and A. Luque. Proceedings 3rd World Conference and Exhibition on Photovoltaic Solar Energy Conversion (Osaka, Japan), pp. 993-996 (2003).

Impurity segregation to sink layer during phosphorus gettering. L.J. Caballero, C. del Cañizo, R. Esteban, A. E. Moussaoui and A. Luque. Proceedings 3rd World Conference and Exhibition on Photovoltaic Solar Energy Conversion (Osaka, Japan), pp. 1013-1016 (2003) .

Acknowledgements

A thesis lasts a long time and it can be frustrating when things do not work out. Always, but specially at those times, it is important to have someone that helps you at work, and absolutely necessary to have fun with friends outside and inside the work place. I would like to thank, without any particular order.

To **Ralf Vogelgesang**, for so many things that I am sure I will forget some here. You have been a friend, have taught me physics, were encouraging and had patience with my errors and my pseudo-philosophical questions on when sure is really sure. In particular, it is thanks to you that I have been able to shift towards theory and to learn some quantum mechanics, of such interest to me. I am sure your continued guidance have been fundamental in my development as a physicist, and I hope also as a person. If the opportunity ever comes, I just want to be as good a supervisor as you have been. A difficult task this will be.

To **Prof. Klaus Kern**, which had confidence in me and gave me the opportunity to make the thesis in his group, even if my engineer education was far from the topics of the department.

To the people from the department with whom I directly worked. **Alpan Bek**, who built the instrument I have used and taught me how to use it. Each problem you discovered has shorten my thesis in months. To **Jens Dorfmueller**, with whom I spend many months in the lab. My conversations with you served to better understand many things, and your patience building pieces for me was really useful. Sorry for the times

I altered your carefully aligned setup. To **Sinan Balci**, with whom I spend some time fighting against virus. To **Eduardo Lee**, I would remember our re-discovery of the confocal microscope. I hope you will be successful with your PETI. And to my private Chauffeur, **Georgios Katsaros** who risked his life for my benefit. I enjoyed greatly my time with you, and I will have to visit Grenoble to taste greek sweets.

To my collaborators in Chalmers, **Alexandre Dmitriev, Prof. Duncan Sutherland, and Tavakol Pakizeh**. It was a pleasure to work with you, let's go now for those papers.

To **Prof. Christian Hafner** for the help with the simulation program.

To the thesis tribunal, **Prof. Giovanni Dietler, Prof. Christian Hafner and Dr. Javier Aizpurua**, for the time taken to evaluate my work.

To **Prof. Vitali V. Metlushko and Dr. Marcos Grimsditch**, for fabricating several of the samples I used during my PhD.

To my office colleges, **Sasha and Tilman**, who have had patience with my sub-optimal order and my large tolerance to warm weather. More than one work hour was spent talking with you.

A la comunidad española e hispano hablante, que no ha permitido que olvidara mi idioma ni mi origen, al menos no completamente. **All the Alicias, Esther, Paola, Ajo, Cristina, Maggie, Carlos, Dimas, Pepe, Ivan, Omar, Nacho, ..**

To our "eating group", either in the Cantine or in our private corner tasting international specialities. **Alicia, Violetta, Cristina, Tilman, both Jens, Georgios, Eduardo, Carlos, Thomas, Kannan, and others**, you were often the first to know if I wanted to break the computer or the microscope, and my visits to the 5C11 lab made me a regular.

To my climbing-snow-trekking-biking, and also generally having fun, friends, with whom I spent many fun hours in the open, or in warm closed places. I already have mentioned many of you, I must refer here to **Marina, Eleonora, Lucia, Rudeesun, Eva, Franck, Ioannis, Jean Rene, Erik, Thomas, Milan, David, Julius, Olivier, Mael, Mark, Martin, Rodney, Armando, Diego, Vladimir ...** You did not manage to kill me, either by fall, or by exhaustion after biking.

In general to all the people in the department and to so many other people in the institute or outside.

Y muy especialmente, a mi familia, y en particular a mis padres y a mi hermana. Mis viajes por el extranjero nos han hecho estar más separados de lo que hubiéramos querido, pero saber que siempre apoyais mis decisiones, y que siempre estáis cuando necesito ayuda, ha sido y será muy importante para mi. Os echo de menos.